Nonlinear Optical Control of Josephson Coupling in Cuprates

Dissertation

zur Erlangung des Doktorgrades an der Fakultät für
Mathematik, Informatik und Naturwissenschaften

Fachbereich Physik
der Universität Hamburg

vorgelegt von

ELIZA CASANDRUC

aus Galați, Romania

Hamburg

2016

Gutachter der Dissertation: Prof. Dr. Andrea Cavalleri

                 Prof. Dr. Martin Eckstein

Zusammensetzung der Prüfungskommission: Prof. Dr. Andrea Cavalleri

                 Prof. Dr. Martin Eckstein

                 Prof. Dr. Ludwig Mathey

                 Prof. Dr. Franz Kärtner

                 Prof. Dr. Michael Rübhausen

Vorsitzender der Prüfungskommission: Prof. Dr. Michael Rübhausen

Datum der Disputation: 15.03.2017

Vorsitzender des Promotionsausschusses: Prof. Dr. Wolfgang Hansen

Dekan der Fakultät MIN: Prof. Dr. Heinrich Graener

Leiter des Fachbereich Physik: Prof. Dr. Michael Potthoff

Hiermit erkläre ich an Eides statt, dass ich die vorliegende Dissertationsschrift selbst verfasst und keine anderen als die angegebenen Quellen und Hilfsmittel benutzt habe. Diese Arbeit lag noch keiner anderen Person oder Prüfungsbehörde im Rahmen einer Prüfung vor.

I hereby declare, on oath, that I have written the present dissertation on my own and have not used other than the mentioned resources and aids. This work has never been presented to other persons or evaluation panels in the context of an examination.

                  Eliza Casandruc

                  Hamburg, 2016

Unterschrift / Signature:

Datum / Date:

Cu mult drag, familiei mele

Abstract

In High-T_C cuprates superconducting Cu-O planes alternate with insulating layers along the crystallographic c-axis, making the materials equivalent to Josephson junctions connected in series. The most intriguing consequence is that the out-of-plane superconducting transport occurs via Cooper pairs tunneling across the insulating layers and can be predicted by the Josephson tunneling equations.

Nonlinear interaction between light fields and the superconducting carriers serves as a powerful dynamical probe of cuprates, while offering opportunities for controlling them in an analogous fashion to other stimuli such as pressure and magnetic fields. *The main goal of this thesis work is to use intense transient light fields to control the interlayer superconducting transport on ultrafast time scales*. This was achieved by tuning the wavelength of such light pulses to completely different ranges, in order to either directly excite Josephson Plasma Waves in the nonlinear regime, or efficiently melt the competing charge and spin order phase, which in certain cuprates quenches the Josephson tunneling at equilibrium.

In a first study, I have utilized strong field terahertz transients with frequencies tuned to the Josephson plasma resonance (JPR) to coherently control the c-axis superconducting transport. The Josephson relations have a cubic nonlinearity which is exploited to achieve two related, albeit slightly different, phenomena. Depending on the driving pulse, solitonic breathers were excited with narrow-band multi-cycle pulses in $La_{1.84}Sr_{0.16}CuO_4$ while broad-band half-cycle pulses were employed to achieve a parametric amplification of Josephson Plasma Waves in $La_{1.905}Ba_{0.095}CuO_4$. These experiments are supported by extensive modeling, showing exceptional agreement. A comprehensive study illustrates the strong enhancement of the nonlinear effects near the JPR frequency.

Then, I turned to investigate the competition between superconductivity and charge- and spin-order (the so called stripe phase) in $La_{1.885}Ba_{0.115}CuO_4$. I have demonstrated selective melting of the stripe phase through the irradiation with high photon energy pulses, which results in a transient enhancement of the c-axis superfluid density. The dependence of the effect on the wavelength of the pump pulse suggests a dominant energy scale which is at play with superconductivity, supporting the competing nature between the stripe and the superconducting order.

Zusamenfassung

Im Aufbau von Hochtemperatur-Kuprat-Supraleitern wechseln sich entlang der kristallographischen c-Achse Cu-O Ebenen und isolierende Schichten ab, was diese Materialklasse zu in Serie geschalteten Josephson-Kontakten gleichsetzt. Die faszinierendste Konsequenz dieser Anordnung ist, dass der supraleitende Transport senkrecht zu den Materialebenen über das Tunneln von Cooper-Paaren durch die isolierenden Schichten geschieht und durch die Josephson-Gleichungen vorhergesagt werden kann.

Nichtlineare Wechselwirkungen zwischen Lichtfeldern und dem supraleitenden Zustand dienen als hilfreiche dynamische Sonden zur Untersuchung solcher Materialien. Gleichzeitig eröffnen sie Kontrollmöglichkeiten analog zu denen anderer Stimuli wie Druck und Magnetfeldstärke, allerdings für ultraschnelle Zeitskalen. *In dieser Arbeit nutze ich ultraschnelle Terahertzspektroskopie zur Untersuchung der supraleitenden Eigenschaften zweier Klassen einlagiger La-214 Kupratproben mit und ohne Ausbildung konkurrierender Ladungsstreifen-Ordnung. Die nichtlineare Wechselwirkung der Proben mit Lichtfeldern wird zudem zur gezielten Steuerung der Materialeigenschaften eingesetzt.*

Zur kohärenten Kontrolle der c-Achsen-Supraleitung habe ich starke Terahertztransienten eingesetzt, deren Frequenzen an die Josephson-Plamsaresonanz des jeweiligen Materials angepasst wurde. Die supraleitenden Eigenschaften der Kuprate entlang ihrer c-Achse werden maßgeblich duch die Josephson-Beziehungen bestimmt. Ihre kubisch-nichtlineare Natur wird dazu genutzt in Abhängikeit vom anregenden Lichtpuls die folgenden zwei zwar in Beziehung stehenden aber dennoch unterschiedlichen Phänomene zu erzeugen: Durch schmalbandige mehrzyklische Pulse werden in $La_{1.84}Sr_{0.16}CuO_4$ "solitonische Atmer" (engl.: solitonic breathers) angeregt, wohingegen breitbandige halbzyklische Pulse eine parametrische Verstärkung der supraleitenden Phasenfluktuationen in $La_{1.905}Ba_{0.095}CuO_4$ bewirken. Die eingehende Untersuchung zeigt eine deutliche Verstärkung der nichtlinearen Effekte in der Nähe der Resonanzfrequenz auf.

Außerdem stelle ich in dieser Arbeit die optische Verstärkung der c-Achsen Superfluiddichte in Kupraten mit konkurrierender Ladungsstreifen-Ordnung dar. In $La_{1.885}Ba_{0.115}CuO_4$ konnte ich das selektive Schmelzen der sich ausbildenden streifenförmigen Phasen mittels Lichtpulsen hoher Photonenenergie zeigen. Dies resultiert in einem stetigen

Anstieg der c-Achsen Superfluid-Dichte. Die Abhängigkeit des Effekts von der Wellenlänge des Pumppulses spricht für eine dominante Energieskala, die in einer Beziehung zur der Supraleitung steht. Dies unterstützt die Konkurrenz zwischen der streifenförmigen Ladungsträgerdichtewellen-Phase und der supraleitenden Phase.

Contents

1

Introduction

1.1. Strongly correlated materials

Conventional band theory successfully describes the electronic properties of many solids. Within this framework, the concept of quasiparticles is invoked to describe electronic excitations. Quasiparticles are free-electron like particles with a renormalized mass that is attributed to the complex many body interactions. However, in materials where Coulomb interactions are important, the quasiparticle picture and the predictions of band theory fail to reproduce their properties. Indeed, in such systems, electron correlations lead to a variety of exotic ground states and complex phase diagrams [1]. Among these states, one of the most exciting state and thus the most studied, is unconventional superconductivity.

The macroscopic behavior of the superconducting condensate can be successfully described by a single wave function which maintains phase-coherence over long distances. One of the most intriguing manifestations of the macroscopic phase coherence is observed when two superconductors are separated by a thin insulating barrier; this configuration forms the so-called Josephson junction. In this case, a zero voltage

supercurrent flows across the barrier, with an amplitude determined by the superconducting order parameter phase difference across the link. These junctions can be fabricated based on niobium technology [3]; however they turned out to naturally occur in several classes of anisotropic superconductors, such as cuprates.

Cuprates are high-temperature superconductors with a layered crystal structure, comprising of superconducting Cu-O planes separated by insulating layers. Adjacent layers are coupled by the Josephson effect which mediates the superconductivity across the planes, making superconductivity three-dimensional. The inductive coupling, together with the capacitive behavior, gives rise to a collective plasma oscillation of Cooper-paired electrons, resulting in a plasma resonance (the so-called Josephson resonance) at terahertz frequencies.

1.2. Photo-induced phenomena

Understanding microscopic interactions and engineering collective responses to tailor material functionalities has been of central importance in the fields of condensed matter physics and material science, both from a fundamental and technological point of view. In particular, much effort has been made to increase the transition temperature of high-Tc superconductors to realize practical applications of superconducting materials beyond the cryogenic confines of a laboratory.

Conventional methods to modify and control the properties of superconductors include chemical doping, application of pressure and magnetic or electric fields and varying the temperature. These stimuli can modify the thermodynamic landscape, thereby rendering control over such systems.

In addition to the methods mentioned above, a conceptually different path consists in perturbing the properties of a material using light. Depending on the energy of the photons, the effects of photoexcitation vary from carrier excitation to photo-induced structural and electronic phase transitions.

In particular, terahertz science is of critical importance in the field of condensed matter physics, as many fundamental excitations in metals and semiconductors (e.g. phonon modes, intraband transitions), as well as superconductors (e.g. superconducting gap, Josephson plasma resonance) are observed at THz frequencies. *It is the aim of this*

thesis to investigate, through ultrafast spectroscopy, the nonlinear physics of Josephson tunneling in cuprates.

In particular, the direct excitation of the Josephson plasma resonance by ultra-short intense terahertz light has proven to be an extremely efficient route towards driving the system into the nonlinear regime. Indeed, the studies presented in the first part of this thesis report on two distinct phenomena: optical excitation and detection of solitonic breathers in cuprates and parametric amplification of Josephson plasma waves.

The second part of the thesis focuses on cuprates for which the Josephson tunneling is suppressed at equilibrium by the existence of charge and spin density waves. In this particular case, high energy photons were used to directly melt the competing orders, thus restoring the interlayer Josephson coupling.

1.3.   Structure of the thesis

Chapter 2 introduces the physics of Josephson junctions, in close connection to the c-axis optical response of high-T_C cuprates. *Chapter 3* presents a theoretical study based on numerically solving the sine-Gordon equation which describes the nonlinear behavior of terahertz driven high-T_C cuprates along the c-axis. The simulations are successfully compared to corresponding experimental data. *Chapter 4* introduces the concepts of charge (and spin) order, with emphasis on the interplay (and competition) that this phase has with superconductivity in cuprates. *Chapter 5* presents an experimental study on the enhancement of c-axis superconducting transport by direct melting of charge and spin order, upon photo-excitation. *Chapters 3 and 5 present the main results of this work*. All chapters can be read independently.

Details of the experimental methods and the Matlab code used for simulations are reported in the appendices.

2

C-axis properties of
High-T$_C$ Cuprates

High-T$_C$ cuprates were discovered in 1986 in a mixed metal copper oxide, La$_{2-x}$Ba$_x$CuO$_4$ (LBCO) at T$_C$ = 30 K [5]. The crystal structure of La$_2$CuO$_4$ is layered, with alternating Cu-O and La-O planes, with the heavy La ions acting as charge reservoirs for the planes. The layered crystal structure also accounts for a strong anisotropy of their physical properties. A partial substitution of La^{3+} by Ba^{2+} in the parent compound introduces holes into the copper-oxygen layers and causes the newly-substituted compound to become metallic, and exhibit superconductivity with a maximum of T$_C$ = 35 K. In the similar manner, substitution of divalent Sr^{2+} for trivalent La^{3+} in the parent compound results in the similar superconducting compound La$_{2-x}$Sr$_x$CuO$_4$ (LSCO) [6]. LSCO has a maximum T$_C$ of ≈ 38 K for a doping level of x = 0.16. Both LBCO and LSCO are part of the same HTS cuprate family, La-214, which has a rather simple crystal structure (*i.e.* high-quality crystals free from twinning are relatively simple to grow), making them appealing for experimental studies [7]. After their initial discovery, the

transition temperature in cuprates raised rapidly above the melting point of nitrogen, T = 77 K. This was achieved in cuprate families such as $YBa_2Cu_3O_{6+y}$ (YBCO) [8] with T_C = 93 K and higher or $Ba_2Sr_2CaCu_2O_{8+y}$ [9]. In the latter, bismuth can also be replaced with thallium or mercury, which results in the highest critical temperature material known to date (T_C = 138 K), at ambient pressure [10], [11].

The central theme of this thesis involves investigation and control of the superconducting coupling along the direction perpendicular to the CuO_2 planes (or Josephson coupling) through nonlinear light-matter interaction on LBCO and LSCO samples. In this chapter I will present some of the most intriguing characteristics of cuprates, with emphasis on out-of-plane properties of the La-214 family and Josephson physics.

2.1. Crystal structure of the La-214 cuprate family

With the mechanism of HTS yet to be understood, there are nonetheless a number of points that are certain. In the case of cuprates, the Cooper pairs responsible for superconductivity are mainly localized in the CuO_2 planes of the perovskite structure, imprinting highly anisotropic properties on the material.

From the microscopic point of view, cuprates can be considered as a stack of quasi-two-dimensional superconducting CuO_2 planes (ab-planes), separated by an insulating layers (built of ions such as Lanthanum, Strontium, Barium) with a thickness comparable to (or, to some extent, greater than) the c-axis coherence length. The anisotropy of the system is determined by the thickness of the insulating layers and this translates in a confined 2D electronic motion, despite Coulomb interactions between carriers being three-dimensional. The ratio of the normal-state resistivities along and perpendicular to the c-direction , ρ_c/ρ_{ab}, is of the order of 10^2 to 10^5, while in the superconducting state the critical current across the layers can be orders of magnitude lower than in the ab-plane.

In Figure 2.1 the crystal structure of LBCO / LSCO is shown. The CO_2 planes form a checkboard pattern, with the Cu^{2+} ions positioned at the centers of squares, while the O^{2-} ions lay in the corners. Oxygen ions surround the copper ions to form octahedral cages, separated from each other by sheets containing lanthanum and strontium ions. The

unit cell is rotated by 45° from the checkerboard pattern, where the center and corners are occupied by the copper ions [12], [13]. In panel b the two-dimensional CuO_2 layers are shown. As 'x' holes per Cu ion are introduced into the layer by doping, the charge carriers become mobile and metallic conductivity develops. For a critical level of doping the material becomes superconductor, with this property becoming three dimensional, due to tunneling of Cooper pairs from one superconducting layer to another.
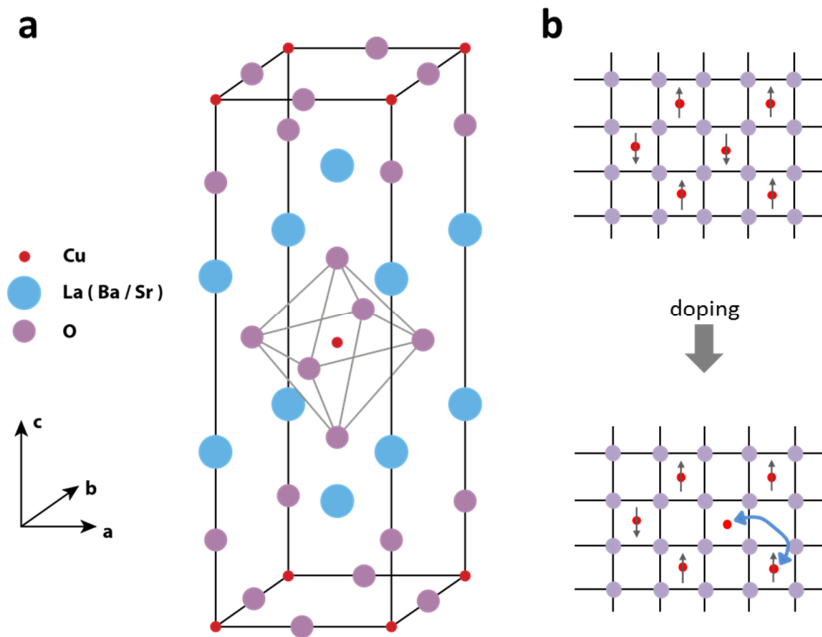

Figure 2.1: Crystal structure of LBCO/LSCO a. The unit cell of LBCO/LSCO, highlighting the perovskite crystal structure. **b**. Two dimensional CuO_2 layer. As holes are introduced in the Cu sites, the charge carriers can hop from one site to another, thus becoming mobile.

2.2.   The cuprates as stacks of Josephson junctions

As a consequence of structural anisotropy, cuprates turn out to act as stacks of Josephson junctions. In these materials, in the superconducting phase, superconducting carriers move without resistance within the copper-oxygen planes, while the out-of-plane (c-axis) electrodynamics are dominated by tunneling between the CuO_2 layers [14]. Thus, tunneling between planes makes possible three-dimensional coherent transport in cuprates, and the c-axis electrodynamics can be understood by considering a Josephson junction array configuration. The validity of this analogy was demonstrated by Kleiner et

al. after they directly measured the d.c. and a.c. Josephson effects in a Bi$_2$Sr$_2$CaCu$_2$O$_8$ single crystal [15]–[17]. Thus, in order to explain the c-axis transport in cuprates, we need to first illustrate the basics of a Josephson junction, which is based on the assertion that electrons can tunnel between two superconductors separated by a thin insulating layer. This effect was predicted by B. D. Josephson in 1962 [18].

In his analysis, Josephson considered two superconductors connected by a thin insulating layer (Figure 2.2a). The insulating barrier has to be thin enough to allow the tunneling of the Cooper pairs. As mentioned before, one essential characteristic of the superconducting state is the existence of a many-particle condensate wave function maintaining phase coherence over a macroscopic distance. For a single junction, one can write the following equations for the wave functions:

$$\psi_1 = \sqrt{\rho_1} e^{i\phi_1}$$
$$\psi_2 = \sqrt{\rho_2} e^{i\phi_2},$$

where ϕ_1 and ϕ_2 are the phases of the condensate wave functions on both sides of the junction respectively, and ρ_2 and ρ_2 are the corresponding Cooper-pair densities.

The two Josephson equations are:

$$I_S = I_C \sin\phi$$
$$\frac{d}{dt}\phi = \frac{2eV}{\hbar}$$

and describe the dynamics of the difference in the phase of the superconducting order parameter between the two superconducting layers ($\phi = \phi_1 - \phi_2$). The first equation states that, between two superconducting electrodes separated by a thin insulating layer there exists a supercurrent, I$_S$, determined by the phase difference ϕ. In the ideal case in which there is no voltage drop across the junction, the supercurrent can take any value between –I$_C$ and I$_C$; therefore I$_C$ denotes the maximum supercurrent that the junction can support. The second equation describes the temporal evolution of the relative phase, ϕ, in case a voltage difference were established and maintained across the link. From here, it follows that the supercurrent will oscillate sinusoidally for a constant voltage drop, with amplitude I$_C$ and frequency *2eV/ℏ*. These predictions are known as the d.c. and a.c. Josephson effects and stay at the core of Josephson physics.

The Josephson junction is equivalent to an LC circuit (Figure 2.2 b): a real junction is modelled by an ideal weak link J (which gives the inductive response, L = J) shunted in parallel by a voltage independent resistance R (corresponding to dissipation via tunneling of non-superconducting quasiparticles) and a capacitance C (which accounts for charging effects, due to the junction geometry). This is the so-called *RCSJ* circuit model of the Josephson junction, with the resonance frequency ω_p corresponding to $1/\sqrt{LC}$ in the case of the undamped oscillator circuit.
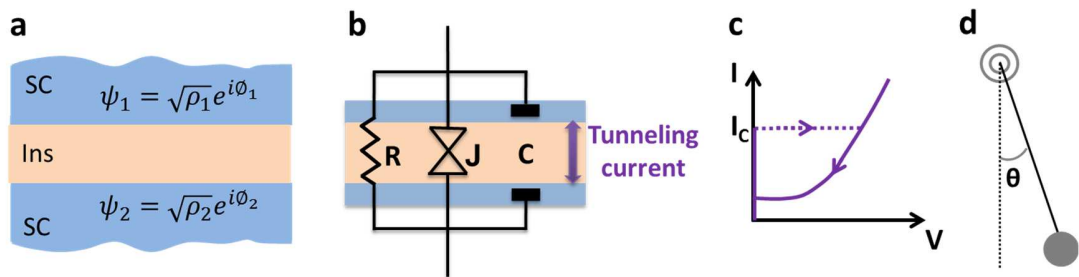

Figure 2.2: Josephson junction and equivalents a. Conventional Josephson junction, with $\boldsymbol{\psi_{1,2}}$ being the microscopic wave functions describing the superconducting electrons on each side of the barrier **b**. Equivalent RCSJ circuit model of a Josephson junction **c**. I-V characteristic of a Josephson junction **d**. Mechanical analogue of the Josephson effect: the angle of deviation corresponds to the phase difference, the angular velocity to the voltage, and the torque to the current.

2.3. Sine–Gordon equation

In long Josephson junctions, where the spatial dependence of the phase in the direction perpendicular to the junction has to be taken into account, the two Josephson relations are supplemented with Maxwell's equations. The phase evolution, $\emptyset(x,t)$, in one dimension, follows the sine-Gordon equation:

$$\frac{1}{\omega_p^2}\frac{\partial^2\emptyset}{\partial t^2} - \lambda_J^2\frac{\partial^2\emptyset}{\partial x^2} + \sin(\emptyset) = 0$$

The time modulation of $\emptyset$ scales with $1/\omega_p$, while the spatial variation scales with the Josephson penetration depth λ_J. The sine-Gordon equation is a nonlinear partial di☐erential equation which describes the electrodynamics of the long Josephson junction.

A general solution for the sine-Gordon equation has not yet been found, but some special cases can be treated analytically and will be presented throughout this chapter (for a more general overview, also consult Table 2.1). In complex physical systems, some of the solutions of sine-Gordon equation (*i.e* solitons, kinks and breathers) appear in various situations, including dislocations in crystals [19], nonlinear spin waves in superfluids [20], waves in ferromagnetic and anti-ferromagnetic materials [21], [22], and nonlinear excitations in living cellular structures [23]. Moreover, this equation also exactly describes a bunch of simple, plane pendula coupled together by the spatial derivative term.

In particular, in the case of Josephson physics, the sine-Gordon equation encapsulates all the well-known phenomena of the Josephson junctions in different limits, as described below. First, if both temporal and spatial variation are considered in the limit of small phase amplitudes, $\sin(\emptyset) = \emptyset$, the sine-Gordon equation describes the linear wave equation, leading to Josephson plasma waves (JPWs), with the phase taking the form $\emptyset \sim e^{i(k_x x - \omega t)}$. For plane waves of this type, the dispersion relation takes the form: $k_x{}^2 = \frac{\varepsilon_\infty}{c^2}\left(\omega^2 - \omega_p^2\right)$. Thus, for $\omega < \omega_p$, the wave vector k_x becomes imaginary and wave propagation inside the material is forbidden, due to screening, while for $\omega > \omega_p$, JPWs can propagate inside the material. As mentioned above, in cuprates the JPWs consist of collective oscillations of Cooper-paired electrons and lead to a Josephson plasma resonance in the superconducting state. This is presented in detail in the next section of this chapter.

It is worth mentioning that there is a mechanical analogue to the Josephson junction, that can aid us in assimilating the physics behind: the dynamics of the relative phase, $\emptyset$, obeys the equations of motions as the angular displacement of the simple pendulum, θ. Thus, in the case of the physical pendulum attached to a pulley (Figure 2.2d), the angle of deviation corresponds to the phase difference, the torque is the analogue of the superconducting current, while the average angular velocity of the mechanical pendulum corresponds to the voltage across a weak link. In the limit of small angles, $sin\theta \approx \theta$, the resonance frequency of the pendulum corresponds to small amplitude oscillations around the equilibrium position, $\theta = 0$. This mechanical resonance is the analogue of Josephson plasma waves.

2.3.1. The Josephson plasma resonance (JPR); c-axis optical properties of cuprate superconductors

The interplay between the capacitive coupling and the tunneling between the CuO_2 planes gives rise to a collective oscillation of Cooper-paired electrons, or Josephson plasma waves [24]. The insulating planes in layered cuprates have thicknesses of the order of interatomic distances (*i.e.* the lattice parameters of LSCO are a = 0.3773 nm and c = 1.3166 nm), resulting in plasma frequencies in the terahertz regime, as opposed to the resonances that are found in macroscopic Josephson junctions, which fall in the megahertz to gigahertz range. The Josephson plasma resonance (JPR) in cuprates, typically investigated using frequency domain techniques, can be observed directly by time-domain terahertz spectroscopy [25] and modelled by the sine-Gordon equation.

In the following I will introduce the equilibrium optical response of LSCO along the c direction, as obtained from terahertz spectroscopy measurements and from simulations of the sine-Gordon equation. A full description of the numerical model will be made in Chapter 3.

Figure 2.3 shows steady-state terahertz time-domain spectroscopy measurements probing the out-of-plane response of $La_{1.84}Sr_{0.16}CuO_4$. Panel a depicts typical traces of the single cycle THz electric field pulse reflected from the sample both below (T = 5K) and above (T = 40K) the superconducting transition temperature of the material. The electric field is polarized along c-axis and sent on the LSCO sample. At low temperatures, clear long-lived oscillations are observed on the trailing edge of the reflected pulse (red), which are not there for temperatures above T_C (black). These oscillations stand as evidence for the Josephson plasma resonance, which, in this material is at $\omega_p = 2\,THz$. The plasma resonance is also clearly visible in the simulations (panel b), where the reflected field also shows clear oscillations with a half a picosecond period.
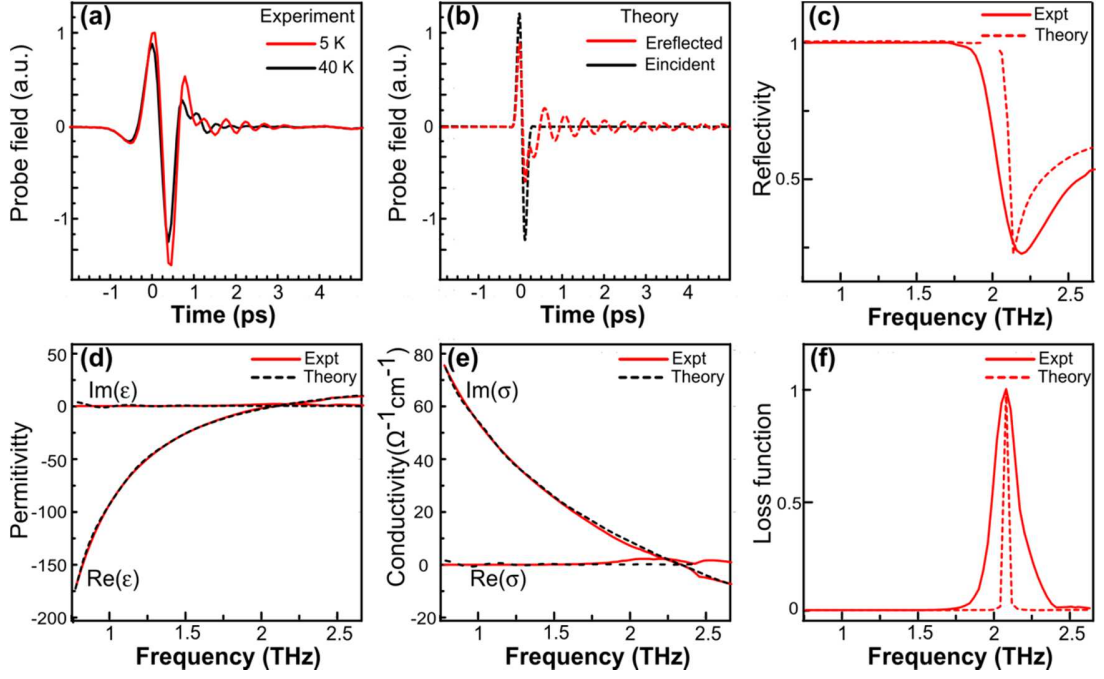
Figure 2.3: Measured (continuous lines) and simulated (dotted lines) c-axis optical properties of LSCO x = 0.16 associated with the JPR phenomenon. a. Time-dependent terahertz transient field detected after reflection from the sample, above (black lines) and below (red) T$_C$. For T < Tc, long lived oscillations on the trailing edge of the pulse signal the onset of interlayer Josephson coupling. **b**. Incident electric field used for the simulation (black) together with the field reflected from the sample surface (red), which shows clear oscillations with 0.5 ps period. In panels **c**, **d**, **e** and **f** the reflectivity $r(\omega)$, complex dielectric function $\varepsilon(\omega)$, complex conductivity $\sigma(\omega)$, and the energy loss function $-\mathrm{Im}(1/\tilde{\varepsilon}(\omega))$ are shown respectively.

In order to deduce the absolute sample reflectivity, the incident pulse is also recorded for comparison. The frequency-dependent complex reflection coefficient is then derived as the ratio of the Fourier transforms of the reflected and incident fields:

$$r(\omega) = \frac{E_{refl}(\omega)}{E_{inc}(\omega)}.$$

The reflectivity calculated as $R = |r(\omega)|^2$ is displayed in Figure 2.3 c. Above the superconducting transition temperature (T > T_C), the c-axis response is insulator-like and the reflectivity essentially featureless. As the sample undergoes the superconducting transition (T < T_C), the reflectivity characteristics change dramatically (red line). The reflectivity approaches unity at low frequency, drops sharply at $\omega = \omega_p$, and then recovers to the value of the normal state for higher frequencies. These measurements, which are reminiscent of the plasma edge observed in conventional metals [2], reproduce the well-characterized Josephson plasma resonance in this compound [4], [26], [27]. Simulations (red dotted line) show a good agreement with experimental data, reproducing the edge in reflectivity at around 2 THz.

From the complex reflection coefficient, all other optical properties can be deduced using Fresnel's equations. The complex dielectric permittivity $\varepsilon(\omega)$ is displayed in panel d. The real part of the permittivity, $\varepsilon_1(\omega)$, which is almost frequency independent above T_C, evolves from positive to negative values for below T_C measurements, with the zero crossing taking place near ω_p. Panel e displays the real and imaginary part of the conductivity, reflecting a flat $\sigma_1(\omega)$ and a $\sim\omega_p^2/\omega$ divergence in $\sigma_2(\omega)$. The energy loss function, defined as $-\text{Im}(1/\tilde{\varepsilon}(\omega))$, is displayed in panel f. Therein, the JPR is well captured by a peak appearing at $\omega = \omega_p$. The loss function captures also another important feature of the interlayer Josephson coupling, as its width reflects the scattering rate or, equivalently, the inverse coherence length for superconducting tunneling. All these optical properties are well reproduced by the solution of the sine-Gordon equation, which are displayed in dotted lines on the plots. The simulated edge in the reflectivity and the Lorentzian shape of the Loss Function are sharper than the experimental analogues, given that the model does not account for inhomogeneous broadening that might be at play in the experiment.

I now continue reviewing the special cases of the sine-Gordon equation and the corresponding solutions, applied to the Josephson junction and the c-axis physics of cuprates.

2.3.2. Zero Frequency: the Meissner effect and the Josephson vortex lattice (Nonlinear effects)

If a static magnetic field is applied to the junction and the time dependence is disregarded ($\frac{\partial^2 \emptyset}{\partial t^2} = 0$), the sine-Gordon equation reads:

$$-\lambda_J^2 \frac{\partial^2 \emptyset}{\partial x^2} + \sin(\emptyset) = 0,$$

and describes the screening of the magnetic field by the superconducting Josephson currents.

In the limit of a short Josephson junction ($L \ll \lambda_J$), a magnetic flux can thread the junction. In this case, a Fraunhofer-type dependence of the Josephson critical current is observed [16], [28].

For long junctions ($L \gtrsim \lambda_J$) and small applied magnetic fields – H much smaller than the lower critical field, H$_{c1}$ – thus small phase, $\sin(\emptyset)$ can be approximated to $\emptyset$, and the sine-Gordon equation reduces to $\lambda_J^2 \frac{\partial^2 \emptyset}{\partial x^2} = \emptyset$, with the solution taking the form $\emptyset \sim e^{-x/\lambda_J}$. This solution incorporates the well-known *Meissner effect*: the applied magnetic field is expelled from the inside of the junction and directed towards its edges, being effectively screened by the Josephson currents.

For long junctions and large magnetic fields (H > H$_{c1}$), the junction is driven in its nonlinear regime. The small phase approximation breaks, and the phase follows $\lambda_J^2 \frac{\partial^2 \emptyset}{\partial x^2} = \sin(\emptyset)$, describing the magnetic flux penetration in the form of Josephson vortices, in which the Josephson currents are positive and negative as the phase advances in steps of 2π with a periodicity of the Josephson penetration depth, driving the tunneling current in a vortex loop. In the case of a stack of Josephson junctions, the vortices spread over more than one junction, and inductive coupling arranges the Josephson vortices in a lattice. Note that Josephson vortices are different from the so called pancake-vortices or Abrikosov-vortices which occur for magnetic fields applied along the *c*-axis and are

pinned to the ab-plane. Extending the pendulum analogy, the penetration of the Josephson vortices into the junction is equivalent to the energy transmission (in the forms of solitons) in the forbidden gap of a nonlinear chain of oscillators [29].

2.3.3. Finite Frequency: emission of THz radiation (Nonlinear effects)

One of the most interesting consequences of the physics discussed above is the emission of THz radiation for the application of a d.c. current [30]. Radiation of electromagnetic waves is rooted in the a.c Josephson effect, best depicted by the nonlinear $RCSJ$ circuit model, qualitatively described in section 2.2.

In this case, due to conservation of the current, the total current across the junction is:

$$I = I_c sin\emptyset + \frac{V}{R} + C\dot{V}$$

In the short junction model (*i.e.* spatial dependence is disregarded), this adds a source term to the sine-Gordon equation, which reads:

$$\frac{1}{\omega_p^2}\frac{\partial^2\emptyset}{\partial t^2} + \beta\frac{\partial\emptyset}{\partial t} + \sin(\emptyset) = \frac{I}{I_c},$$

Here, $\beta = L/R$ determines the damping, and $\omega_p = 1/\sqrt{LC}$ corresponds to the resonance frequency of the undamped oscillator circuit.

Below the critical current $I < I_c$, this equation has a solution $\emptyset(t) = \emptyset_0$ which is time-independent. Physically, the junction is in the zero resistance state, where superconducting carriers "short" the normal carriers.

When the junction is biased above its critical current I_c, oscillations of the tunneling current appear. The junction develops a finite voltage V_{dc} for which, according to the first Josephson relation, the phase evolves as $\emptyset(t) = \frac{2e}{\hbar}V_{dc}t$. Consequently, the Josephson current $I(t) = I_c\sin(\frac{2e}{\hbar}V_{dc}t)$ oscillates at a frequency $\nu = \frac{2e}{h}V_{dc}$ and radiation is emitted.

2.3.4. Nonlinear solutions of sine-Gordon equation by accounting for both the temporal and spatial dependences

I now turn to the limit in which none of the above approximations are valid, and space and time dependences are to be considered, together with large perturbation of the phase. In this nonlinear regime, the sine-Gordon equation exhibits travelling wave solutions, such as kink, anti-kink, small and large amplitude breathers (See Table 2.1). All these solutions are solitons, *i.e.* coherent waves that preserve their shape while propagating through a system, or after collision with other stationary waves:

- The moving kink and anti-kink solutions represent a twist of the phase from 0 to 2π (kink) or from 2π to 0 (antikink) and have the form: $\phi(x,t) = 4\arctan(\exp(\pm\frac{x-ut}{\sqrt{1-u^2}}))$, where u is their propagation speed. Here, u is dimensionless and can take values between 0 and 1. The maximum speed of propagation is defined by $c_{sw} = \lambda_J \omega_p$, where c_{sw} is called the Swihart velocity.

- The unperturbed sine-Gordon equation has also the exact solution: $\phi(x,t) = 4\arctan\left[\dfrac{sinh\left(\frac{ut}{\sqrt{1-u^2}}\right)}{u\,cosh\left(\frac{x}{\sqrt{1-u^2}}\right)}\right]$. This is a large amplitude breather, which can be viewed as a bound kink – antikink state oscillating with an internal frequency. Both the standing breather (u=0) and the moving breather (u≠0) are solutions of the equation.

All the solutions presented above were derived from the one dimensional sine-Gordon equation (*i.e.* accounting for only on spatial coordinate, x). For the solutions including two spatial dimensions see Ref. [31].

As cuprate superconductors consist of stacks of intrinsic Josephson junctions, they are expected to give rise to these nonlinear phenomena when subject to sufficiently strong terahertz fields. This problem is extensively studied in Chapter 3, both by simulation and experimental tools.
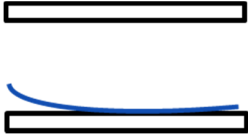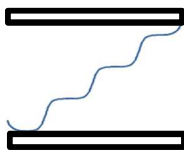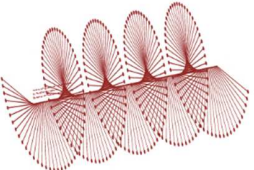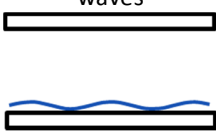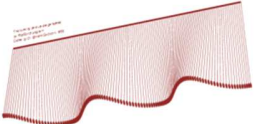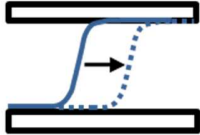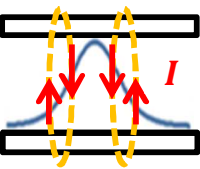
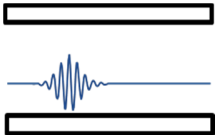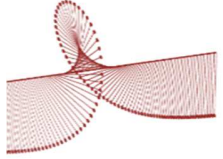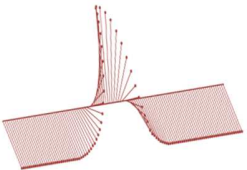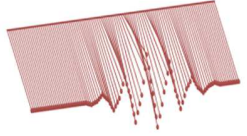|	Approximation	Sine-Gordon equation and solution	Φ in a single Josephson Junction	Phase dynamics
No time dependence $\frac{\partial^2 \emptyset}{\partial t^2} = 0$	Weak external fields $\sin(\emptyset) \approx \emptyset$	$\lambda_J^2 \frac{\partial^2 \emptyset}{\partial x^2} = \emptyset$ with solution: $\emptyset \sim e^{-x/\lambda_J}$	Meissner effect	
	Strong external fields $\sin(\emptyset) \neq \emptyset$	$\lambda_J^2 \frac{\partial^2 \emptyset}{\partial x^2} = \sin(\emptyset)$	Static vortex lattice	
Time dependent $\frac{\partial^2 \emptyset}{\partial t^2} \neq 0$	Weak external fields $\sin(\emptyset) \approx \emptyset$	$\frac{1}{\omega_p^2} \frac{\partial^2 \emptyset}{\partial t^2} - \lambda_J^2 \frac{\partial^2 \emptyset}{\partial x^2} + \emptyset = 0$ with solution: $\phi(x,t) = A e^{i(kx - \omega t)}$	Josephson plasma waves	
	Strong external fields $\sin(\emptyset) \neq \emptyset$	$\frac{1}{\omega_p^2} \frac{\partial^2 \emptyset}{\partial t^2} - \lambda_J^2 \frac{\partial^2 \emptyset}{\partial x^2} + \sin(\emptyset) = 0$ <u>Travelling wave solutions:</u> **Kink, antikink solutions** $\phi(x,t) = 4 \arctan(\exp(\pm \frac{x - ut}{\sqrt{1 - u^2}}))$ *u = the velocity of the soliton* **Large amplitude breather** $\phi(x,t) = 4 \arctan\left[\frac{\sinh\left(\frac{ut}{\sqrt{1-u^2}}\right)}{u \cosh\left(\frac{x}{\sqrt{1-u^2}}\right)}\right]$ *u = breather's velocity* **Small amplitude breather** (Its envelope is that of a large amplitude breather)	*I*	

Table 2.1: Solutions of the sine-Gordon equation together with the pictorial view of the phase dynamics in a Josephson junction.

3

Nonlinear physics of Josephson Junctions

In cuprates, superconductivity is made three dimensional by the tunneling of Cooper pairs across the CuO_2 planes trough the insulating barriers (consisting of the La, Ba, Sr, Y, *etc.* atoms). Cuprates are in fact stacks of Josephson junctions with distributed tunneling inductance, between capacitively coupled planes. The first signatures of Josephson coupling along the c-axis of cuprates were detected in $Bi_2Sr_2CaCu_2O_{8+\delta}$ [15], [16]. These d.c. transport measurements revealed the presence of multiple branches in the I-V curves, which is a signature in the response of a stack of Josephson junctions connected in series [32]. More recent experiments exposed other aspects of Josephson physics, such as: Shapiro steps, microwave emission via a.c. Josephson effect or macroscopic quantum tunneling of the Josephson phase [33], [34]. Furthermore, artificial stacks of Josephson junctions (e.g. Nb/Al-AlOx/Nb) can be prepared. In these materials, by varying the thickness of the superconducting layers, one can adjust the coupling, thus controlling the frequency of the plasma resonance.

Optical pump-probe techniques based on femtosecond lasers give important insight on the out-of-equilibrium physics of cuprates [35]. However, photons with wavelengths of 800 nm (~ 1.5 eV) can break the Cooper-pairs and induce dissipation, giving that the superconducting gap in cuprates is of the order of several milli-electronvolts (~ 30 meV) [4], [36]. For non-dissipative control, the photon used as excitation should have energies below the pair-breaking threshold, as in the case of terahertz radiation.

A recent study found that the out-of-plane conductivity of $La_{1.84}Sr_{0.16}CuO_4$ can be periodically modulated by an intense single cycle THz pump pulse of picosecond duration [37]. In this experiment, the spectrum of the incident pulse (centered at $\omega_{pump} = 450$ GHz and limited below 1.2 THz) was well below the JPR frequency of $La_{1.84}Sr_{0.16}CuO_4$ ($\omega_p = 2$ THz); thus the pump electric field, polarized along c axis, was screened as an evanescent wave within the penetration depth, $\lambda_J \sim 5\ \mu m$. However, within the length of the penetration depth, the Josephson phase was driven to high amplitudes, thus modulating the interlayer Josephson coupling. The transient complex conductivity of the perturbed material was determined as a function of pump-probe delay by time-resolved THz spectroscopy, for both in-plane and out-of-plane polarizations. The out-of-plane optical conductivity, $\sigma_c(\omega)$, was strongly modulated by the excitation, showing fast oscillations on a sub-picosecond time scale. Thus, these measurements reveal a state in which the material switches on an ultrafast timescale between superconducting and resistive states of the interlayer transport. Under this non-resonant excitation conditions, this modulation occurs only for the duration of the pump pulse. Throughout the oscillations of $\sigma_c(\omega)$, the in-plane conductivity, σ_{ab}, remains unperturbed, demonstrating the preservation of the in-plane superconductive properties (*i.e.* no Cooper pair breaking and no quasiparticle formation is observed).

Thus, the experiment presented above reported on the possibility to gate the interlayer superconducting transport by driving the Josephson phase with an intense, non-resonant THz pulse. In contrast, here, we are looking into how to control the Josephson coupling in high-T_C cuprates using THz radiation *resonant* to the plasma frequency. Tuning the excitation in resonance to the JPR discloses new interesting nonlinear phenomena, as high-amplitude Josephson plasma waves are excited and propagate into

the material. We will focus on two distinct phenomena that depend on the characteristic of the incident light:

- optical excitation of solitonic breathers occurs when $La_{1.84}Sr_{0.16}CuO_4$ is excited with intense narrow-band, long THz pulses;

- parametric amplification of Josephson plasma waves in $La_{1.905}Ba_{0.095}CuO_4$ is triggered upon excitation with broad-band, single-cycle THz pulses.

The problems are addressed both experimentally, by manipulating the phase with strong THz-frequency pulses in pump-probe configuration measurements (see Figure 3.1) and theoretically (*i.e.* by numerically solving the sine-Gordon equation, thus capturing the dynamics of the Josephson phase).The Matlab code used for the simulations is shown in Appendix B. In both experiments, the pump and probe pulses are polarized along the c-axis.
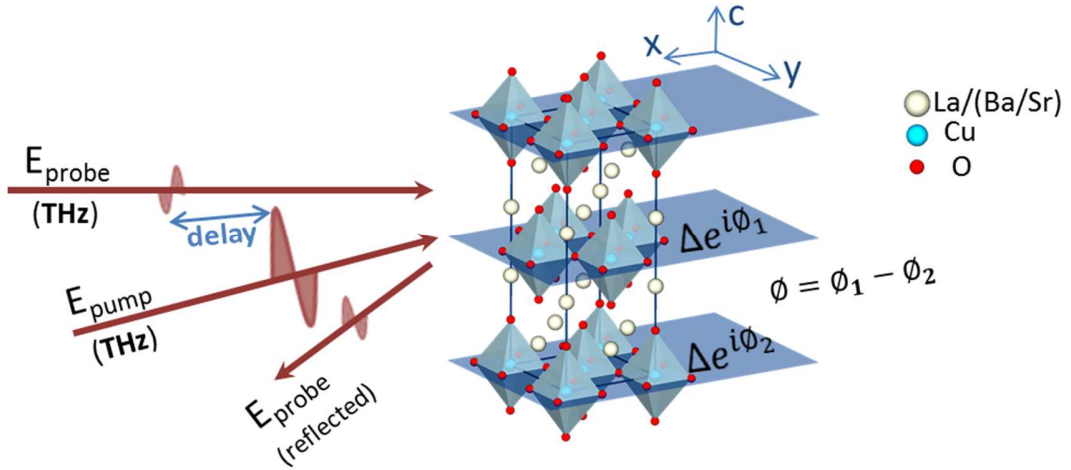
Figure 3.1: Caricature of the THz pump - THz probe configuration used for the experiments and simulations on La(Ba,Sr)CuO$_4$ samples presented in this chapter

3.1. Modeling the Josephson junction

Because radiation at photon energies below the superconducting gap of LSCO (~ 20 meV) [38] does not perturb the order-parameter amplitude (number of Cooper pairs), the electrodynamics is determined only by deformations of the space and time dependent

order-parameter phase, and it's well captured by the sine-Gordon equation described above.

For the numerical simulation, we consider a cuprate with layers stacked along the c direction (equivalent of the z-axis in the Cartesian coordinate system) and a free surface at x = 0. Input optical pump and probe pulses come at normal incidence (propagating along x-direction), with the electrical field vector in z-direction. We assume translational invariance of the system in y-direction, and the propagation of the Josephson phase difference across each layer of the cuprate is described by a one-dimensional sine-Gordon equation (see discussion in Chapter 2) which, in the presence of damping can be re-written as:

$$\frac{\partial^2 \emptyset}{\partial x^2} - \frac{1}{\gamma}\frac{\partial^2 \emptyset}{\partial t} - \frac{\varepsilon}{c^2}\frac{\partial^2 \emptyset}{\partial t^2} = \frac{\omega_p^2 \varepsilon}{c^2}\sin(\emptyset) \tag{1}$$

The Josephson phase evolution is therefore affected by the following boundary conditions at the vacuum-sample interface.

$$[E_i(t) + E_r(t)]_{x=-0} = E_c(x,t)|_{x=+0} = H_0 \frac{1}{\omega_p \sqrt{\varepsilon}}\frac{\partial \emptyset(x,t)}{\partial t}|_{x=+0} \tag{2}$$

$$[H_i(t) + H_r(t)]_{x=-0} = H_c(x,t)|_{x=+0} = -H_0 \lambda_J \frac{\partial \emptyset(x,t)}{\partial x}|_{x=+0} \tag{3}$$

The subscripts *i*, *r*, and *c* denote the incident, reflected and propagating fields inside the cuprate, respectively. Here, $H_0 = \Phi_0/2\pi D\lambda_J$, where Φ_0 is the flux quantum $\left(\Phi_0 = \frac{hc}{2e}\right)$, D is the distance between adjacent superconducting layers and λ_J is the Josephson penetration depth. In the simulations, the equilibrium plasma frequency is an input parameter chosen to be that of $La_{1.84}Sr_{0.16}CuO_4$ ($\omega_{JPR} = 2$ THz) or of $La_{1.905}Ba_{0.095}CuO_4$ ($\omega_{JPR} = 0.5$ THz).

For fields in vacuum ($x < 0$), the Maxwell's equations imply

$$E_i - E_r = \frac{\omega\mu}{ck}(H_i + H_r) = H_i + H_r \tag{4}$$

By combining equation (4) with equations (2) and (3), we obtain the boundary condition:

$$\frac{2\sqrt{\varepsilon}}{H_0}E_i(t)|_{x=-0} = \frac{\partial \emptyset(x,t)}{\omega_p \partial t}|_{x=+0} - \sqrt{\varepsilon}\frac{\partial \emptyset(x,t)}{\partial x/\lambda_J}|_{x=+0} \tag{5}$$

After solving the Josephson phase through equation (1) and equation (5), the reflected field is calculated from equation (2). The equilibrium reflectivity of the cuprate is

obtained by computing the ratio between the Fourier transforms of the reflected field and a weak input field

$$r^{equilibrium}(\omega) = E_r^{equilibrium}(\omega)/E_i(\omega) \tag{6}$$

The complex optical properties are then calculated from $r^{equilibrium}(\omega)$:

- the equilibrium dielectric permittivity takes the form:

$$\varepsilon(\omega) = \left(\left(\frac{1 - r^{equilibrium}(\omega)}{1 + r^{equilibrium}(\omega)}\right)^2\right) \tag{7}$$

- the loss function is computed as:

$$L(\omega) = -\text{Imag}\left(\left(\frac{r^{equilibrium}(\omega) + 1}{r^{equilibrium}(\omega) - 1}\right)^2\right) \tag{8}$$

In the simulation, the input field is renormalized as $E_i^{simulation}(t) = \frac{2\sqrt{\varepsilon}}{H_0}E_i(t)$ and $E_i^{simulation}(t) = 1$ corresponds to $E_i \approx 30kV/cm$.

In the following, I will first present a theoretical study (*i.e.* numerical solutions of the sine-Gordon equation) on the linear and nonlinear optical properties of the optimally doped single layer compound $La_{1.84}Sr_{0.16}CuO_4$ (T_C = 38 K). Experimental discussion will follow, with the simulations and experimental data in very good agreement. A systematic study as a function of the central frequency of the driving field is presented. Both in simulations and experiment the excitation frequency was tuned far above, close to or slightly below the plasma frequency. We conclude that the nonlinearities in the Josephson coupling get enhanced for excitation tuned into resonance with ω_p.

3.2. Linear optical excitation of Josephson Plasma Waves

For plane waves of the type $\emptyset \sim e^{i(k_x x - \omega t)}$, the dispersion relation takes the form: $k_x^2 = \frac{\epsilon_\infty}{c^2}(\omega^2 - \omega_p^2)$. For $\omega < \omega_p$, the wave vector k_x becomes imaginary and wave propagation inside the material is forbidden, due to screening. For $\omega > \omega_p$, JPWs can propagate inside the material.

In the color plot of Figure 3.2, the calculated space and time dependent phase oscillations excited by a narrowband THz pulse is displayed. The evolution of the Josephson phase $\emptyset(x, t)$ is shown on a color scale as a function of time t and depth x

inside the material. The phase evolution is calculated for an excitation of $E = 9V/cm$ at two frequencies above ($\omega = 1.1\omega_p$ and $\omega = 1.05\omega_p$) and one below the plasma frequency ($\omega = 0.97\omega_p$). The spectrum of the excitation pulse is shown in red in the upper panels of Figure 3.2, while the spatial profile at one particular time after excitation is plotted in black immediately below each two-dimensional plot.

- $\omega_{pump} \gg \omega_p$

In the linear regime, in the transparent region above the plasma resonance, $\omega_{pump} = 1.1\omega_p$, a mode is found to propagate inside the material (Figure 3.2 a.2). The estimated group velocity extracted from the simulations is $v_g = \frac{d\omega}{dk} \approx 2.5 * 10^7 m/sec$. In panel a.3, a lineout of the phase profile as a function of x is shown at a fixed time, t = 40 ps. The JPWs have a linear profile, and the amplitude in this regime does not exceed a small fraction of π.

- $\omega_{pump} > \omega_p$

For an excitation with a frequency closer to the plasma frequency, $\omega_{pump} = 1.05\omega_p$, a very similar propagating mode was found: the waves have a slightly smaller group velocity $v_g \approx 2 * 10^7 m/sec$ and similar amplitude.

- $\omega_{pump} < \omega_p$

The phase profile calculated in panel c.2, corresponds to an electromagnetic excitation with the frequency lower than the plasma frequency of the material, $\omega_{pump} = 0.97 * \omega_p$. In the weak field regime ($E = 9V/cm$) only an evanescent wave is excited, with screening occurring over a distance of less than 20 μm, as best seen in the spatial profile of the interlayer phase at 40 ps (panel c.3). As already discussed, this mode is characteristic of linear excitation below the plasma resonance.
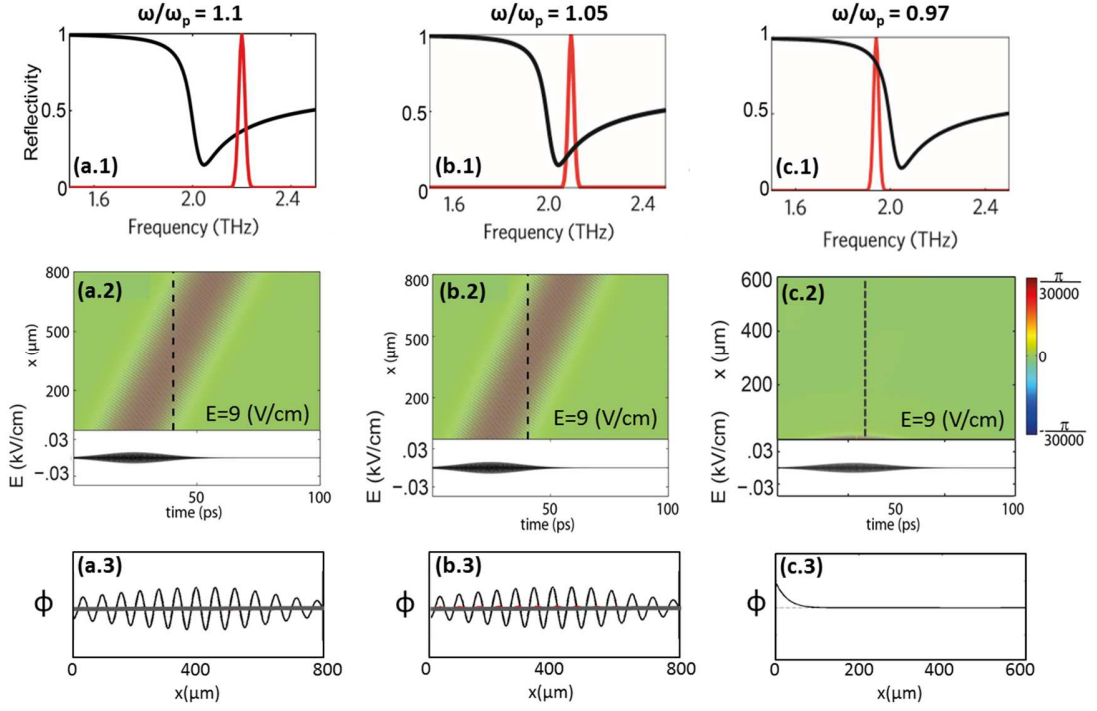
Figure 3.2: Numerical solution of the sine-Gordon equation. LINEAR regime.
Calculated space- and time-dependent interlayer phase, $\emptyset(x, t)$, as a function of pump wavelength: **a.** $\omega = 1.1\omega_p$, **b**. $\omega = 1.05\omega_p$ and **c.** $\omega = 0.97\omega_p$. The amplitude of the pump pulse is E = 9 V/cm. Upper panels show the pump spectrum (red) superimposed on the calculated equilibrium reflectivity (black) of $La_{1.84}Sr_{0.16}CuO_4$. Intermediate panels show the calculated $\emptyset(x, t)$ and the temporal profile of the pump pulse. Lower panels show selected lineouts of the phase at 40 ps.

3.3. Nonlinear dynamics of the Josephson junction; Optical excitation of Josephson Solitons

For intense fields, the electrodynamics of the JPR becomes greatly nonlinear. Figure 3.3 shows the calculated phase, $\emptyset(x,t)$, for two pump wavelengths above the plasma frequency, $\omega = 1.1\omega_p$, and $\omega = 1.05\omega_p$. The amplitude of the pump pulse is $E = 39kV/cm$.

- **$\omega_{pump} \gg \omega_p$**

Far above the plasma frequency, increasing the field strength makes little difference in the velocity of the propagating mode found in the linear regime. The amplitude of the phase reaches $\emptyset^{peak}(x,t) = \pi/10$, but the nonlinear response in this regime was found to be small (Figure 3.3 a). In panel a.3 $\emptyset(x, t = 40ps)$ is displayed in black, showing no qualitative difference from the linear response which is shown in red.

- **$\omega_{pump} > \omega_p$**

Closer to the plasma resonance (*i.e.* $\omega_{pump} = 1.05\omega_p$) the effects of a strong excitation become evident, and the phase profile is significantly perturbed. The oscillations of the phase increase and sharpen as the wave propagates into the material. Finally, the pulse-shape breaks up in a train at later times and for a propagating distance x ≥ 300 μm (panel b.2). Hence, the shape of the phase profile deviates from a plane wave shape, as further emphasized in the one-dimensional plot of $\emptyset(x, t = 50ps)$ in panel b.3. The maximum amplitude of the nonlinear phase in this case reaches $\emptyset^{peak}(x,t) = \pi/4$, twice as much as for $\omega_{pump} = 1.1\omega_p$.

- **$\omega_{pump} < \omega_p$**

Next, I will present the nonlinear dynamics of the Josephson phase calculated for pump excitation immediately below the plasma frequency, $\omega_{pump} = 0.97\omega_p$, where the most interesting results were obtained. The results are displayed in Figure 3.4, as a function of pump fluence. For fields of E = 38 kV/cm (panel a), the evanescent wave suffers a strong deformation, with the maximum phase amplitude reaching π/4. However, the material remains opaque.
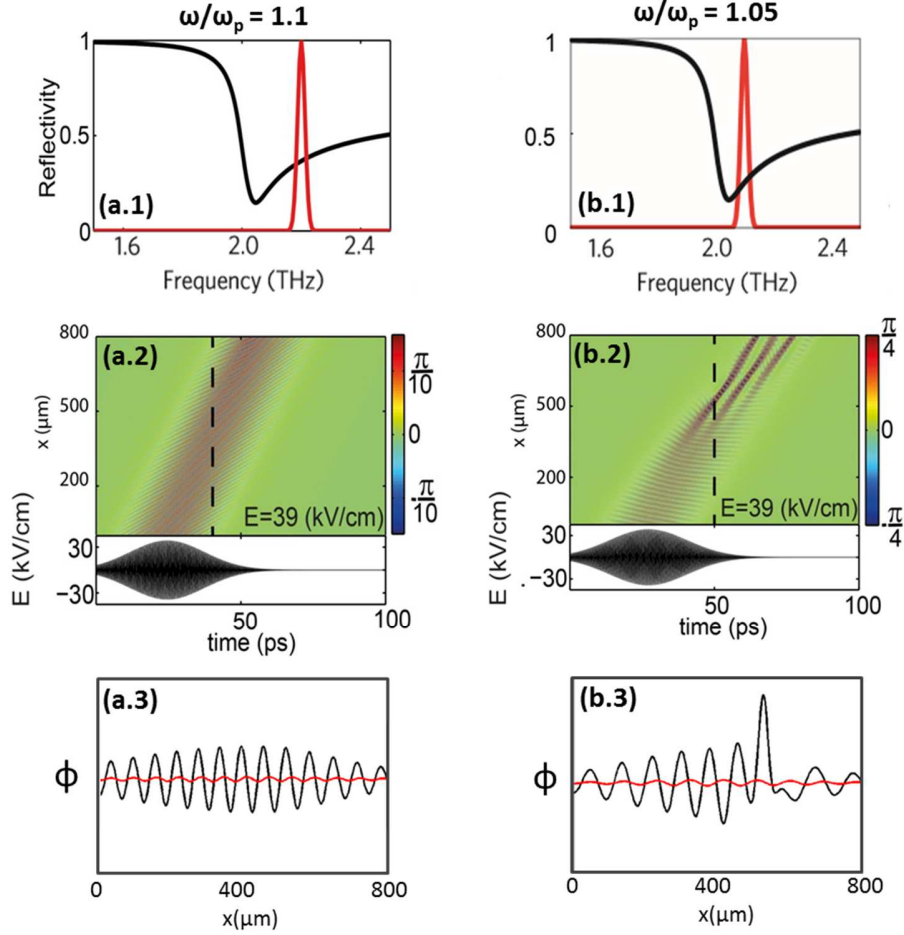
Figure 3.3: **Numerical solution of the sine-Gordon equation. Strong driving fields with $\omega_{pump} > \omega_p$.** Calculated space- and time-dependent interlayer phase, $\emptyset(x,t)$, for E = 39 kV/cm tuned at two pump wavelengths above the plasma frequency: a. $\omega = 1.1\omega_p$, and b. $\omega = 1.05\omega_p$. Upper panels show the pump spectrum (red) superimposed on the calculated equilibrium reflectivity (black) of La$_{1.84}$Sr$_{0.16}$CuO$_4$. Intermediate panels show the calculated $\emptyset(x,t)$ and the temporal profile of the pump pulse. Lower panels show in black selected line cuts of the phase at t = 40 ps for $\omega = 1.1\omega_p$ (a.3) and 50 ps for $\omega = 1.05\omega_p$ (b.3). In red, the linear response in the same excitation conditions is presented for comparison.

Remarkably, for E = 39 kV/cm a propagating mode emerges, as can be seen in the two-dimensional plot in panel b.1. Spatial line cuts of the phase for 50 and 55 ps time delay (panel b.2) show a single solitonic mode of amplitude $\emptyset^{peak}(x,t) = \pi/4$. The propagating mode evolves from the exponentially evanescent wave at early times and concentrates the electromagnetic energy in space and time without any noticeable distortion of its shape as it propagates. This mode (*i.e.* Josephson Plasma Soliton, JPS), is a *breather* solution of the sine Gordon equation (see discussion in Chapter 2). As previously discussed, the *breather* can be thought of as pair of oppositely-oriented phase kinks, or a bound vortex anti-vortex pair. Note that the unbound vortex anti-vortex pair would correspond to two oppositely-phased 2π phase kinks, whereas the peak of the bound state is $\pi/2$, corresponding to a lower total energy. The JPS propagates close to the surface of the material, $x < 100\mu m$, at a group velocity of $v_g = 8 \cdot 10^5$ m/s. As the field strength is further increased to 42 kV/cm (panel c), the velocity of the soliton increases, with the breather propagating deep in the material, x > 600 μm. Also, the peak phase increases to $\emptyset^{peak}(x,t) = \pi/2$. A first conclusion is that the velocity of the breather is an extremely steep function of the excitation field.

At even higher fields more than one soliton is launched during the pulse. For E = 50 kV/cm, two solitons are obtained, with a fast soliton penetrating into the material and a slow soliton propagating close to the surface. The second soliton is injected 10 ps after the first one, and has smaller amplitude. Increasing the excitation field even higher gives rise to a train of fast solitons, as seen for E = 75 kV/cm (panel e) and E = 100kV/cm (panel f). Thus, the characteristics of the solitons (such as their precise shape, their propagation velocity or oscillation frequency) depend sensitively on the excitation conditions. Also, the prompt emergence of the breather at E = 39 kV/cm indicates that the injection of solitons inside the material is a threshold phenomenon. Further discussion will follow.

As a mechanical analogue, it is worth mentioning that Geniet and Leon [29], [39] experimentally showed the nonlinear transmission of energy in the forbidden gap of a chain of oscillators. The process occurred above a threshold amplitude of the external driving which in many cases is exactly predictable, as demonstrated both numerically (from sine-Gordon calculations) and experimentally, by driving the chain of oscillators

coupled by a coil spring by one end and observing the emergence of the nonlinear modes.
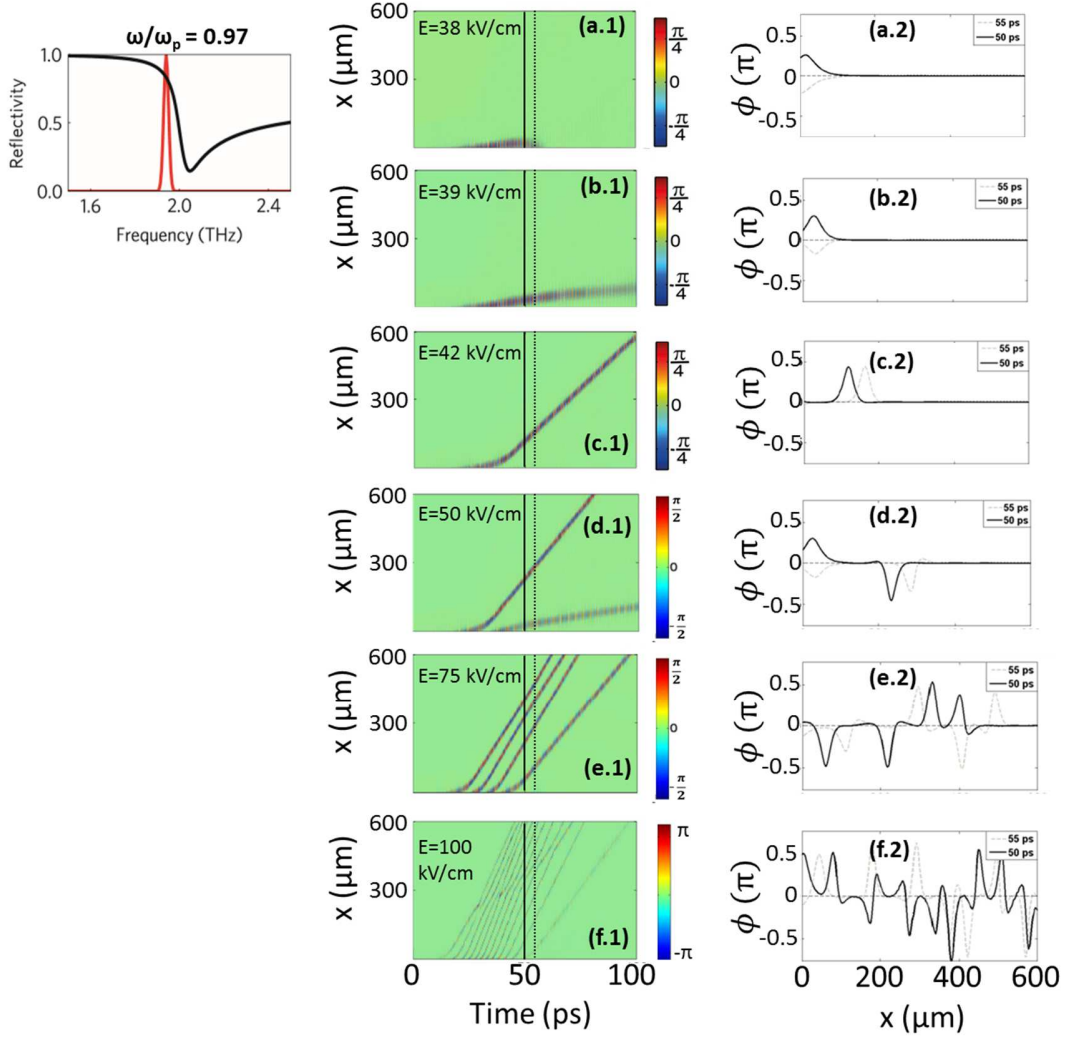
Figure 3.4: Numerical solution of the sine-Gordon equation. NONLINEAR regime, $\omega_{\text{pump}} \leq \omega_p$. Calculated space- and time-dependent interlayer phase, $\emptyset(x, t)$, for a pump wavelength below the plasma frequency, $\omega = 0.97\omega_p$ is presented as a function of pump fluence: **a**. E = 38 kV/cm, **b.** E = 39 kV/cm, **c**. E = 42 kV/cm, **d.** E = 50 kV/cm, **e.** E = 75 kV/cm, **f.** E = 100 kV/cm. The left panel shows the pump spectrum (red) superimposed on the calculated equilibrium reflectivity (black) of La$_{1.84}$Sr$_{0.16}$CuO$_4$. Right panels show selected lineouts of the phase for t = 50 ps (solid) and t = 55 ps (dashed lines) for each pump fluence.

Breather intrinsic frequency

In Figure 3.5 a caricature of a JPS is presented in which two Josephson vortices, kink and antikink, propagate along the planes oscillating against one another at a frequency determined by the strength of the binding. As a consequence, the peak of the phase pulse oscillates between positive and negative values, with an intrinsic frequency of the breather $\sim \omega_p$, thus with a period of only few hundred femtoseconds, ~ 500 fs. In a cuprate (*i.e.* in a stack of long Josephson junctions), the breathers extend over many layers and are not confined between two planes. The magnetic field associated to the resulting breather is presented in red and is confined in the ab-planes of the cuprate.
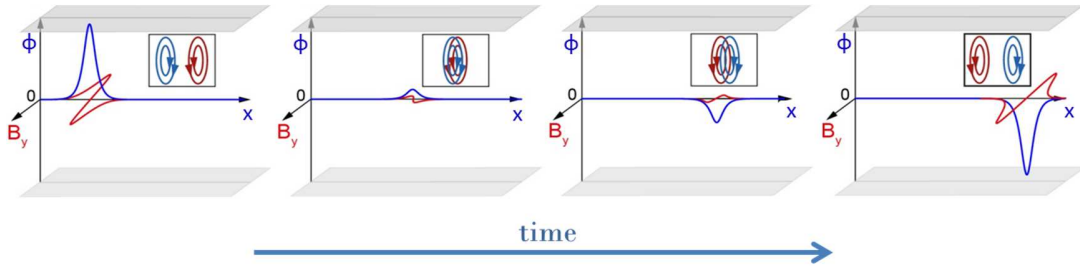
Figure 3.5: Pictorial representation of a Josephson breather as it propagates in time. A bound kink - antikink pair (blue), with associated oppositely phased magnetic fields along the y axis (red) oscillates as it propagates. The equivalent representation in terms of oscillating vortex anti-vortex pair is included in the insets.

Threshold field for breather formation

As mentioned above, the prompt injection of the first breather that propagates into the material suggests that a threshold amplitude of the driving field is required for soliton formation. To further investigate this matter, we consider an oscillating electric field of constant amplitude E = 50 kV/cm (left panel of Figure 3.6) that excites the sample in the same geometry as before.

The solitons are injected in the material at a constant rate, as depicted in the two dimensional plot on the left panel of Figure 3.6. We define τ as the time between the appearances of two consecutive breathers. In the middle panels we plot τ as a function of

excitation amplitude, for three field frequencies: $\omega_{pump} = \omega_p$, $\omega_{pump} = 0.97\,\omega_p$, and $\omega_{pump} = 0.95\,\omega_p$. The decay of τ with increasing field amplitude obeys the formula:

$$\tau \propto (E - E_{threshold})^{\alpha}.$$

This equation provides very good fits to the data (red lines), which return the threshold values: $E_{threshold} = 5$, $E_{threshold} = 21$ and $E_{threshold} = 30\,kV/cm$ for $\omega_{pump} = \omega_p$, $\omega_{pump} = 0.97\,\omega_p$, and $\omega_{pump} = 0.95\,\omega_p$ respectively. In the right panels the quantity $\tau^{1/\alpha}$ as a function of field amplitude is shown to correctly be fit by a linear function, as expected. Note that τ is defined only if two or more breathers are injected in the material, thus the threshold values correspond to the first two breathers being formed. For only one breather to be injected, one expects lower values. The lowest value for the threshold field is registered when the frequency of the excitation is tuned in resonance with the plasma frequency. Consequently, it strongly increases as you go further from the JPR: a 5% decrease in the pump frequency accounts in a six time increase of the amplitude field needed for breather formation. Also, for higher fields, there is a saturation in the breather formation, as the breather's velocity cannot exceed the Swihart velocity, $c_{sw} = \lambda_J \omega_p$ (depicted in dark blue on the two dimensional plot).
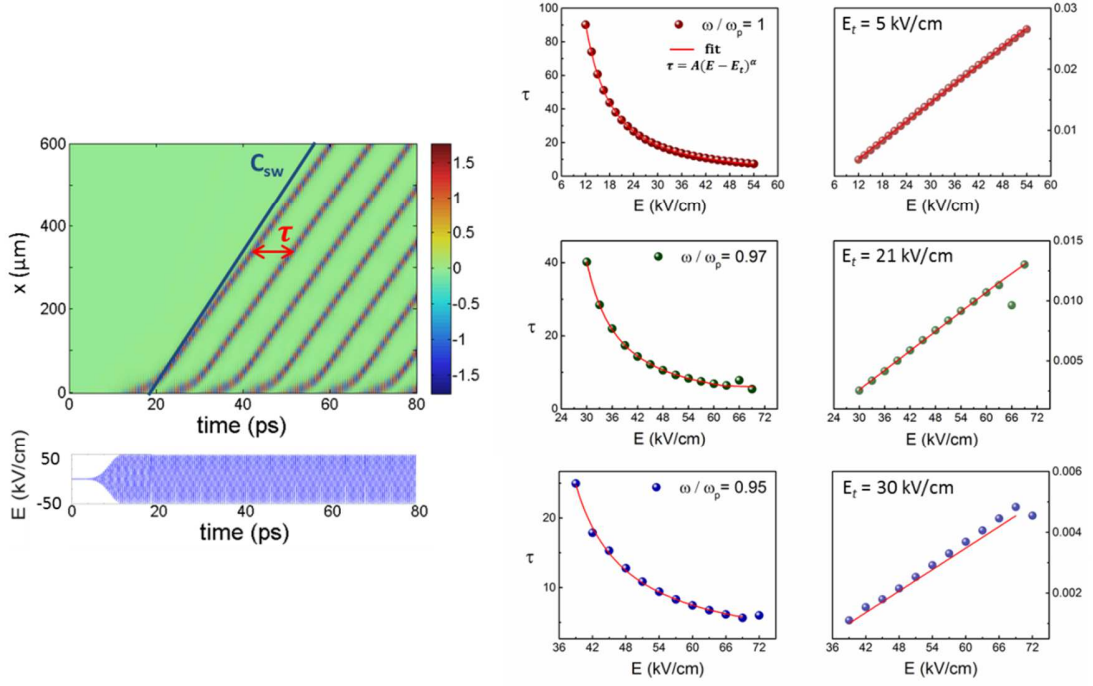
Figure 3.6: Threshold behavior of breather formation. Left: Calculated space- and time-dependent interlayer phase, $\emptyset(x,t)$, for a pump wavelength $\omega = 0.97\omega_p$ and field $E \approx 50\ kV/cm$ with the profile shown in the lower panel. τ is the time between 2 breather formations and c_{sw} is the Swihart velocity; **Middle**: Simulation of the pump field amplitude dependence of τ, for three field frequencies $\omega = \omega_p$, $\omega = 0.97\omega_p$, and $\omega = 0.95\omega_p$. Red lines are fits to the data, following the formula $\tau = (E - E_{threshold})^{\alpha}$. **Right**: the quantity $\tau^{1/\alpha}$ shows a linear dependence on the field amplitude.

Simulating the transient optical response at THz frequencies

After studying the different modes that can be excited in a high-T_C cuprate by an external narrow band THz pulse, we will now discuss simulations of the transient properties of the sample, by employing a second, weak broad band THz pulse, impinging onto the sample after a certain time delay. All experiments and simulations in this thesis are performed in a so-called pump-probe configuration, which is explained in Appendix A.

In the simulations, for the pump-probe configuration, we consider that the input field is the sum of the pump and probe fields (with a defined delay between them):

$$E_i(t) = E_{pump}(t) + E_{probe}(t) \tag{9}$$

Correspondingly, the Josephson phase can be written as

$$\emptyset = \emptyset_{pump} + \emptyset_{probe} \tag{10}$$

Substituting this equation in the sine-Gordon equation and using the relation $\sin(\emptyset_{pump} + \emptyset_{probe}) = \sin(\emptyset_{pump})\cos(\emptyset_{probe}) + \cos(\emptyset_{pump})\sin(\emptyset_{probe})$, one obtains two coupled equations:

$$\frac{\partial^2 \emptyset_{pump}(x,t)}{\partial x^2} - \frac{1}{\gamma}\frac{\partial \emptyset_{pump}(x,t)}{\partial t} - \frac{\varepsilon_r}{c^2}\frac{\partial^2 \emptyset_{pump}(x,t)}{\partial t^2}$$
$$= \frac{\omega_p^2 \varepsilon_r^2}{c^2}\sin \emptyset_{pump}(x,t)\cos \emptyset_{probe}(x,t) \tag{11}$$

$$\frac{\partial^2 \emptyset_{probe}(x,t)}{\partial x^2} - \frac{1}{\gamma}\frac{\partial \emptyset_{probe}(x,t)}{\partial t} - \frac{\varepsilon_r}{c^2}\frac{\partial^2 \emptyset_{probe}(x,t)}{\partial t^2}$$
$$= \frac{\omega_p^2 \varepsilon_r^2}{c^2}\sin \emptyset_{probe}(x,t)\cos \emptyset_{pump}(x,t) \tag{12}$$

For a weak probe ($\emptyset \ll 1$), $\cos \emptyset_{probe} \approx 1$ and the effect of $\emptyset_{probe}$ on $\emptyset_{pump}$ can be neglected in Equation (11). Thus, $\emptyset_{pump}$ and $\emptyset_{probe}$ are calculated as follows:

- Equations (11) and (5) are solved with the driving field $\mathbf{E_i = E_{pump}}$ to get $\emptyset_{\mathbf{pump}}(\mathbf{x, t})$;

- Equation (12) and (5) are solved by substituting $\emptyset_{\mathbf{pump}}(\mathbf{x, t})$ with the input field $\mathbf{E_i = E_{probe}}$, to obtain $\emptyset_{\mathbf{probe}}(\mathbf{x, t})$ and the reflected probe field $\mathbf{E_r^{perturb}}$. The reflectivity of the transient state is given by:

$$r^{perturb}(\omega, t) = \frac{E_r^{perturb}(\omega, t)}{E_i(\omega)}. \tag{13}$$

The optical response functions of the perturbed material are extracted from the complex optical reflectivity $r^{perturb}$.

- the transient dielectric permittivity takes the form:

$$\varepsilon(\omega) = \left(\left(\frac{1 - r^{perturb}(\omega)}{1 + r^{perturb}(\omega)} \right)^2 \right) \tag{14}$$

- while the perturbed loss function is calculated as:

$$L(\omega, t) = -\text{Imag}\left(\left(\frac{r^{perturb}(\omega, t) + 1}{r^{perturb}(\omega, t) - 1} \right)^2 \right) \tag{15}$$

The steady-state optical properties obtained from the simulations were presented in detail in Chapter 2, where I introduced the concept of Josephson Plasma Resonance (see Figure 2.3). We will focus here on the transient properties that the material exhibits upon excitation, with emphasis on the loss function, which exhibits a clear peak at the plasma frequency in the equilibrium superconducting state.

Figure 3.7 shows the frequency-dependent loss function of the material as a function of pump-probe delay, for a nonlinear excitation (E = 39kV/cm) tuned above the plasma frequency.

- $\boldsymbol{\omega_{pump} \gg \omega_p}$

For excitation pulses with the central wavelength far above the plasmonic frequency, *i.e.* for $\omega_{pump} = 1.1 \, \omega_p$, simulations predict a slight shift to the red of the loss function during and immediately after the pump pulse.

- $\boldsymbol{\omega_{pump} > \omega_p}$

The effect increases as the pump wavelength is tuned closer to the plasma resonance, *i.e.* for $\omega_{pump} = 1.05 \, \omega_p$. Remember that in this case, fast nonlinear waves are propagating into the material and interact with the probe pulse. At later delays, after the pump pulse has propagated beyond the probe penetration depth, no significant effect appears. The redshift is readily understood by qualitative considerations: as the tunneling current depends nonlinearly on the phase difference ($J \propto sin\emptyset$), the inductance follows as

$L \propto 1/cos\emptyset$, and in turn the Josephson plasma resonance frequency decreases as $\omega_p = 2\pi/\sqrt{LC}$. Thus, the plasma frequency shifts towards lower frequencies for strong excitation fields [40].
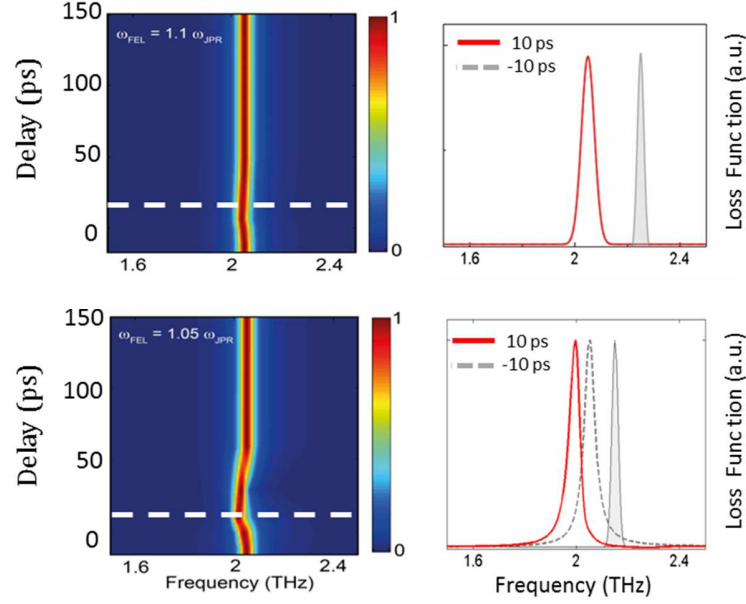
Figure 3.7: Calculated frequency and time-dependent loss functions, for $\omega_{pump} > \omega_p$. The pump amplitude is of E = 39 kV/cm and pump wavelength of $\boldsymbol{\omega = 1.1\omega_p}$ (upper panels) and $\boldsymbol{\omega = 1.05\omega_p}$ (lower panels). On the right hand side, lineouts depict the loss function before (-10ps) and after (+10ps) pump excitation. The shaded line is a Gaussian fit to the pump spectrum.

- $\boldsymbol{\omega_{pump} < \omega_p}$

For an excitation pulse with the central wavelength immediately below the plasma frequency, we showed a plethora of emergent phenomena (e.g. nonlinear evanescent wave, slow and fast moving breathers, train of breathers), depending on the fluence of the pump pulse. In Figure 3.8 the loss functions as a function of pump-probe delay are presented for three selected fluences, as obtained from the simulations. For all excitation fluences, during the pump pulse (t < 50 ps), as the probe interacts with the highly nonlinear waves, the simulations predict a strong reshaping of the loss function,

accompanied by a pronounced broadening.

At time delays after the excitation (t > 50 ps), the loss function goes back to the equilibrium position for pump fluences of 38 kV/cm and 75 kV/cm. On the contrary, for an amplitude of 39 kV/cm of the excitation pulse, a long-lived dip in the loss function line shape is observed. In this case, the emerged soliton propagates slowly through the material (the mode is presented in Figure 3.4 b), thus it interacts with the probe pulse on a long timescale. The first remark is that the long-lived perturbation observed in the loss function is highly sensitive to the field strength. This comes directly from the sensitive dependence of the soliton velocity on the amplitude of the applied excitation: a fast soliton escapes the probe penetration depth within the duration of the pump pulse and does not interact with the probe pulse after t = 50 ps. Lineouts for the loss functions at 80 and 100 ps time delay are compared on the right hand side plots of Figure 3.8. Note that the dip is very pronounced at 80 ps, and slowly reduces with increasing time delay, but it is still apparent at 100 ps. The calculated decay time of the dip is 40 ps, that matches the escape time of the soliton from the probed volume (5-20 μm depending on the wavelength).

The split lineshape with a dip is understood by considering the optical properties of the solid in presence of the soliton. Interference occurs throughout the spectrum, resulting from the interaction between the soliton (for which $\emptyset(x,t) \gg 0$) and the Josephson plasma waves (*i.e.* $\emptyset(x,t) \sim 0$) employed to probe it. The dip in the loss function is analougus with a Fano-like lineshape observed in physical systems in which continuum excitations are anharmonically coupled to discrete ones [41]–[43].
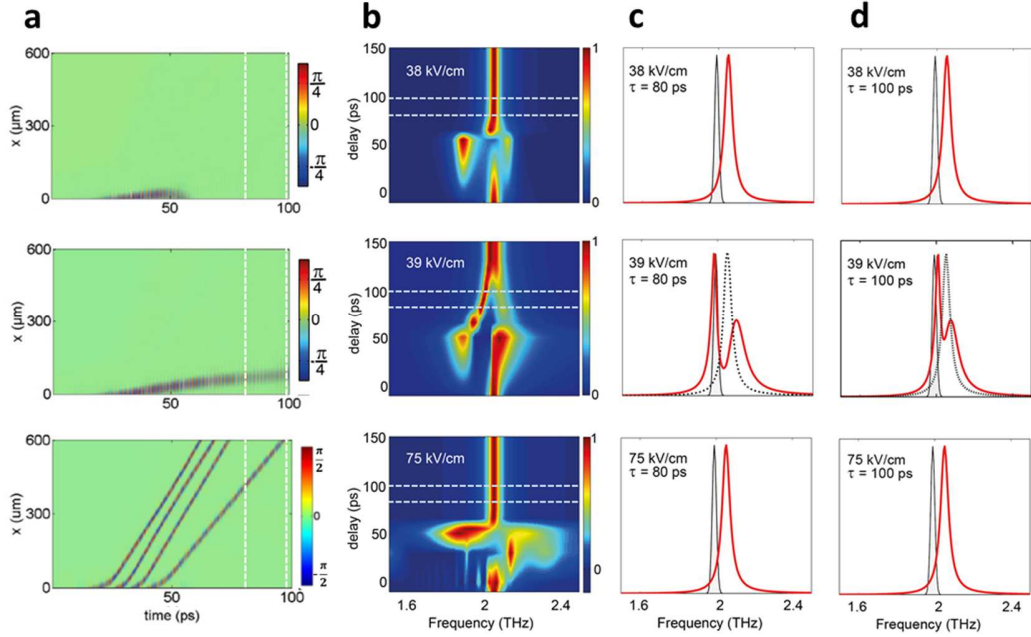
Figure 3.8: Calculated frequency and time-dependent loss functions, for ω$_{pump}$<ω$_p$
a. Calculated space- and time-dependent interlayer phase, $\emptyset(x, t)$, for a pump wavelength, $\omega = 0.97\omega_p$ and three different excitation field strengths. **b**. Corresponding frequency and time delay dependent loss function. The lineouts displayed on the right hand side depict the perturbed loss function at 80ps (**c**) and 100 ps (**d**) time delay (red curves), compared to a Gaussian fit to the pump spectrum, shaded. The gray dotted lines show the equilibrium loss function.

3.4. Experimental implementation

The strong reshaping of the loss function was also experimentally observed, validating the simulations discussed above. I will now present experimental data acquired and analyzed by Andreas Dienst and coworkers at the FELBE THz Free Electron Laser (FEL) [44]. The FEL emitted intense, narrowband (Δω/ω~1%) pulses of 25-ps duration, and could be tuned around the 2-THz Josephson Plasma Resonance (JPR) of the La$_{1.84}$Sr$_{0.16}$CuO$_4$ sample measured. The resulting transient excited state of the cuprate was then probed in the time domain using single-cycle, broadband THz pulses, which were generated by a photoconductive antenna illuminated with a femtosecond laser. Both pump and probe fields were polarized along the c axis, perpendicular to the superconducting planes.

The excitation by the FEL could be tuned around the plasma resonance, at $\omega_{pump} = 1.1\,\omega_p, \omega_{pump} = 1.05\,\omega_p$ and $\omega_{pump} \sim \omega_p$. The Free Electron Laser wavelength was measured by using a grating spectrometer, which allowed for a precision better than 1%. The pump pulse peak strength was about 10 kV/cm.

For the equilibrium, linear properties of unexcited bulk $La_{1.84}Sr_{0.16}CuO_4$, review Figure 2.3 and the corresponding discussion. I will now proceed with presenting the pump-induced effects and discuss the similarities between experiment and simulations. Thus, the time-dependent optical properties of the photo-excited superconductor are extracted as follows.

Firstly, the incident electric field was calibrated, by measuring it after reflection from a gold-coated portion of the sample. Further, the frequency-dependent reflectivity is derived as $r^{equilibrium}(\omega) = E_r^{equilibrium}(\omega)/E_i(\omega)$. For the transient state, the non-equilibrium reflectivity is extracted as $r^{equilibrium}(\omega) + 6\Delta r(\omega)$. We use 6 as a scaling factor, because the response is probed at 78 MHz, while the pump repetition rate is only 13 MHz; thus, only one pulse out of six probes the light-induced dynamics. The transient response was fitted by taking into account the mismatch between the penetration depth of the pump and probe pulses, with a model that considers a surface layer of unknown permittivity over an unperturbed semi-infinite superconductor. This procedure will be further used in this thesis for data analysis and it is presented in Ref. [45]. From these measurements, the time- and frequency-dependent loss function is extracted, as displayed in Figure 3.9. All observations qualitatively follow the simulations presented above. When the free electron laser is tuned well above the Josephson plasma frequency, $\omega_{pump} = 1.1\,\omega_p$, the loss function remains unperturbed (panel a). However, for excitation just above the resonance, $\omega_{pump} = 1.05\,\omega_p$, a rigid shift of the loss function to lower frequencies can be observed (panel b). Good agreement is found in between theoretical and experimental loss functions for all the above-resonance excitation wavelengths. As in the case of the simulations, the dynamics are short-lived and persist only as long as the pump field is present. In the experiment, the resolution is not as sharp as in the simulations, and the red shift is clearly visible only for $\omega_{pump} = 1.05\,\omega_p$. The red-shift of the resonance achieved here experimentally was theoretically predicted in the literature as self-induced transparency [46].
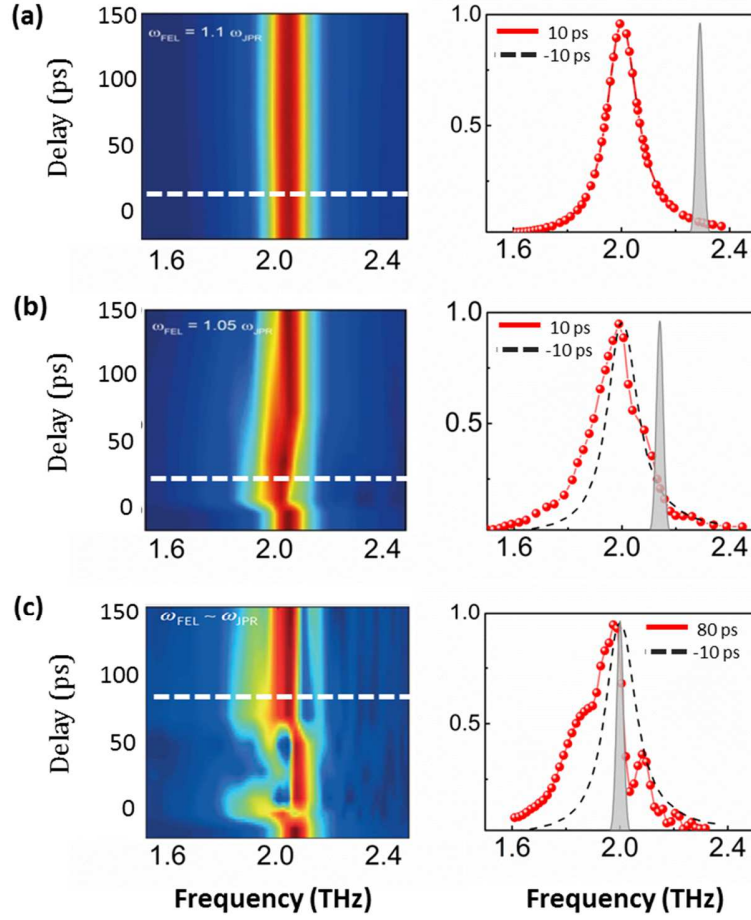
Figure 3.9: Experimental frequency and time-dependent loss functions. Left: Two dimensionnal plots representing the time evolution of the frequency resolved loss function as a function of pump-probe delay for different pump wavelengths: (a) $\omega_{pump} = 1.1\,\omega_p$, (b) $\omega_{pump} = 1.05\,\omega_p$ and (c) $\omega_{pump} \sim \omega_p$. **Right**: Respective selected lineouts before (dotted black lines) and after (red dots) excitation. The shaded curve represents a Gaussian fit to the pump spectrum.

As in the case of the simulations, the experimental data show that tuning the excitation just below the plasma resonance ($\omega_{pump} \sim \omega_p$) triggers the most nonlinear response. During the first 50 ps, the time-dependent loss function shows a broadening to the red, accompanied by a strong re-shaping. After the pump pulse (*i.e.* in the un-driven regime), for time delays greater than 50 ps, the formation of a long-lived dip similar to the one predicted by the simulations is observed, extending over the whole temporal window of the measurement (which corresponds to a delay between pump and probe of 150 ps). A first important observation is that incoherent quasi-particle excitations cannot be

responsible for this peculiar line-shape in the loss function. In the sine-Gordon equation, the quasi-particle damping is taken into account in the term $\frac{1}{\gamma}\frac{\partial^2 \emptyset}{\partial t}$, with γ being a damping constant. Thus, quasi-particle excitations could only act towards broadening the loss-function linewidth.

In the following, the loss function measured experimentally for $\omega_{pump} \sim \omega_p$ is compared to the one predicted by the calculations. The main features are closely reproduced by the simulations, albeit some quantitative differences are apparent:

- Firstly, the experiments are performed at pump frequencies of $\omega^{exp}_{pump} \sim \omega_p$, but are best described by calculations performed at $\omega^{simulation}_{pump} = 0.97\omega_p$. Note that the confidence level on the relative calibration of the pump wavelength and the probe is approximately 1%, difference which appears to be significant.

- Simulations cannot reproduce accurately the dynamics of the optical response during the pump pulse (delays < 50 ps), due to the high nonlinearity. However, there is a clear broadening of the loss function in this regime.

- As already discussed, the main feature represented by the dip in the loss function at time delays after the excitation (t > 50 ps), is predicted by simulations. The calculated decay time of the dip is ~ 40 ps, as opposed to the measured value of 150 ps. Thus, simulations overestimate the velocity of the breather by a factor of 3 to 4. This could be qualitatively explained by the fact that in real materials disorder may cause the soliton to slow down further from the ideal case, represented by the single Josephson junction without disorder.

- In the calculations, the formation of a slow soliton (which causes the long lived dip) occurs for an excitation field of 39 kV/cm, four times higher than the pump field used in the experiment, 10 kV/cm. Thus, experimental conditions seem to favor the nonlinear coupling of the light into the material. This might be also because the cuprate is approximated by a stack of Josephson junctions which may amplify the nonlinearity, while in the simulations we only consider one junction.

- The experimental linewidth of the loss function for delays > 50 ps is broader than the one obtained in the simulations, and it also shows a low-frequency shoulder not reproduced by the theory. As already mentioned, this could be the effect of

inhomogeneous broadening which plays a role in the experiment.

The main observation of this work is that, by exciting a $La_{1.84}Sr_{0.16}CuO_4$ sample with narrow-band pulses centered at the 2 THz JPR, optical signatures of soliton formation are observed. The theoretical work is in very good agreement with the experimental measurements.

In the following, we turn our attention to *broadband* THz pump pulses, and investigate the effect a resonant excitation of this type has on layered cuprates. The broad-band pulses are obtained here by tilted pulse front technique in lithium niobate ($LiNbO_3$) (see Appendix A.4). This allows for generating THz pulses with a typical spectrum centred around 0.5 THz (Figure 3.10 a, green curve). In order to be resonant to the JPR of the system, the sample chosen was $La_{1.905}Ba_{0.095}CuO_4$, for which the JPR is at ~ 0.5 THz. All experimental data are supported by simulations.

3.5. Parametric amplification of Josephson Plasma Waves

When a low amplitude broadband THz pump pulse is tuned resonantly with the JPR, JPWs propagate into the material (see discussion in Chapter 2). These waves are linear, as the phase is much smaller than 1, corresponding to the regime where the Josephson tunneling could be approximated as $\sin(\emptyset) \approx \emptyset$. If the pump field is increased to a few tens of kV, high amplitude Josephson plasma waves are excited and propagate within the penetration depth of the superconductor. *Here, I will show that Josephson Plasma Waves in cuprate superconductors can be driven to large amplitudes. In this regime phase fluctuations are parametrically amplified*. This is shown by simulating the sine-Gordon equation in the same manner as presented in Section 3.1 of the current chapter, and is achieved experimentally in barium-doped lanthanum single-layer copper oxide ($La_{1.905}Ba_{0.095}CuO_4$) when it is illuminated with an intense broadband THz pump pulses tuned in resonance with the plasma frequency of the material. The equilibrium value for the plasma frequency of $La_{1.905}Ba_{0.095}CuO_4$ is $\omega_{p0} = 0.5\,THz$, as seen by measuring the c-axis equilibrium optical reflectivity (Figure 3.10, panel a). For the pump-probe configuration, both pump and probe were polarized perpendicular to the Cu-

O planes, maintaining the geometry of the previously presented experiment. The results of the simulations are presented at first.

According to the second Josephson equation, the interlayer phase difference, $\emptyset(t)$, advances in time with the integral of an applied voltage. Thus, for a sinusoidal electric field of the form $E = E_0 \sin(\omega_{p0} t)$, if one disregards the spatial dependence, one can write the interlayer phase difference as:

$$\emptyset(t) = \frac{2eE_0 d}{\hbar\omega}\cos(\omega_{p0} t) = \emptyset_0 \cos(\omega_{p0} t). \tag{16}$$

Correspondingly, the oscillator strength, $f \sim \omega_p^2$ for the plasma oscillations also becomes a function of the interlayer phase, and takes the form:

$$f(t) = f_0 \cos\left(\emptyset_0^2 \cos(\omega_{p0} t)\right) \tag{17}$$

$$\approx f_0\left((1 - \emptyset_0^2 - \emptyset_0^2 \cos(2\omega_{p0} t))/4\right).$$

Thus, although in linear response the plasma frequency is $\omega_{p0}^2 = \frac{1}{L_0 C}$, for stronger electric fields, as the phase difference ($\emptyset_0$) becomes sizeable, one expects a redshift of the plasma resonance (*i.e.* an average reduction of the interlayer coupling strength) and a modulation of the oscillator strength at twice the JPR frequency, $2\omega_{p0}$. For La$_{1.905}$Ba$_{0.095}$CuO$_4$ the interlayer spacing is ~ 1nm and, in the case of ~ 1ps period of the applied field (1 THz frequency), sizeable phase $\emptyset_0$ are expected for only a few tens of kV/cm fields, according to the second Josephson equation.

Going back to the sine-Gordon equation, which accounts for both temporal and spatial coordinates of the phase, it reads:

$$\frac{\partial^2 \emptyset(x,t)}{\partial t^2} = -\omega_p^2 \sin(\emptyset_0 \cos(\omega t)). \tag{18}$$

Figure 3.10 displays solutions of the sine Gordon equation for two pump fluences. In the linear regime (E << 1 kV/cm), the space and time dependent phase propagates into the superconductor as plasma waves. In this limit, the oscillator strength remains virtually unaltered (panel b.2). In the case of strong electromagnetic fields (E ~ 200 kV/cm), calculations show the excitation of large phase amplitudes. One can observe an average reduction of the oscillator strength and a clear oscillatory modulation at $2\omega_p$ (panel c.2).
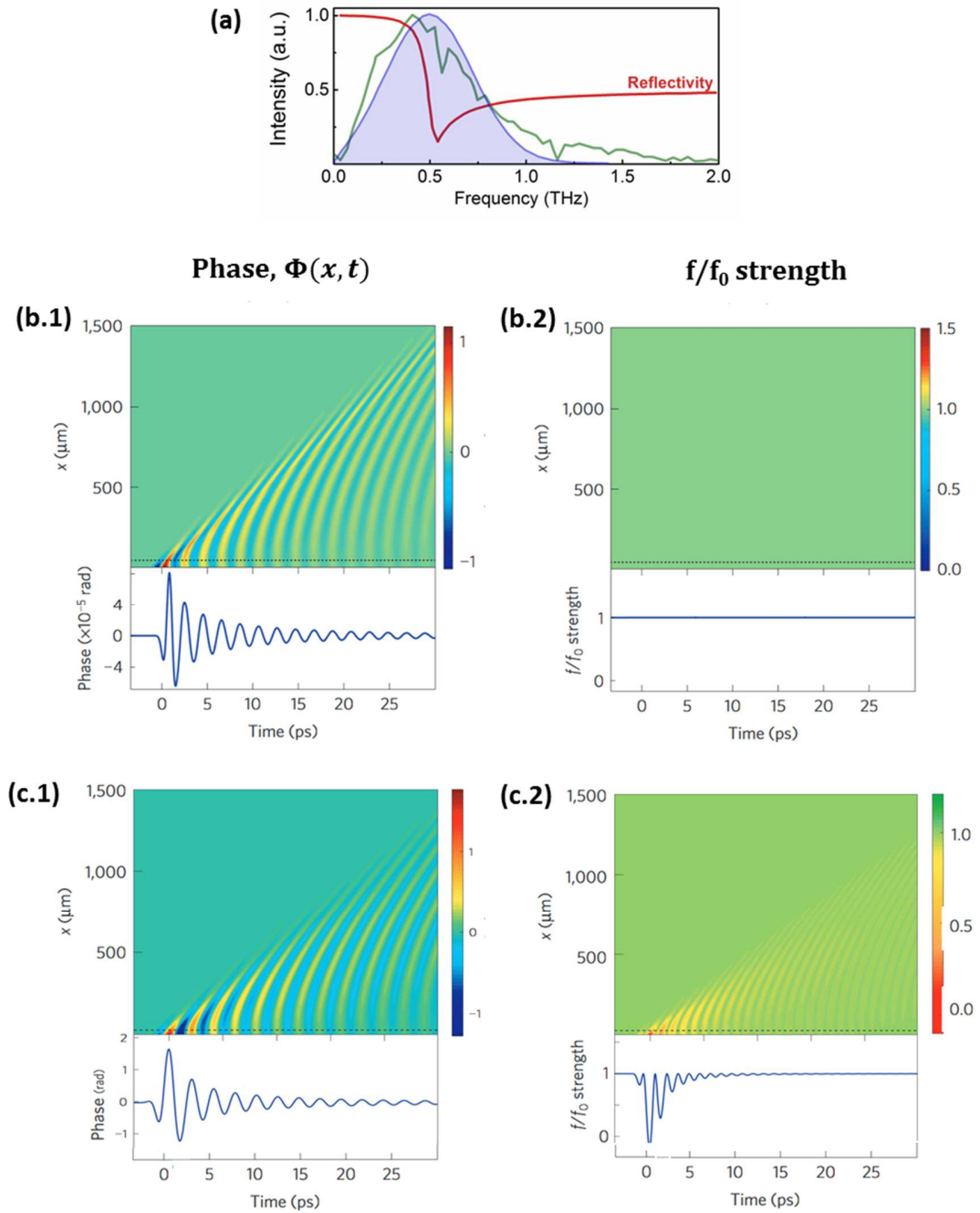
Figure 3.10: a. Comparison between the Fourier spectrum of the THz pulse (purple area) used for simulations and the JPR characterized by a plasma an edge in the reflectivity (red curve). The green line is the THz pulse used in experiments. **b-c.** Solutions of the sine-Gordon equation in the linear and nonlinear regimes: **b.1** Simulated phase $\emptyset(x, t)$ induced by a weak probe THz field. **b.2** The interlayer superfluid inductance (or a measure of the oscillator strength). **c.1** and **c.2** are the corresponding plots for strong pump THz field used in the experiment.

We will now focus only on the nonlinear dynamics induced in the sample, *i.e.* by using electric fields $E > 30 kV/cm$. In Figure 3.11, we report the measured response upon sample excitation with pump pulses having peak field strengths of 40 and 80 kV/cm (enough to drive the phase close to $\emptyset_0 \sim \pi/2$). Panel a.1 shows the frequency-integrated THz probe pulse as a function of pump-probe delay. For both 40 (blue) and 80 (purple) kV/cm a reduction in the signal and clear oscillations are observed. The oscillatory part of the signal shown in panel a2 was obtained by subtraction of a frequency independent background displayed as the blue dashed line in panel a1. Fourier transform of the extracted oscillations, show a peak at 1 THz (at 5K – red line) and 0.75 THz (at 30 K – lack line). Note that 1 THz and 0.75 THz represents twice the equilibrium plasma frequency measured at a temperature of 5K and 30K in this material, *i.e.* $\omega_{p0} = 0.5\ THz$ and 0.37 THz. Also, the measurements at different temperatures indicate a red shift of these oscillations, with their frequency always twice the static plasma frequency, as the equilibrium frequency also red-shifts with temperature.

Further, the simulated spectrally integrated response replicating the measured pump-probe response is displayed in panels b.1 and b.2. A very good agreement found with the experimental data. A comparison of the oscillation frequency between experiment and theory is made in panel c, both returning a value close to $2\omega_{p0}$, as expected.

The time dependence of the sine-Gordon equation with oscillator strength modulated at twice its plasma frequency (as given by equations 17 and 18) resembles the Matthieu equation for parametric amplification,

$$i.e.\ \frac{\partial \emptyset}{\partial t^2} + \omega_p^2 \varepsilon_r \emptyset \left(1 - \frac{\emptyset_0^2}{4} - \frac{\emptyset_0^2 \cos(2\omega_{p0}t)}{4} \right) = 0.$$

Hence, for intense enough pump fields, parametric amplification of the JPWs is expected, with the mechanism being indeed reminiscent of the third order nonlinearity in optical parametric amplifiers.
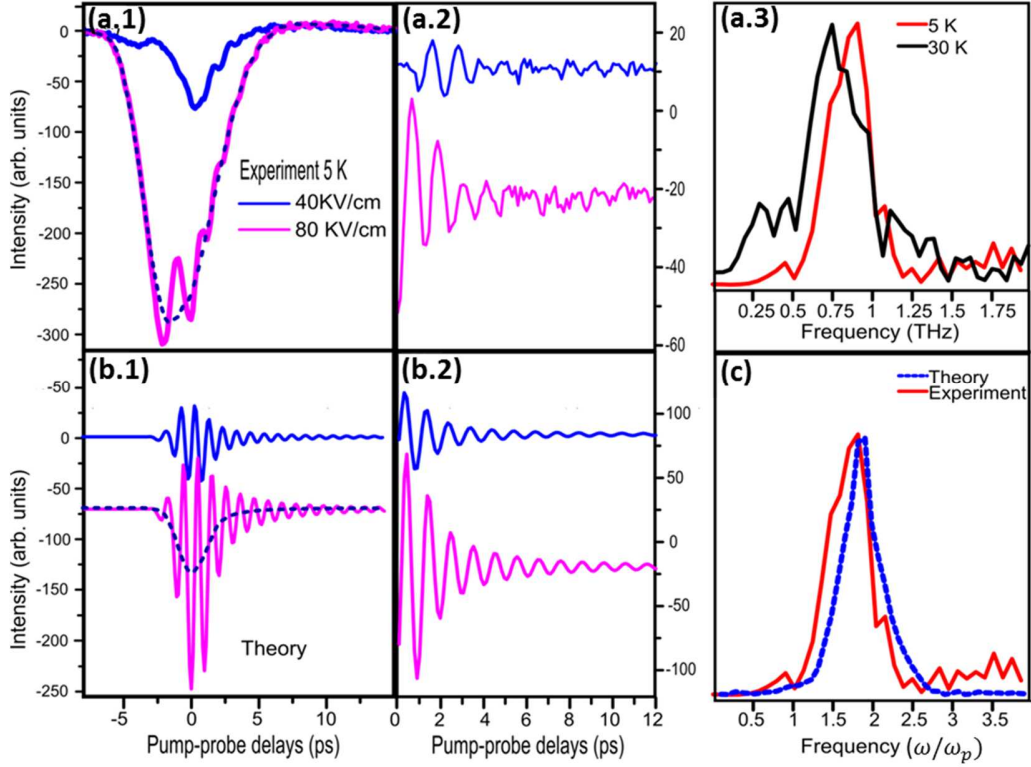
Figure 3.11: Frequency-integrated THz probe pulse as a function of pump-probe delay.
a.1 Measured experimental data for two fluences, the blue dotted line indicates the subtracted background to obtain the oscillatory component. **a.2** the extracted oscillations, after applying a high pass Fourier filter (0.2 THz). **a.3** Fourier transforms of the extracted oscillations show a peak at 1 THz (at 5K) and 0.75 THz (at 30 K). **b.1** and **b.2** are the corresponding simulated data. **c** A comparison of the oscillation frequency between experiment and theory.

This is manifest in the time- and frequency-dependent loss function as measured by the THz probe pulse, as displayed in Figure 3.12 for a pump field of ~ 80 kV/cm. The loss function redshifts upon excitation and also becomes successively negative and positive as a function of pump probe delay. This corresponds respectively to amplification and dissipation of the Josephson plasma waves excited by the THz probe pulse, and occurs at ~ 1THz (*i.e.* equivalent of ~ $2\omega_{p0}$).

The simulated loss functions are shown in Figure 3.12 b. Good agreement is observed between the simulated and experimentally obtained loss functions. Furthermore, very good agreement in the pump field strengths is observed between the experiments

and the simulations, reiterating the validity of the model in describing the observed non-equilibrium effects.
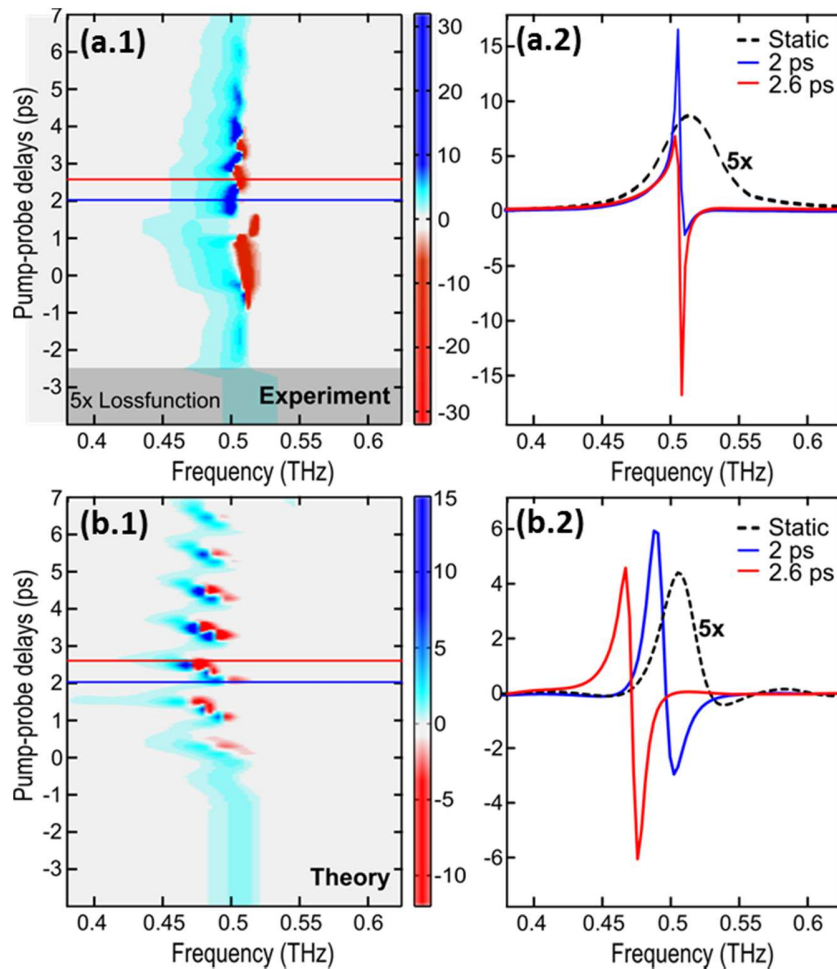
Figure 3.12: Time evolution of the frequency resolved loss function as a function of pump-probe delay. a.1 Experimental loss function as a function of pump-probe delays. Note that the loss functions at negative time delays have been multiplied by a factor of 5. **a.2** Line-cuts of the loss function at pump-probe delays of t = -4 (static), 1.5 and 2 ps. **b.1** and **b.2** are the corresponding loss functions obtained from simulations.

3.6. Conclusions

The work presented in this chapter reports on the nonlinear optics of Josephson junctions in a cuprate superconductor. The strong field terahertz pulses used as stimulation allow for non-dissipative excitation and control of the interlayer tunneling between the Cu-O planes. The experimental data were accurately reproduced by numerically solving the one-dimensional sine-Gordon equation.

In the first experiment performed on $La_{1.84}Sr_{0.16}CuO_4$, the frequency of *narrowband* THz pulses was tuned across the Josephson plasma resonance of the sample, to explore different excitation regimes. The strongest nonlinear effect was observed for resonant driving at the plasma frequency, where a slowly propagating soliton is emitted. This mode could be optically detected by a subsequent probe pulse, as it induces a transparency window caused by interference.

In the second study, $La_{1.905}Ba_{0.095}CuO_4$ was resonantly excited with *broadband* terahertz pulses. In this case, the Josephson plasma waves were driven to a regime in which phase fluctuations were parametrically amplified, exhibiting an oscillatory dependence at twice the frequency of the drive.

Due to the non-dissipative superconducting nature of the plasma waves, both experiments presented above show the potential of layered superconductors for applications in ultrafast electronics.

4

Competing phases in the La-214 cuprate family

It is known that in low-dimensional Fermi liquids, which are ordinary metals, weak electron-phonon and electron-electron interactions can lead to broken symmetry ground states. Among the most striking examples of this behavior are charge (CDWs) and spin density waves (SDWs). CDWs that occur in non-correlated Fermi liquids are a consequence of electron-phonon coupling and can be explained within the BCS theory.

However, charge order was also find to occur in strongly correlated systems, such as high temperature superconductors. In such systems, the mechanism behind the formation of charge order often eludes simple explanations and remains a subject of much debate in modern condensed matter physics. Moreover, the interplay between charge order and superconductivity is of particular interest, with studies supporting either the coexistence or the competition between these different degrees of freedom. Indeed, even early attempts to explain superconductivity were based on a sliding CDW resulting in infinite conductivity in the absence of defects [47]. Furthermore, it has been observed

that high-temperature superconductivity arises in proximity to density wave orders in many different systems including Fe-based and organic superconductors, chalcogenides, and, in particular, cuprates. Whether these orders are competing or working together is a question which still has to be answered in many of the materials mentioned before.

The experiments presented in chapter 5 concentrate on manipulating the c-axis coherent transport in cuprates with charge stripes; for our purpose, the basic understanding of a CDW is essential. Thus, in this chapter, the electronic properties of cuprates and their temperature-doping phase diagram will be presented, followed by a discussion on CDWs and the theories behind their mechanism.

4.1. Electronic properties of cuprates

As mentioned above, in materials where electron correlations become strong, the conventional band theory breaks and the measured properties can become vastly different from the single electron picture predictions. This was first experimentally proven by Boer and Verwey in the case of transition metal oxides [48]. These compounds have only partially filled $3d$ bands, so according to band theory should be metals; in fact, they turn out to be insulators, and this can only be explained by taking into account electron-electron interactions [49]. This is also the case for cuprates, for which most of the rich features in the temperature-doping phase diagram can be explained by accounting for Coulomb interactions.

In the parent compound of cuprates, *i.e.* at zero doping, all the Cu^{2+} ions in the CuO_2 planes are in the $3d^9$ configuration. Due to the orthorhombic crystal field, the energy levels of the Cu^{2+} and O^{2-} ions are modified.
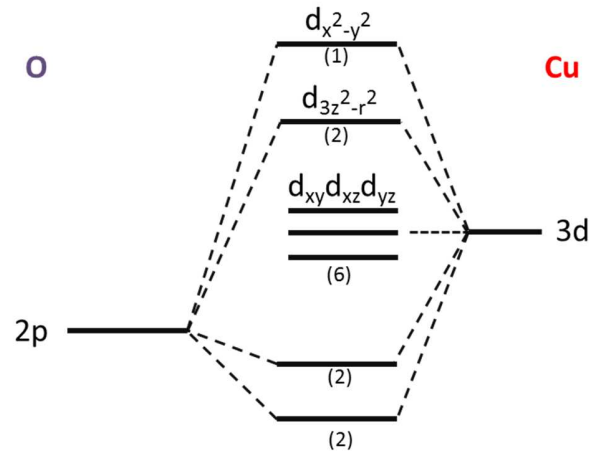
Figure 4.1: Hybridization between the Cu 3d and the O 2p electronic level in cuprates.

The crystal field removes the five-fold d-orbital degeneracy in a way that depends on the details of the Cu-ion environment. However, in all cuprates, the square Cu-O lattice makes the $d_{x^2-y^2}$ orbital the less energetically favorable since in that case most of the electron density is allocated in the direction of the negatively-charged O^{2-} ions. At zero doping, as all the d levels are filled with 9 electrons, the $d_{x^2-y^2}$ level is half filled. The O^{2-} ions are in the $2p^6$ configuration, which is split in three completely filled levels ($\pi_\perp$, $\pi_\parallel$, σ) by the crystal field. We now consider the hybridization between the Cu and O levels (Figure 4.1). The comparison of the final Cu $d_{x^2-y^2}$ energy with the O σ energy suggests that the bonding level has a predominant oxygen character, while the antibonding level has a predominant copper character. Since the latter is half filled, according to band theory, this should lead to a Cu-like conduction band, thus a conductive behavior. However, the experimental evidence on the undoped parent compound, La_2CuO_4, shows them to be antiferromagnetic (AF) insulators with a rather high Néel temperature, $T_N \simeq 300$ K. The reason for this discrepancy can be found in electron correlations, as described below.

The simplest model for electron correlation was first proposed by Hubbard in 1963 [50]. This model introduces a term that corresponds to the Coulomb repulsion U when two electrons occupy the same lattice site, hence removing the two-fold spin degeneracy and creating two states separated by the energy U. In a solid, the two states

become two energy bands called the Lower Hubbard Band (LHB) and the Upper Hubbard Band (UHB).

A schematic application of the Hubbard model to the transition metal oxides was developed by Zaanen, Sawatsky and Allen [51] in which three electronic bands are considered: the Cu 3d, split in the UHB and LHB, and the O 2p (Figure 4.2). At half filling, the LHB and the O 2p bands are occupied, allowing two kind of charge excitations:

- a charge fluctuation between the two Cu bands, which creates a doubly-occupied Cu site, associated to the energy U; This happens for **U < Δ** and gives rise to the so-called **Mott-Hubbard insulators**.

- a charge transfer excitation from the O 2p band to the UHB, associated to the energy Δ; This arises when **Δ < U** and the compounds are called **Charge Transfer insulators**.

In copper oxides, the Coulomb repulsion between two electrons occupying the same Cu orbital is of the order of U ~ 10eV, suppressing the charge fluctuations within the Cu-3d^9 orbitals. The lowest excitation remains the charge transfer of a localized Cu-3$d_{x^2-y^2}$ hole into its neighboring O-2p orbitals, with an energy cost of Δ ~ 2eV. Thus, the experimental results indicate that the cuprates are charge transfer insulators, since Δ < U **[51], [52]**.

One of the main consequences of the strong correlations in cuprates is that usually independent energy scales become intertwined, with low-energy phenomena strongly affecting the electronic properties at the energies of several eV. This stays at the core of the rich phase diagrams that these materials exhibit, including the existence of superconductivity, and the formation of charge and spin density waves.
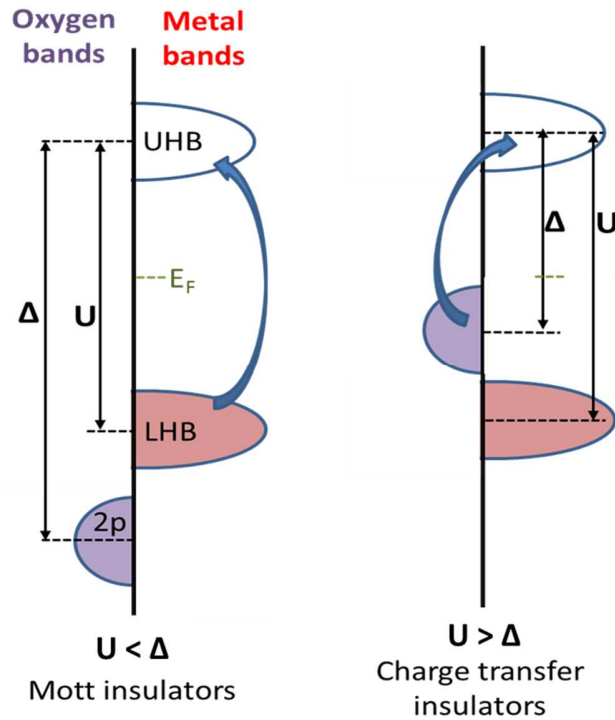
Figure 4.2: Band diagram of a transition metal oxide. The *d*-orbital of the transition metal is split in LHB and UHB. The *p*-orbital of oxygen is filled. (a) If U < Δ, the compound is a Mott insulator. (b) If U > Δ, the transfer of charge occurs from 2p oxygen site to UHB of neighboring transition metal. The compound is a charge transfer insulator

4.2. Phase diagram

Cuprate materials undergo radical modification when a moderate density of charge carriers is introduced into the system. This leads to complex doping-temperature phase diagrams which have been extensively studied in the last three decades by a wide variety of techniques. In Figure 4.3 a generic phase diagram of hole-doped high-T_C cuprates is shown (adapted from [7]). The salient features of the phase diagram are:

- Parent compound properties –
  - A long range antiferromagnetic ordering is found in the undoped parent compound, which persists for low doping levels (x < 0.05 holes

/ Cu atom). Above this level, a spin-glass state with short-range magnetic order is formed.

- Superconducting dome –
  - o Superconductivity appears at low doping, with T_C increasing with doping (underdoped region), then reaching a maximum value (optimal doping, $x \approx 0.16$), but being suppressed with further increasing the doping level (overdoped regime). This results in a dome-shaped dependence on doping [53].

- Pseudogap –
  - o The normal state for temperatures above the critical temperature (T > T_C) and $x < 0.16$ is strikingly different from a conventional metal, exhibiting high levels of resistivity and a depletion in the density of states around the Fermi energy. This region is usually referred to as the *pseudogap region*. The existence of the pseudogap was revealed by a plethora of experiments: resistivity technique [54], IR spectroscopy [55], [56], angle-resolved photoemission spectroscopy (ARPES) [57], [58], etc. With increasing x, the system moves towards the normal Fermi-liquid state (the overdoped side of the phase diagram).

- The 1/8th anomaly and stripe ordering –
  - o The superconducting dome of the La-214 cuprate family exhibits an anomalous dip near $x = 1/8$ doping. In the barium based compound, LBCO, the bulk superconductivity is completely destroyed at this doping.
  - o The suppression of superconductivity is accompanied by the formation of charge stripes (*i.e.* the charges introduced by doping into the antiferromagnetic lattice align parallel). The onset of charge stripe order (CO) is accompanied by spin order below T_{SO} [59]. In other families of cuprates, like YBCO, a similar apparent suppression of superconductivity near $p = 1/8$ occurs, with recent experiments unveiling stripe ordering (SO). In this case spin excitations appear to

be gapped out, with gapping an order of magnitude larger than in lanthanides [60].

○ The Sr (Ba) substitution for La in LSCO (LBCO) induces also a structural phase transition driven by soft phonons from the high-temperature tetragonal (HTT) to low-temperature orthorhombic (LTO) phase, below ~ 240K. In LBCO, on further cooling, the LTO configuration evolves into the low temperature tetragonal phase, LTT. This occurs below the T_{LT} temperature. This later configuration has been shown to stabilize the charge order phase [61], [62].
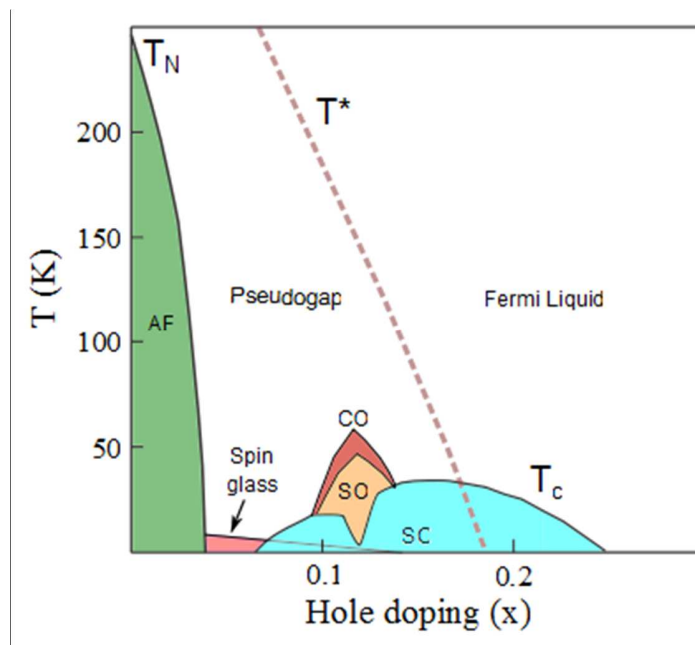
Figure 4.3: Generic phase diagram of La-214 as a function of temperature and hole doping concentration, adapted from **[63]**. T_N, T^*, T_C indicate the Neel, pseudogap and superconducting temperatures, respectively. AF, SC, SO and CO stand for antiferromagnetic, superconducting, spin-order and charge-order phases.

In the CO_2 planes of a cuprate, signature of preformed pairs was shown to occur at high temperatures. However, for cuprates to become superconducting, coherence has to establish between the various layers, *i.e.* superconducting tunneling along c-axis has to arise. The magnitude of the normal state c-axis resistivity, ρ_c, is orders of magnitude larger of that expected from band calculations, leading to considerable resistivity

anisotropy. Also, the temperature dependence of ρ_c is in most cases typical of a semiconductor or insulator, while the in-plane resistivity, ρ_{ab}, exhibits a metallic behavior. The c-axis transport in the normal state of the cuprates is dictated by the tunneling of incoherent carriers. However, as extensively discussed in previous chapters, in the superconducting state tunneling relies on Cooper pairs which obey the Josephson equations; this further leads to a Josephson plasma resonance in the superconducting state. These peculiar c-axis transport properties of high-T_C cuprates are the manifestation of the unusual electronic states of these materials discussed above [64], [65].

4.3. Charge Density Waves

Strong electron-electron and electron-phonon interactions can result in a ordering of the electron density in a solid. In a simple picture, charge density waves (CDW) are a modulation of the conduction electron density throughout the crystal, accompanied by a periodic lattice distortion, and occur predominantly in low-dimensional materials. The existence of CDW was first predicted by Peierls in the 1930s, who observed that a one-dimensional chain of equally-spaced atoms is not stable at low temperatures [66]. The assertion was that, in these conditions, the elastic energy cost to modulate the atomic positions is less than the gain in conduction electron energy, thus favoring CDW as a ground state. At high temperatures, however, the electronic energy gain is reduced by thermal fluctuations, so the metallic state is stable. A consequence of the Peierls model is the transition of the material from the metallic high-temperature state to the insulating ground state at a critical temperature (also known as Peierls transition). The electron-phonon coupling responsible for the formation of CDWs seems to be particularly favorable when the phonon modes soften, such as in the case of Kohn anomaly [67].

However, this simple picture regarding the origin of CDWs does not seem to be correct in many materials. Density functional theory calculations performed for a one-dimensional chain of Na atoms (which approximates a perfect Peierls system) showed no sign of a purely electronic density wave, and relaxation of the ion positions in the 1D chain failed to produce any distortion [68]. However, when the dimensionality of the system was increased (*i.e.* the atoms were allowed to move in two dimensions), the lowest energy state was a zig-zag chain, but the electronic gap anticipated by the Peierls

CDW phase was missing. Similar computational attempts to stabilize a CDW without allowing the ions to move have failed also for $NbSe_2$, which is a prototypical quasi-two dimensional CDW metal.

The failure of the Peierls picture comes from considering the lattice distortion a secondary effect that comes as a result of the charge redistribution which would occur regardless of whether or not the ions subsequently shift from their initial positions. This is not valid in real materials, where the electronic and ionic instabilities always occur simultaneously.

A large number of materials undergo a transition to a CDW state, especially in low-dimensional systems. Classical materials that exhibit the CDW phase are $NbSe_3$ and $K_{0.3}MoO_3$, with CDW emerging below T = 145 K and T = 180 K respectively. Moreover, CDW transport was observed also above room temperature, in materials like NbS_3, T = 340K.

Early discussions on CDWs were developed in the attempt to explain superconductivity. H. Frohlich (1954) predicted the formation of collective charge transport and in particular of CDWs in his theory explaining 'one-dimensional superconductivity' [47].

The interplay between CDW and superconductivity has led to much debate also in the field of high-T_C superconductivity [69], [70]. One point of view is that the CDW represents a state that competes with superconductivity. An alternate point of view is that the formation of stripes is a part of the mechanism of superconductivity itself [71].

4.4. CDW and the superconducting order in the La-214 family

Many materials that host superconductivity exhibit various forms of charge and spin ordering, such as the BCS superconductor $2H$-$NbSe_2$ [72], [73], cuprates [74]–[76], and even certain organic compounds [77].

Among the cuprate materials, a typical example is the La-214 family. In the case of both LSCO and LBCO, the superconducting dome exhibits an anomaly in the form of a dip (far more pronounced in LBCO, where there is a complete suppression of superconductivity) at x = 1/8 which is attributed to spin and charge stripe fluctuations [78], [79]. In this states, the charges introduced by doping into the antiferromagnetic

lattice align parallel to form equidistant charge and spin stripes [80] which arise from a balance between phase separation (the AFM insulator expelling the doped holes) and long-range Coulomb repulsion. The stripes have been shown to be either statically ordered (in LBCO) [79], [81] or slowly fluctuating (in LSCO) [82] and are pinned down by a low-temperature tetragonal structure. Moreover, due to the subtle interplay between Coulomb repulsion and phase separation, in LBCO the uniaxial stripes alternate in alignment along the a and b crystalline axes in neighboring planes, with a stripe periodicity that locks with every fourth unit cell hence suppressing c-axis superconductivity.

A recent experiment using the grating spectroscopy technique to generate collective modes (amplitudon and phason) of the CDW state in LSCO thin films supports that the fluctuating CDW state most probably competes with superconductivity [82].

CDW materials provide an ideal playground for time-resolved studies, where the excitation of the CDW modes or collapse of the CDW gap lead to an understanding of the collective behavior of the system [83], [84]. By using intense laser pulses at mid-infrared and terahertz frequencies tuned resonantly to some specific vibrational mode of the crystal lattice, superconducting coherence was transiently enhanced (or induced), possibly by melting some competing phase (*e.g.* stripe order or charge density waves) [85]–[87].

The first vibrational control experiment on high-T_C cuprates was performed on $La_{1.675}Eu_{0.2}Sr_{0.125}CuO_4$ [85]. Similar to LBCO, this material also exhibits an LTT phase for $T < T_{LT} = 135$ K and stripe order for $T < T_{SO} = 25$ K. In this experiment the crystal lattice was dynamically perturbed by selectively driving the IR active, in-plane Cu-O stretching mode with femtosecond pulses centered around ~20 THz frequency. The transient state was shown to be superconducting by detecting a Josephson Plasma Resonance edge at ~ 2 THz, with the effect persisting up to 10-20 K, near the spin order transition temperature. The hypothesis for the light-induced interlayer Josephson coupling was an instantaneous melting of the stripe order, which was further confirmed by a subsequent experiment. Thus, the evolution of the stripe order and the LTT distortion was investigated by femtosecond resonant soft X-ray diffraction in the related compound $La_{1.875}Ba_{0.125}CuO_4$ after ~ 20 THz phonon

excitation [86]. Stripe order was found to melt promptly on the same sub-ps time scale of light-induced superconductivity in LESCO, underlying the close connection between the two phenomena. In contrast, the LTT distortion was only weakly reduced and on a much longer time scale ($\sim$ 15 ps), suggesting that it plays only a minor role (if at all) in the onset of three-dimensional superconductivity.

As concluded in the previous experiment, lattice distortion seems not to play an important role in relation to c-axis superconductivity. Thus, the work presented in the next chapter will focus on other optical excitation schemes (*i.e.* as opposed to lattice excitation), in order to melt stripes and enhance the superconducting interlayer coupling.

5

Optical enhancement of superconducting interlayer coupling in LBCO

As presented above, the presence of charge and spin stripe order in several families of high-T_C cuprates (which includes LBCO) and its interplay with superconductivity is still not completely understood, despite the plethora of experimental effort on the matter. It has been shown that spin and charge stripes are compatible with in-plane superconducting pairing, but, due to their orthogonal arrangement in adjacent planes (see Figure 5.1), can compete with interlayer superconducting phase coherence.

In the present chapter, enhancement of the Josephson interlayer coupling in LBCO is demonstrated through the suppression of charge order. The results further support the competing nature between the stripe order and SC order. The melting of the stripe phase is achieved by the use of femtosecond laser pulses with high photon energy

(800-nm wavelength), thus performing a purely electronic excitation in LBCO crystals, with light polarized perpendicular to the CuO_2 planes (*i.e.* along the *c* axis).

In the past, above-gap charge excitation at near-infrared and visible wavelengths has been extensively studied in conventional and high-temperature superconductors. In high-T_C cuprates, ultrafast studies with probing frequencies in the near- and mid-infrared allowed to identify different time scales in the response dynamics during the recovery of the superconducting condensate and of the pseudogap correlations [88], [89]. Optical pump-terahertz probe studies provided additional information by monitoring the dynamics of excess quasiparticles and the condensate recovery in the energy scale of the superconducting gap [35]. These experiments directly demonstrated how Cooper pairs are broken right after photo-excitation and how they recombine at later times, by directly following the evolution of superfluid density.

All these high-energy charge excitation experiments on high-T_C cuprates have been performed by pumping the system with light pulses polarized parallel to the CuO_2 planes (*ab* direction), thus exciting the Cooper-pair condensate above the superconducting gap. Furthermore, the pump fluences used therein were usually in the ~ 10 $\mu J/cm^2$ range and below, just enough to destroy the condensate and to study its recovery dynamics.

Here, we set out to excite "striped" high-T_C cuprates of the LBCO family with much stronger laser fields (fluences up to ~3 mJ/cm^2) polarized perpendicular to the planes, *aiming at directly melting the stripe order and enhancing superconducting interlayer coherence. The detailed study also includes the dependence of this effect on the pump wavelength, which is tuned between the mid-infrared (5 µm) and the visible (400 nm) with the aim of understanding how stripe order is melted most effectively (Figure 5.1 a), and to determine a dominant energy scale that affects the nonlinear time-dependent interplay with superconductivity. We complement the THz time domain spectroscopy studies with soft X-ray measurements which show a prompt decrease in the stripe peak upon optical excitation (Figure 5.1b).*
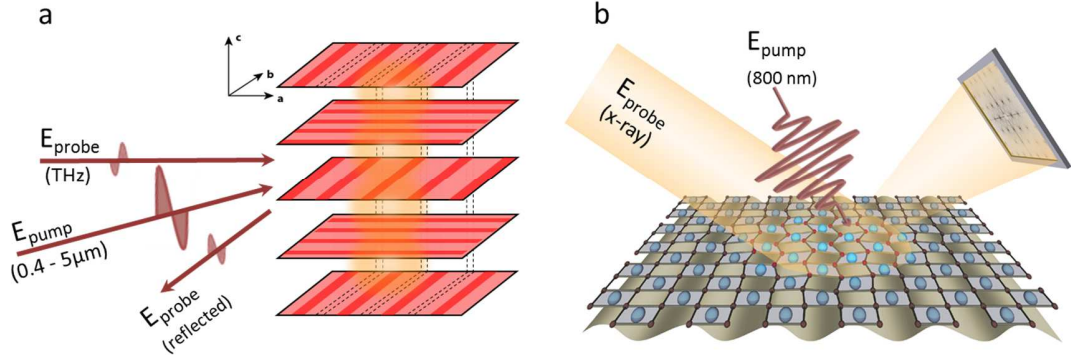
Figure 5.1: Schematics of the pump-probe set up used for THz time domain spectroscopy measurements (a) and of the 800nm pump - soft x-ray probe experiment (b). The orthogonal arrangement of charge stripes is visible in panel (a).

5.1.   Light induced superconductivity by NIR excitation

Samples

The $La_{2-x}Ba_xCuO_4$ single crystals investigated in the present study were grown [90] using the traveling-solvent floating-zone method for a series of three nominal Ba concentrations $x = 9.5\%$, 11.5%, and 12.5%, thus covering the most underdoped region of the phase diagram in Figure 5.2 (a).

The $x = 9.5\%$ and 11.5% samples are superconducting with transitions at $T_C \simeq 32$ and 13 K, respectively, while superconductivity in the $x = 12.5\%$ sample is strongly suppressed with $T_C \lesssim 2.4$ K. This value is below the lowest temperature achievable in our experiments, which is T = 4K. For the three samples used in the current work, all values of T_C were determined by magnetic susceptibility measurements [90], [91].

At 9.5% doping, the appearance of superconductivity, charge- and spin-order, as well as the structural transition, are reported to occur at the same temperature:

- $x = 9.5\%$: $T_{CO} \simeq T_{SO} \simeq T_{LT} \simeq T_C \simeq 32$ K.

As one increases the holes concentration, these transitions decouple, occurring within a 15 K temperature window:

- $x = 11.5\%$: $T_{CO} \simeq T_{LT} \simeq 53$ K and $T_{SO} \simeq 41$ K,
- $x = 12.5\%$: $T_{CO} \simeq T_{LT} \simeq 55$ K and $T_{SO} \simeq 42$ K.

All three crystals were cut and polished along the *ac* direction. The resulting *ac* surfaces measured between 5 and 15 mm^2 and were large enough for performing long-wavelength time-domain spectroscopy in the sub-THz regime.

Experimental implementation

The time-domain THz spectroscopy measurements presented in this thesis were performed in reflection geometry. A detailed description and a sketch of the pump-probe setup is presented in Appendix A.1. Single-cycle THz pulses were generated by illuminating a large-area photoconductive antenna with near-infrared laser pulses from a Ti:Sa amplifier. After generation, the optical pulses with frequency bandwidth covering a range between 150 GHz and 3 THz, were focused on a ~ 1 mm spot diameter onto the sample surface, at 30° incidence. The polarization of the THz light was kept perpendicular to the CuO$_2$ planes (*c* direction). The reflected electric field was measured by electro-optic sampling in a 1 mm thick ZnTe (see Appendix A.2). The equilibrium optical properties were obtained by comparing the THz reflected field measured at equilibrium with our setup at different temperatures against the *c*-axis broadband reflectivity reported in Ref [91].

The *transient optical properties* were obtained as a function of pump-probe delay by measuring the pump-induced change in the reflected THz electric field. The transient response was processed by taking into account the mismatch between the penetration depth of the pump pulses (~ 0.1 - 10 µm, depending on the excitation wavelength) and the THz probe pulses (~ 50 - 500 µm), assuming a thin photo-excited layer on top of an unperturbed bulk (*i.e.* which retains the optical properties of the sample at equilibrium). Figure 5.2, (b) shows the absorption coefficients corresponding to the different pump wavelengths used in this experiment, revealing a factor of 100 difference between the absorbance at the lowest (400 nm) and highest (5000 nm) pump wavelength. The effect of this difference and how was it accounted for in the data analysis will be discussed in detail while presenting the pump-wavelength dependent transient data.

A detailed analysis of the transient response upon optical excitation was performed at different temperatures, both bellow and above T_C (see circles on phase

diagram in Figure 5.2 a), and different pump wavelengths and fluences, for all three doping levels mentioned above.

Equilibrium optical properties

The *c*-axis equilibrium reflectivity of all three samples at the lowest measured temperature ($T = 5$ K) is shown in the shaded region of Figure 5.2 c).

- At *x* = **9.5%** doping (blue line), the superconducting transition is evidenced by the appearance of a clear Josephson Plasma Resonance at ~ 500 GHz;

- For *x* = **11.5%** (red line), the response is very similar to the $x = 9.5\%$ sample, with a JPR emerging in the reflectivity spectrum slightly below ~ 200 GHz;

- At *x* = **12.5%** doping (green line), no JPR feature is visible down to the lowest measured frequency (~150 GHz), the reflectivity remaining flat. We stress again that for this compound we are above the critical temperature, $T_C < 4$ K **[92]**.

In the spectrum of the real part of the conductivity no feature is present at low frequencies, independent of the doping level. The arrows indicate the different pump photon energies that will be used in these measurements. One can clearly see that, along the c-axis, the optical conductivity shows a strong absorption in the 3 eV region (400 nm wavelength), while around 1.5 eV (800 nm) only a tale of a higher frequency band is found. Below 0.6 eV (5 μm) the optical conductivity stays gapped. The fact that linear absorption increases with photon energy has to be accounted for in the pump-wavelength dependent study.
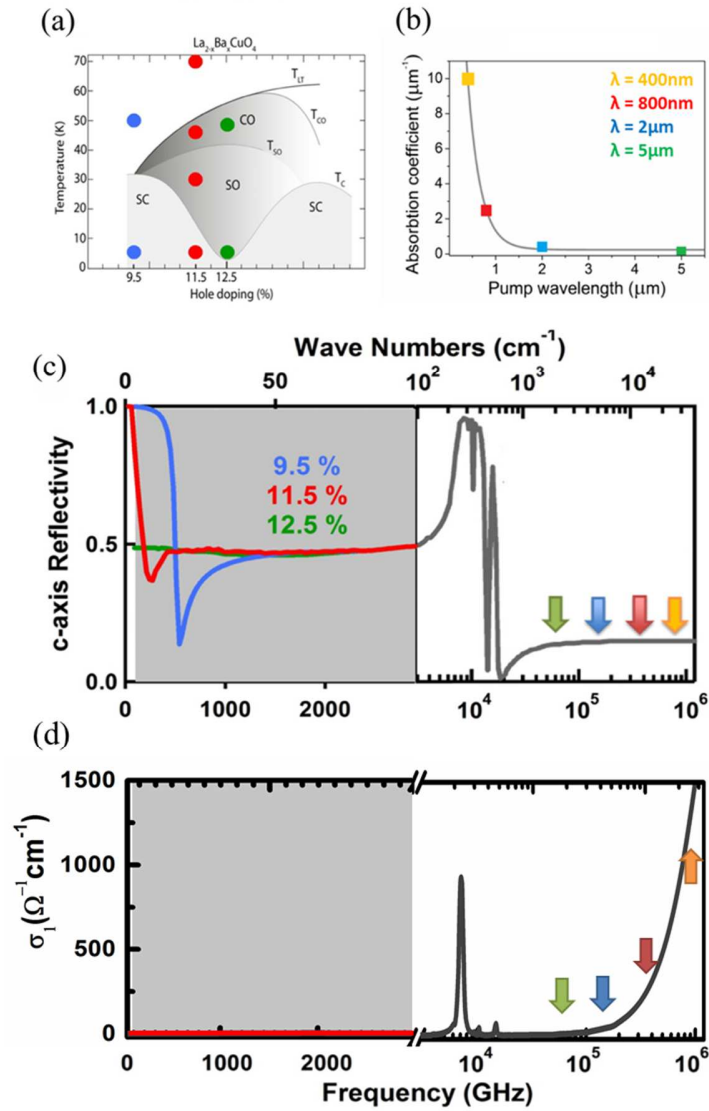
Figure 5.2: (**a**) Phase diagram of $La_{2-x}Ba_xCuO_4$ as a function of temperature and hole doping concentration (discussed in detailed in Chapter 4). Colored circles indicate the different doping levels and temperatures at which the pump-probe experiment of the present work has been carried out. (**b**) Absorbtion coefficient of the optical pump pulse as a function of the pump wavelength. (**c**) and (**d**) Equilibrium c-axis optical properties of LBCO. The gray-shaded region is the one investigated in the present experiment, while the high-frequency c-axis data for which the doping dependence is negligible are taken from Ref [**91**] The THz reflectivity at $T = 5$ K is depicted in blue (9.5% doping), red (11.5%) and green (12.5%). The arrows indicate the region of the optical excitation performed in this experiment and the color code coincides with the one of panel (**b**).

Out of equilibrium transient optical properties

Although the pump excitation wavelength was varied, I first discuss the observed effects when the LBCO crystals were photo-excited with ~100 fs laser pulses with 800 nm central wavelength, polarized along the c axis. While in the in-plane direction this region around 1.5 eV shows a strong absorption (the so-called charge transfer resonance) [93], along the c axis only the tail of a higher frequency band in the optical conductivity is found. Thus, in this case, the effects of excitation of incoherent, hot quasi-particles should be reduced with respect to in-plane pump experiments.

By measuring the pump-induced changes in the amplitude and phase of the reflected electric field polarized perpendicular to the planes, the behavior of all complex c-axis optical functions could be retrieved as a function of pump-probe delay. As mentioned before, by calculating the coupled Fresnel equations of a multi-layer system which takes into account the penetration mismatch between pump and probe, the transient optical response of the photo-excited layer could be derived.

In Figure 5.3, the reflectivity $R(\omega)$ of the photo-excited LBCO sample is shown for all measured doping levels and temperatures at +1.5 ps pump-probe delay, and compared with the same quantity at equilibrium. Some salient features include:

- At the lowest doping, $x = 9.5\%$, for temperatures below the superconducting transition temperature, $T < T_c$, a slight blue-shift of the JPR (about 3%) is observed (panel a.1), suggestive of a photo-induced increase in the interlayer Josephson coupling. For the same material *above T_c* (panel a.2), no considerable photo-induced dynamics could be measured at any pump-probe delay.

- In the sample for which $x = 11.5\%$, the effect is much more pronounced: *below T_c* (panel b.1) a substantial blue-shift of the JPR (from ~200 to 600 GHz) is observed upon photo-stimulation. *Above T_c*, in the spin-ordered phase (panel b.2) an edge-like feature is photo-induced in the flat, featureless normal-state $R(\omega)$. The induced feature appears at ~500 GHz and strongly resembles the JPR detected below T_c.
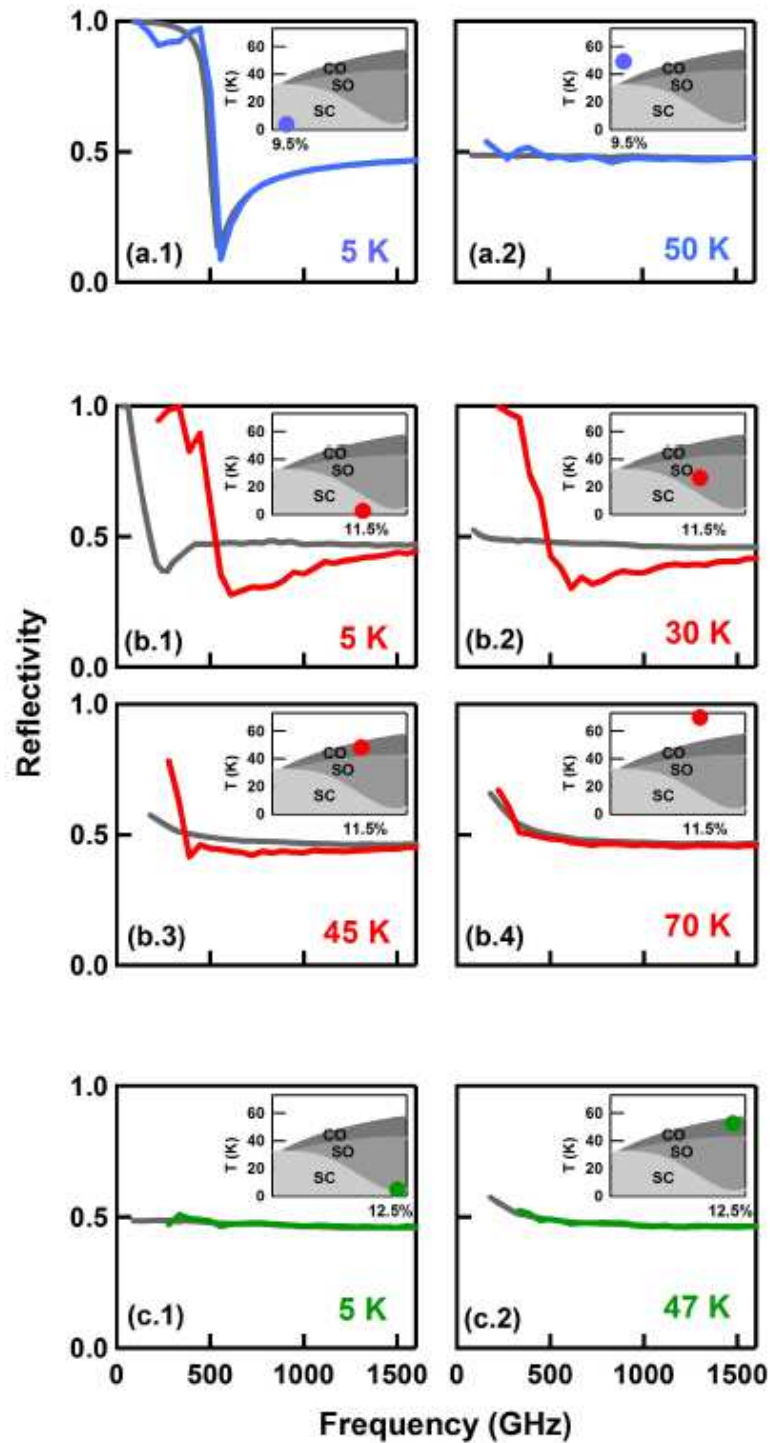
Figure 5.3: Reflectivity of the photo-excited LBCO samples. THz reflectivity of La$_{2-x}$Ba$_x$CuO$_4$ displayed at different doping values and temperatures at equilibrium (grey) and 1.5 ps after near-infrared excitation (colored). Data in panels **a, b** and **c** correspond to doping levels of 9.5%, 11.5% and 12.5% respectively. Data in panels **a** and **b** have been acquired with a pump fluence of ~2 mJ/cm^2, while those in panel c with ~3 mJ/cm^2. In the insets, the parameters at which the measurements are taken are indicated in the LBCO phase with colored circles.

By increasing the temperature further to T = 45 K (panel b.3), *above T_{SO}*, one finds a similar effect: a reflectivity edge at ~300 GHz can be clearly distinguished in the reflectivity spectrum of the transient state.

The temperature was increased even higher, *above T_{CO}* (panel b.4), with no evidence of a JPR-like feature in the reflectivity of the perturbed material.

- Finally, in the 1/8-doped material, **$x = 12.5\%$**, no measurable effect was observed at any temperature and pump-probe delay (panels c.1 and c.2). As will be discussed further, even when increasing the near-infrared beam fluence to 3 mJ/cm^2, the transient reflectivity remained featureless.

Inducing a JPR-like feature in the reflectivity of the x = 11.5% sample above T_C together with the complete absence of any pumped induces response in the x = 12.5% sample were highly surprising, so further investigation was carried out in order to have a quantitative comparison between the pump-induced effects in the three samples, at different temperatures.

It is illustrative to characterize the transient response with the following quantity: $\Delta E_R/E_R$, that tracks the normalized transient changes in reflectivity at the maximum amplitude of the THz response. Figure 5.4 (a) depicts three such curves, taken after excitation of La$_{1.885}$Ba$_{0.115}$CuO$_4$ sample at T = 5K, for three different pump fluences. A clear trend emerges: the changes in reflectivity increase with increasing pump fluence. In panels (b) and (c), the peak of the optical response (at time delay t^{peak,} *i.e.* at the peak of the curves in panel a) of La$_{2-x}$Ba$_x$CuO$_4$ is plotted at various temperatures, as a function of pump fluence (which was tuned between 0.01 mJ/cm^2 and a maximum of 3 mJ/cm^2):

- For the **x = 11.5%** sample (panel b), the effect saturates with pump fluence, exhibiting a threshold behavior for temperatures below the spin order temperature, *i.e.* at 5K and 30K. The effect decreases with increasing temperature, and almost no changes in reflectivity are detected for T > T_{CO} (T = 70K).

- For **x = 9.5%** (panel c), a smaller but similar effect exists below T_C (dark blue squares), while above T_C (light blue) only a residual change in reflectivity can be detected.

- Finally, the **x = 12.5%** doped material (green squares in panel c) shows no change in the optical reflectivity, up to the highest pump-fluence measured. The absence of the effect seems to also be independent of temperature. This experimental evidence suggests that the 1/8-doped material, where the charge order parameter and correlation length are stronger and superconductivity is quenched, has a much lower photo-susceptibility than the other samples.
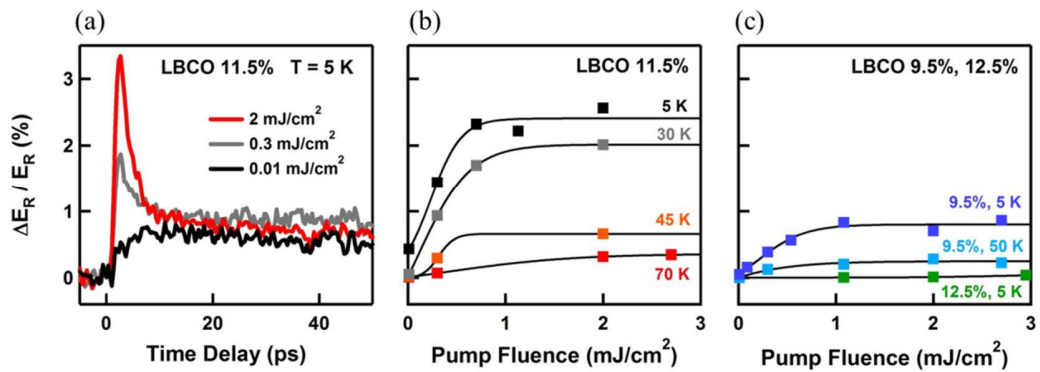
Figure 5.4: Fluence dependence of the pump-induced response in LBCO. (**a**) One dimensional traces of $\Delta E_R/E_R$ as a function of time delay, at three different fluences. The fluence dependence of the peak of reflectivity changes in the samples was measured at different temperatures, 1.5 ps after photo-excitation and is shown in panels (**b**) (x = 11.5%) and (**c**) (x = 9.5% and x = 12.5%). The lines in panels (**b**) and (**c**) are guides to the eye.

As clearly shown so far, the most striking effects induced by light in the optical response of LBCO appear in the stripe phase of the $x = 11.5\%$ sample. Thus, I will focus the analysis to this specific material, by exploring the behavior of the relevant complex optical constants as a function of temperature, pump-probe delay, pump fluence and pump wavelength.

In Figure 5.5 (lower panels), the real and imaginary part of conductivity, $\sigma_1(\omega)+i\sigma_2(\omega)$, and the energy loss function $\left[-\text{Im}(1/\tilde{\varepsilon})\right]$ of $La_{1.885}Ba_{0.115}CuO_4$ are displayed in color scale throughout the whole dynamics after photo-excitation, for **T < T_C**. Selected lineouts are shown in the upper panels at three pump-probe delays: t < 0 (equilibrium - gray), t = 1.5 ps (corresponding to the reflectivities in Figure 5.3 b.1 - red), and t = 5 ps (after the first relaxation process has occurred - blue).

Figure 5.5: Below T_C dynamics of the LBCO 11.5% system upon optical excitation. Lower panels: Frequency dependent optical conductivity, both real [$\sigma_1(\omega)$] and imaginary part [$\sigma_2(\omega)$], and energy loss function $\left[-\text{Im}(\mathbf{1/\tilde{\varepsilon}})\right]$ of LBCO 11.5% as a function of pump-probe delay. **Upper panels**: Selected lineouts of the optical properties are shown in the upper panels at three pump-probe delays: t < 0 (equilibrium - gray), t = 1.5 ps (red), and t = 5 ps (blue). All data have been taken using a pump fluence of 2 mJ/cm^2.

As expected, in the superconducting state *at equilibrium*, the out of plane superconducting nature is evidenced by a fully gapped $\sigma_1(\omega)$ (Figure 5.5 a.1, grey curve) and a 1/ω-like divergence in the low-frequency $\sigma_2(\omega)$ (panel b.1, grey curve). The quantity $\lim_{\omega \to 0} \omega\sigma_2(\omega)$ is an indication of the strength of the *c*-axis superfluid density. As already discussed, the Josephson-like tunneling, evidenced by an edge in the reflectivity, is expressed by a sharp peak in the loss function corresponding to the JPR frequency (c.1, grey curve).

The maximum pump induced effect is observed *1.5 ps* after photo-excitation (red curves), when a strong enhancement in $\sigma_2(\omega)$ is observed down to the lowest measured frequency, while $\sigma_1(\omega)$ stays gapped. In the outlines of the loss function, the same strong increase in the JPR frequency (~ 400 GHz) reported in the reflectivity analysis is apparent. *The observed electrodynamics is compatible with interlayer superconducting transport.*

At later delays, ~ 2.5 ps after excitation (see color plots), a well-defined absorption peak develops in the low-frequency $\sigma_1(\omega)$, while $\sigma_2(\omega)$ is peaked at finite $\omega \neq 0$. After t = 5 ps, a relaxation towards a state with a finite carrier scattering time is observed. Most importantly, the pump-probe dependence of the loss function (panel c.2) shows that there is a *continuous* evolution of the JPR frequency below T_C: it increases from its equilibrium value (~200 GHz) up to ~1200 GHz (at ~2.5 ps delay), and then relaxes back to lower values.

For a temperature higher than T_C, but lower than the spin order temperature (**T_C < T = 30K < T_{SO}**), where the system is non-superconducting at equilibrium, a similar qualitative pumped induced response is observed (Figure 5.6). Here, starting from the complex conductivity of an insulator ($\sigma_1(\omega) \simeq 0$ and $\lim_{\omega \to 0} \sigma_2(\omega) = 0$, grey curves in panels a.1-b.1), the material shows a strong light-induced enhancement in the low-frequency $\sigma_2(\omega)$, which turns positive and diverges down to the lowest measured ω. Concomitantly, $\sigma_1(\omega)$ is gapped, suggesting that in such transient state the charge carriers exhibit an anomalously coherent behavior, which resembles that of the Cooper pairs tunneling between the CuO_2 layers below T_C. In the case of the energy loss function, a peak is photo-induced on a flat and featureless background, it first blue-shifts, and then relaxes back to lower frequencies. As in the case of the below T_C data, the peak tends to progressively broaden with increasing pump-probe delay (see panels c1 and c2). For later delays, the evolution of all optical properties are indicative of a relaxation to a more incoherent state (t = 5 ps).

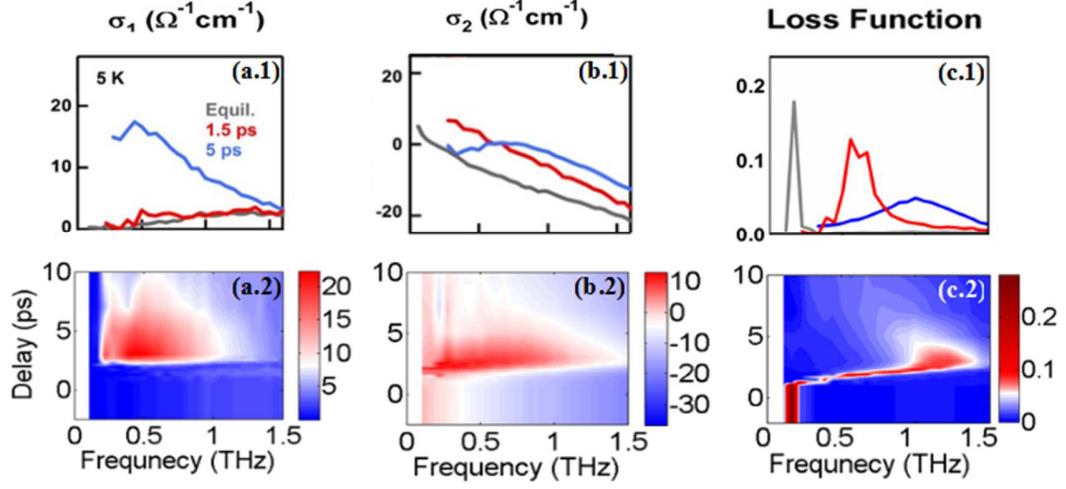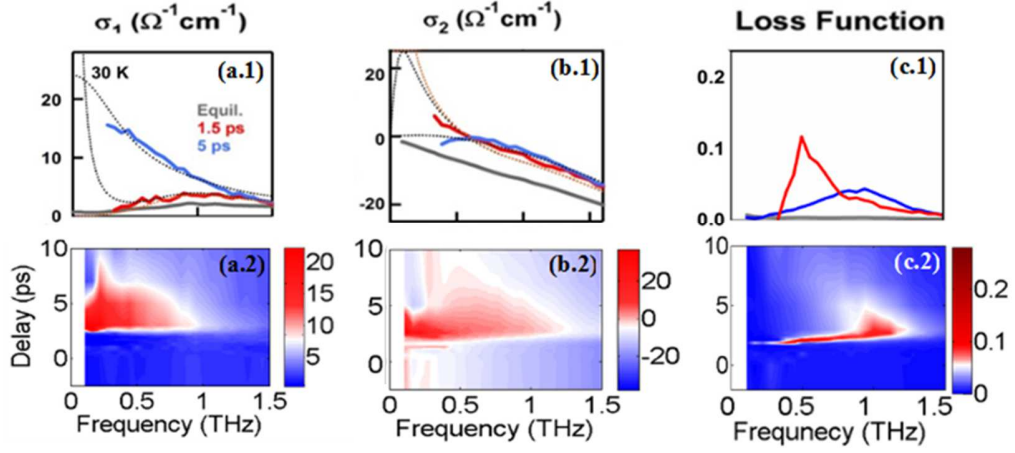**Figure 5.6: Above T_C ($T_C < T < T_{SO}$) dynamics of the LBCO 11.5% system upon optical excitation. Lower panels**: Frequency dependent optical conductivity, both real [$\sigma_1(\omega)$] and imaginary part [$\sigma_2(\omega)$], and energy loss function $\left[-\text{Im}(1/\tilde{\varepsilon})\right]$ of La$_{1.885}$Ba$_{0.115}$CuO$_4$ as a function of pump-probe delay. **Upper panels**: Selected lineouts of the optical properties are shown in the upper panels at three pump-probe delays: t < 0 (equilibrium - gray), t = 1.5 ps (red), and t = 5 ps (blue). All data have been taken using a pump fluence of 2 mJ/cm^2. In panels a.1 and b.1 examples of fits with a Drude model (dashed lines) and with a perfect-conductor model (orange dots) are displayed.

Plasma frequency (ω_P) and carrier scattering time (τ_S)

The evolution of the charge transport properties of photo-excited LBCO ($x = 11.5\%$) can be better quantified by fitting the transient complex conductivity spectra with a Drude model:

$$\sigma_1(\omega) + i\sigma_2(\omega) = \frac{\omega_P^2}{4\pi} \frac{1}{1 - i\omega\tau_S},$$

where ω_p is the plasma frequency and τ_s the carrier scattering time. Examples of the fits are shown in Figure 5.6 (a.1 and b.1) – dashed lines. In order to mimic the background in the optical spectra, mainly caused by phonon absorptions, two high-frequency Lorentz oscillators have been added and kept constant in all fits. The central frequencies of the oscillators were fixed at 1.35 THz (45 cm^{-1}) and 7.13 THz (237.9 cm^{-1}), with a weight of 2.7 THz (90 cm^{-1}) and 34 THz (1135.6 cm^{-1}) respectively.

The extracted fit parameters, *i.e.* the screened plasma edge frequency $\widetilde{\omega}_P = \omega_P/\sqrt{\varepsilon_{FIR}}$ (where $\varepsilon_{FIR} \simeq 27$) and τ_s, are displayed in Figure 5.7 a and b, both below and above T_C as a function of pump-probe delay. Below T_c (black dots), at delays t $\lesssim$ 1.5 ps the transient optical properties are described equally well by a Drude model with scattering time $\tau_S \gtrsim$ 10 ps. In other words, a fit could be obtained by assuming a perfect conductor (or superconductor) with infinite $\tau_S \rightarrow \infty$:

$$\sigma_1(\omega) + i\sigma_2(\omega) = \frac{\omega_P^2}{8}\delta[\omega = 0] + \frac{\omega_P^2}{4\pi}\frac{i}{\omega}$$

Therefore, the system stays in an extremely high mobility state (with carrier mobilities $\mu \sim 10^3$ - 10^4 $\frac{cm^2}{V \cdot s}$, see also Ref. [45]), compatible with interlayer Josephson tunneling, for a duration lasting longer than 1 ps after photo-excitation. During this early-time dynamics, the plasma frequency $\widetilde{\omega}_P = \frac{4\pi N e^2}{m^*}$ (where *N*, *e*, and *m** are the carrier density, charge, and effective mass, respectively) progressivley increases, reaching values which are compatible with the highest ones observed within the LBCO family [91]. The same early-time dynamics can be extracted also from the fits to the 30 K data, where, starting from the non-conducting ground state, a high-mobility state, also compatible with interlayer superconducting coupling, develops. Fits to $\sigma_1(\omega)+i\sigma_2(\omega)$ at t = 1.5 ps with the perfect-conductor formula are displayed as red dots in Figure 5.7. When analyzing the relaxation dynamics of the photo-induced response at longer time delays (t $\gtrsim$ 2 ps), one can see that, both at 5K and 30 K, the high-mobility state found at t $\lesssim$ 2 ps progressively loses its coherence, with a finite carrier scattering time $\tau_S \sim$ 5 ps setting in, which reduces down to $\tau_S \sim$ 1 ps at later delays. Concomitantly, $\widetilde{\omega}_P$ keeps on increasing, exceeding 1 THz at t $\simeq$ 2.5 ps, and relaxing then back to about 500 GHz.
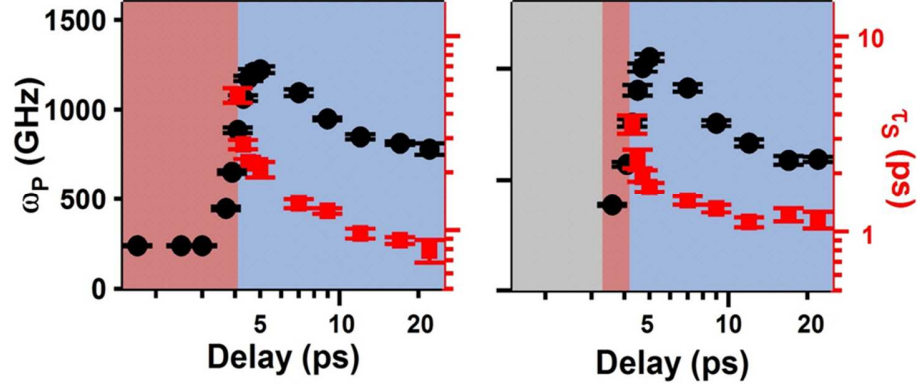
Figure 5.7: Parameters extracted from the Drude fits as a function of pump-probe delay. The grey shaded region indicates the non-conducting regime, where no Drude fit could be carried out. The red shaded area refers to the highly coherent state, where data could be fitted equally well by any $\tau_S \gtrsim 10$ ps. Data are shown both below (black dots) and above T_C (red dots).

The scattering times estimated during the relaxation process ($\tau_s \sim 1 - 5$ ps) are anomalously high for conventional incoherent charge transport. This seems to suggest that, unlike high-energy charge excitation parallel to the CuO_2 planes, light polarized along the c axis may not substantially affect the superconducting condensate and rather act directly on the competing stripe order, thus transiently enhancing interlayer Josephson tunneling. In this framework, the relaxation process observed at t $\gtrsim 2$ ps may be dictated by a progressive increase of temporal fluctuations of superconductivity, in analogy with the interpretation of the equilibrium THz response of $La_{2-x}Sr_xCuO_4$ right below and above T_c reported in Ref [94], which qualitatively matches the above observations.

The experimental evidence suggests that interlayer Josephson coupling is enhanced by light below T_c both at $x = 9.5\%$ and 11.5% doping and even induced above T_c in the stripe phase of $La_{1.885}Ba_{0.115}CuO_4$, combined with the absence of any effect above T_{CO}. This further points towards a possible light-induced melting of the stripe order, which would induce 3D superconductivity in a material where the CuO_2 planes are already superconducting at equilibrium, but interlayer Josephson tunneling is prevented.

Soft X-ray data: evidence for stripe melting

In support of this view, I report here a time-resolved experiment carried out at the DIAMOND light source in Oxford, with the aim of measuring the stripe-peak relaxation dynamics after out-of-plane high-energy charge excitation, using resonant soft X-ray diffraction (RSXD) at the oxygen K-edge (530 eV). The c-axis surface normal cut of the $La_{1.885}Ba_{0.115}CuO_4$ samples makes possible both out-of-plane laser excitation at grazing incidence and RSXD at the relevant wave vector.

The wave vector (h k l) which contains information on the spatial correlations of the doped holes in $La_{1.885}Ba_{0.115}CuO_4$ is (0.23 0 0.65) [95]. This can be seen in Figure 5.8 a, which depicts the x-ray diffraction scan on the charge order peak at T = 10K (blue points), for a phonon energy of 526.6 eV. A Gaussian fit to the data (blue line) shows a clear peak at (0.23 0 0.65). The same scan reported at T = 60K > T_{co} (red dots) displays a featureless profile.

The x-ray scan was repeated as a function of pump-probe delay upon excitation with 800-nm light in the saturation regime of ~ 1 mJ/cm^2 (i.e corresponding to 10^{20} absorbed photons/cm^3). As shown in Figure 5.8 b, the transient intensity of the charge stripe order diffraction peak displays a prompt decrease of about 40% after photo-excitation. This supports the hypothesis that the observed light enhanced (for T < T_C) and the light induced (for T_C < T< T_{SO}) Josephson coupling is related to the melting of the stripe phase.

Furthermore, in a recent study by Khanna et al. it was also shown that the fluence dependence of the enhanced interlayer coupling follows closely that of the stripe order melting [96]. This further corroborates the competing interplay between the two phases.
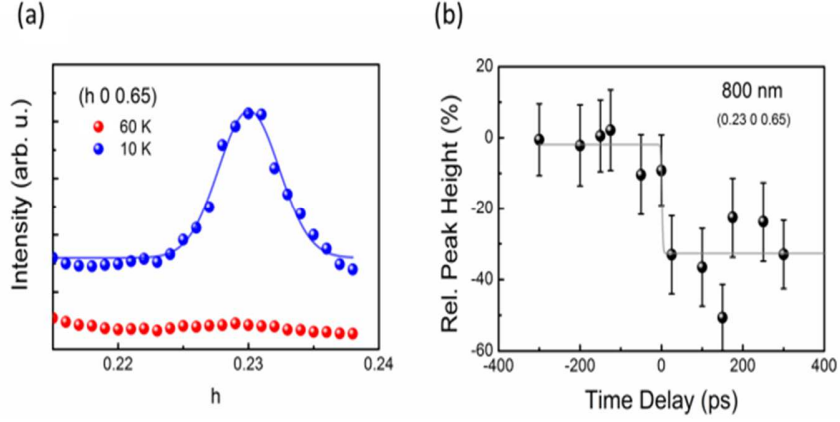
Figure 5.8: Soft x-ray diffraction measurement. (**a**) Resonant soft X-ray diffraction scan of the $La_{1.885}Ba_{0.115}CuO_4$ charge stripe order peak at 10 K (blue), using a photon energy of 526.6 eV (near the oxygen K edge). The blue line is a Gaussian fit to the data. For comparison, the same scan is reported at $T > T_{CO}$ (red), showing a featureless profile. (**b**) Intensity change in the stripe order peak measured at $Q_{stripe} = (0.23\ 0\ 0.65)$ as a function of time delay, after photo-excitation. The pump pulses were tuned to 800-nm wavelength, with polarization perpendicular to the CO_2 planes and a fluence of ~ 1 mJ/cm^2, corresponding to $\sim 10^{20}$ photons/cm^3. The gray line is a guide to the eye.

In-plane pumping

We analyze here another particularity of these measurements, by emphasizing the *polarization selective character* of the enhancement of the Josephson interlayer coupling by melting of the stripe phase. Figure 5.9 compares the complex optical conductivity measured in the stripe phase (T = 30 K) 1.5 ps after excitation with 800 nm light polarized perpendicular (red lines) and parallel (black lines) to the CO_2 planes. The coherent coupling - evidenced by an increase in $\sigma_2(\omega)$ at low frequencies - is far more pronounced in the case of out-of-plane excitation (*i.e.* along c-axis). Moreover, the quasiparticle response in $\sigma_1(\omega)$ is lower than for in-plane excitation.

This underlines further that out-of-plane optical excitation couples only weakly to quasiparticle excitations in quasi-two-dimensional cuprates.
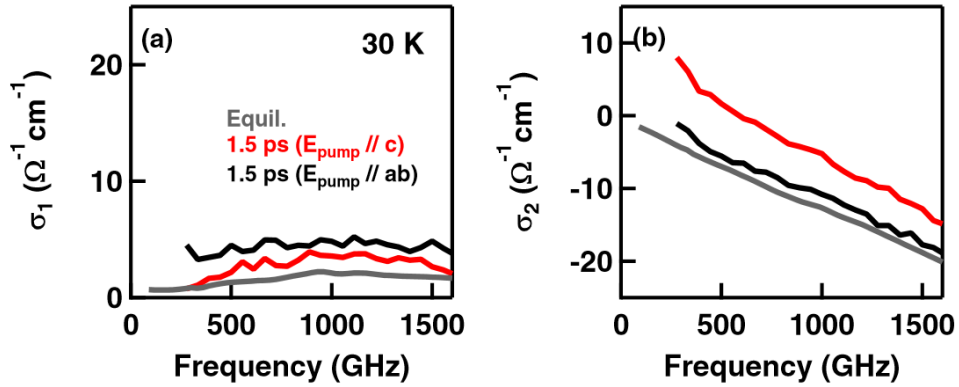
Figure 5.9: Complex optical conductivity of $La_{1.885}Ba_{0.115}CuO_4$ at T = 30 K, 1.5ps upon optical excitation with light polarized perpendicular (red) and parallel (black) to the CO_2 planes. Data are taken at a pump fluence of 2 mJ/cm^2.

5.2. Wavelength dependence

In order to understand how to melt stripe order most efficiently, we also studied the dependence of light-induced superconductivity on the pump wavelength, which is tuned between the mid-infrared (5 µm) and the visible (400 nm) spectral region.

The polarization of the optical pulses was maintained perpendicular to the CuO_2 planes, and tuned to central wavelengths of 5 µm, 2 µm and 400 nm, in addition to the 800 nm case studied above. Nonlinear optical rectification of 800-nm wavelength pulses from a Ti:Sa laser was used to generate the tunable pump pulses: the excitation pulses with ω_{pump} = 2 µm wavelength, difference frequency generation between signal and idler pulses resulted in pulses with ω_{pump} = 5 µm central wavelength, while for obtaining the 400 nm pump pulses we used second harmonic generated from a 1 mm thick BBO crystal. For further details on the pump-pulses generation, consult Appendix A.3.

As previously, the experiments were performed at temperatures below and above T_C, T = 4 K ($T < T_C$) and T = 30 K ($T_C < T < T_{SO}$). In Figure 5.10, the frequency dependent reflectivity is shown as a function of temperature and pump wavelength both at equilibrium (black curves) and at t = 1.5 ps after excitation (colored lines), pump-probe delay which corresponds to the peak amplitude of the transient response.

- For excitation pulses with a central wavelength of ω_{pump} = **5 µm**, no pump-induced effects were detected at any temperature (panels a.1. and a.2), even when applying the highest achievable fluence. As the pump pulses were tuned to shorter wavelengths, a signal of increasing strength emerged.

- For ω_{pump} = **2 µm** wavelength pump pulses, a shift of the equilibrium plasma resonance toward higher frequencies was observed below T_C (panel b.1) and a reflectivity edge appeared at ~220 GHz from the f eatureless equilibrium reflectivity at 30 K (black curve in panel b.2).

- The case of ω_{pump} = **800 nm** optical pump was extensively discussed previously, and it shows the strongest response, with a striking shift of the equilibrium JPR from ~200 GHz to ~600 GHz (panel c.1) at $T < T_C$ and a transient edge observed near 500 GHz for $T_C < T < T_{SO}$ (panel c.2).

- Finally, in the case of optical excitation with ω_{pump} = **400 nm** central wavelength, there is an increase in the sample reflectivity at all frequencies below 1 THz, effect observed also in the above-T_C data (panel d.2.), but no sharp edge was found.

Hence, two opposing trends could be identified when tuning the pump wavelength, both below and above T_C. A transient photo-induced reflectivity edge is measured at frequencies that grow with shorter wavelengths. However, the "quality" of such edge, as identified by its size and width, deteriorates for higher photon energies.

To analyze the origin of these observations quantitatively, we note again that linear optical absorption in this compound increases with photon energy (as seen in the optical conductivity, Figure 5.2). Hence, for a given fluence, the total energy and the number of photons deposited per unit volume varies with the wavelength of the pump pulses. Figure 5.11 shows the fluence dependent spectrally integrated response (measured as the change in the THz electric field peak $\Delta E_R/E_R$ at a pump-probe delay t = 1.5 ps) for all excitation wavelengths where the sample showed optical-induced effects. The pump-probe response shows saturation with fluence for all the excitation light pulses; $\Delta E_R/E_R$ exhibits a well-defined threshold behavior. The data were fit with sigmoid functions (orange lines) which returned threshold fluences anywhere between

less than 1 mJ/cm^2 (for ω_{pump} = 400 nm) and 3 mJ/cm^2 (for ω_{pump} = 2 µm), as presented in detail in Table 5.1.
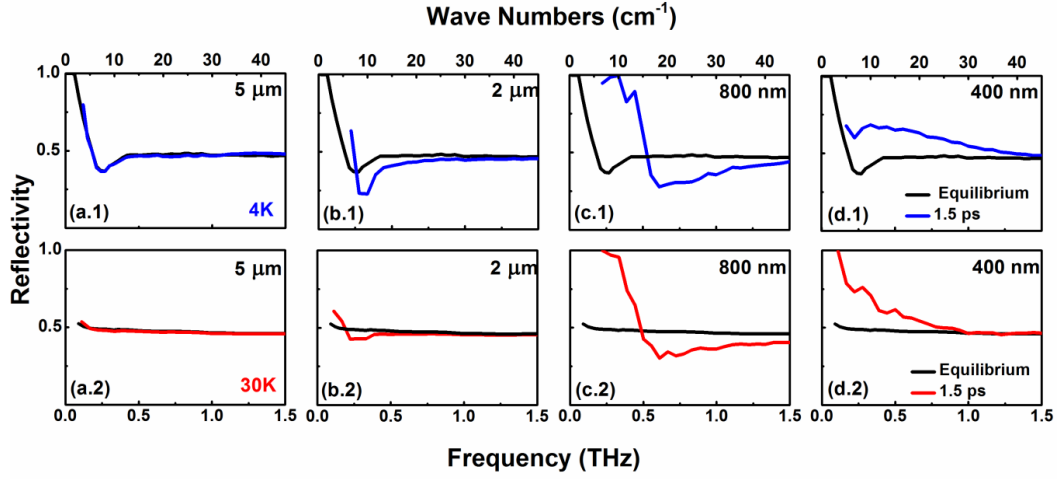
Figure 5.10: Frequency-dependent reflectivity of La$_{1.885}$Ba$_{0.115}$CuO$_4$ measured at equilibrium (black lines) and 1.5 ps after excitation with different pump wavelengths. Data are shown at two different temperatures: T = 4 K (blue) and T = 30 K (red). All data were taken at saturation fluences for all pump wavelengths, corresponding to $\sim 2 \cdot 10^{20}$ photons/cm^3.

However, taking into account the different penetration depths which vary from 2.5 µm to 100 nm for different pump pulses and renormalizing against the total number of absorbed photons per unit volume (see upper scale for each panel), we found that the optical response always saturates for $\sim 10^{20}$ photons/cm^3. This experimental evidence emphasizes that the difference in blue shift and in edge width does not depend on the different excitation conditions.

Pump wavelength λ	Pump penetration depth	Saturation fluence (mJ/cm²)	Saturation fluence E_s(mJ/cm³)	$E_s * \lambda$ (mJ/cm²)	Nr of photons / cm³
400nm	100nm	0.75	$0.31 * 10^5$	1.24	$1.2 * 10^{20}$
800nm	400nm	1.1	$0.15 * 10^5$	1.20	$1.2 * 10^{20}$
2µm	2.5µm	3	$0.058 * 10^5$	1.16	$1.2 * 10^{20}$

Table 5.1: Fluence and number of photons corresponding to the different pump pulses.
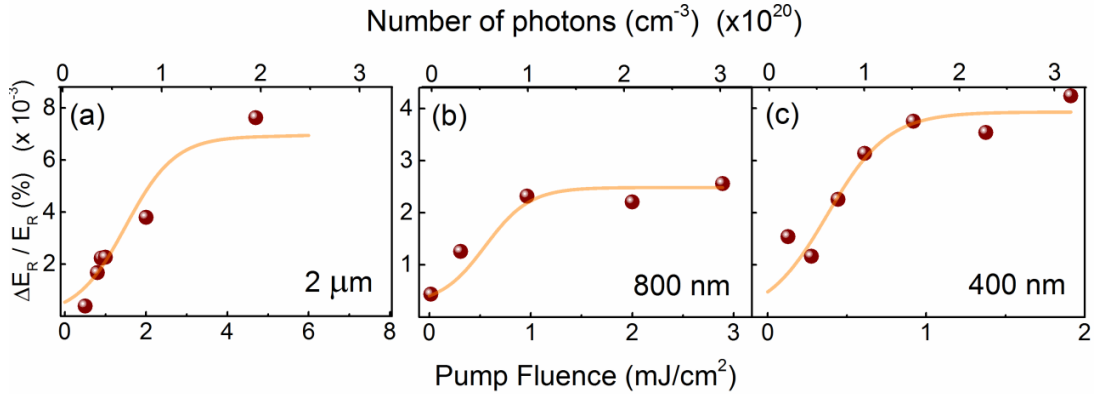
Figure 5.11: Differential time-domain transient $\Delta E_R/E_R$ measured at the THz electric field peak, 1.5 ps after photo-excitation, plotted as a function of pump fluence for different excitation wavelengths. The black lines are sigmoid function fits, indicating threshold fluences of 3.0 mJ/cm^2, 1.1 mJ/cm^2 and 0.75 mJ/cm^2 for 2-µm, 800-nm and 400-nm excitation wavelength, respectively. On the top horizontal scale, the fluence is expressed in terms of total number of absorbed photons per unit volume, returning a saturation value of ~1.2· 10^{20} photons/cm^3, independent of pump wavelength.

The two competing phenomena of enhanced coupling (blue shift of the plasma edge) and increased width of the resonance (decoherence) can be better understood by analyzing the transient complex optical conductivity $\sigma_1(\omega) + i\sigma_2(\omega)$ of the photo-excited material, depicted in Figure 5.12. As already observed in the transient reflectivities, no effect was induced by the 5 µm pump pulses in the real (σ_1) and imaginary (σ_2) part of conductivity at any temperature (panels a.1-a.4).

- In contrast, 1.5 ps after exciting the material with **2 µm** light pulses below T_C, an increase in the imaginary part of the conductivity (panel a.2.) was observed down to the lowest measured frequency, while $\sigma_1(\omega)$ (panel b.2.) was not affected by the pump pulses. Thus, at early time delays, the ohmic response remains gapped and that quasi-particle heating is initially negligible.

- The **800 nm** transient response was already discussed: it is qualitatively similar to the 2 µm optical response, even more pronounced.

- Finally, in the case of **400 nm** light pulses, both below and above T_C, the imaginary part of the conductivity, $\sigma_2(\omega)$, increases (panel a.4.), alongside with a considerable enhancement of $\sigma_1(\omega)$ at all measured frequencies, which is most likely due to resonant quasiparticle excitation. This indicates a mixed

response involving an enhancement in interlayer tunneling *and* an increase in the incoherent transport properties.

A qualitatively similar, however less pronounced response is reported for the striped state above T_C (Figure 5.12, panels a.3 – d.3, a.4 – d.4).
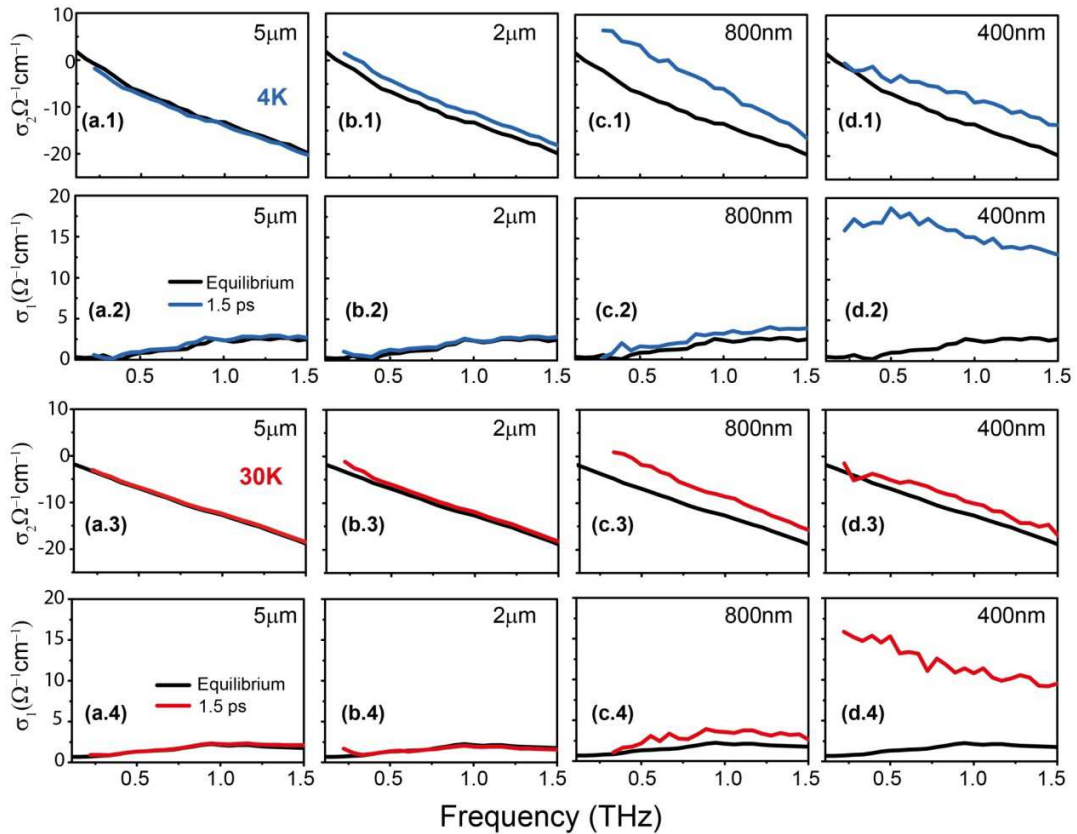
Figure 5.12: Complex optical conductivity of La1.885Ba0.115CuO4 at equilibrium (black) and 1.5 ps after excitation with different pump wavelengths (colored). All data were taken at a pump fluence corresponding to ∼ $2 \cdot 10^{20}$ photons/cm^3, both below (blue) and above (red) T_C.

As already mentioned in the analysis for the 800 nm pump pulse, the energy loss function captures key features of the excited state: it exhibits a peak where $\tilde{\varepsilon}$ crosses zero, that is, at the frequency of the plasma edge. Also, the width of the loss function reflects the scattering rate for superconducting tunneling. In Figure 5.13 the frequency dependent loss function is presented as a function of pump-probe delay and temperature, for all pump-wavelengths. The loss function plots reinforce the

observations discussed above: there is a progressive strengthening of the loss function peak frequency for shorter pump wavelengths. Also, the number of incoherent quasiparticles excited by the pump pulses rises with increasing excitation energy, effect indicated by the broadening of the loss function alongside with the enhancement of the real part of conductivity already discussed. The two dimensional plots show clearly how the incoherent broadening becomes progressively stronger and sets in at earlier delays for shorter wavelength excitation.
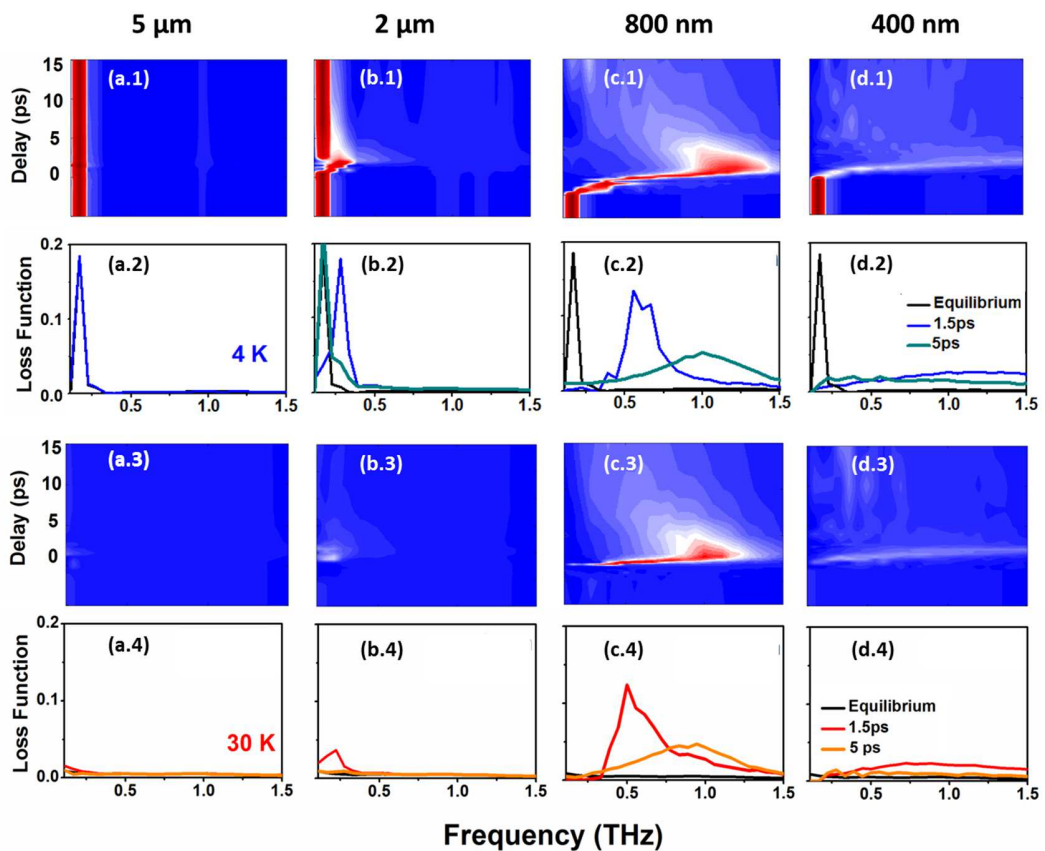
Figure 5.13: Frequency-dependent Energy Loss Function of La1.885Ba0.115CuO4 for different excitation wavelengths, as a function of pump-probe delay, measured below (upper panels) and above (lower panels) T_C. The color plots show the light-induced dynamical evolution of the loss function, while selected line cuts are reported at negative (black), + 1.5 ps (blue and red) and + 5 ps (cyan and orange) time delay. All data corresponds to a pump fluence of $\sim 2 \cdot 10^{20}$ photons/cm^3.

Similar to the analysis performed for 800 nm pump, we now fit the loss function and the other transient optical properties with a Drude model. We extract the screened plasma frequency $\widetilde{\omega}_p$ (loss function peak frequency) and the scattering time τ_S (inverse width of the loss function peak) at all measured temperatures, pump wavelengths and time delays. These two quantities are plotted in Figure 5.14 (a) and (b) at t = 1.5 ps pump-probe delay as a function of excitation wavelength. The scattering time (panel b) shows a dramatic reduction with decreasing pump wavelength. Thus, one can conclude that the carrier lifetime is strongly degraded at short pump wavelengths.

While the induced carrier density scales up with increasing excitation energy, the relaxation into an incoherent state is faster for high-energy light pulses. The balance of these two effects results in an "optimal" excitation condition for light-induced superconductivity in the 800-nm range, as emphasized by the peak in $\Delta\sigma_2$ response showed in Figure 5.14 (c) the pump induced changes in the imaginary conductivity were estimated at ω = 300 GHz, 1.5 ps after the optical excitation).
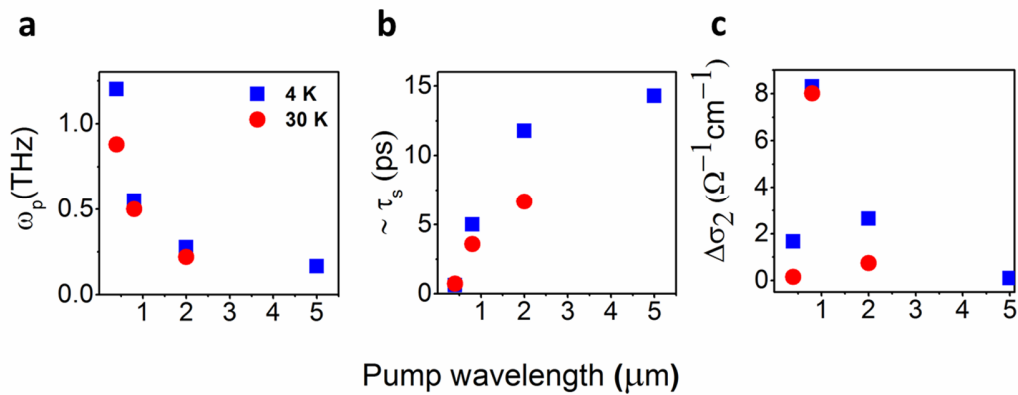
Figure 5.14: Screened plasma frequency (a), scattering time (b) and pump induced changes in the imaginary conductivity estimated at ω = 300 GHz (c) displayed as a function of pump wavelength, for temperatures below (blue dots) and above (dark yellow dots) T_C. ω_p and τ_s were evaluated from the Loss Function curves shown in **Figure 5.13**, while $\Delta\sigma_2$ was estimated from the σ_2 curves shown in **Figure 5.12**. All parameters are represented 1.5 ps after optical excitation with a pump fluence corresponding to ~ $2 \cdot 10^{20}$ photons/cm^3. The parameters $\widetilde{\omega}_p$ and τ_S were also extracted from Drude fits to the optical spectra, in perfect agreement with those estimated from the loss function.

The analysis discussed above reveals that light-induced enhancement of interlayer coupling is most pronounced for intermediate pump wavelengths. This is deconvolved from the progressive deterioration of this signal, which becomes strongest for hot quasi-particles at 400 nm.

5.3. Conclusions

In this chapter I have presented THz time domain spectroscopy studies demonstrating the out-of-plane superfluid density of LBCO can be transiently increased by light polarized perpendicular to the CO2 planes. Highly coherent dynamics were also be induced above T_C, in the stripe phase. Furthermore, the soft x-ray experiment showed that, for this polarization, coupling to the charge stripes is very efficient, with the stripe peak melting promptly following near-infrared photoexcitation.

The data is essentially in favor of the competing orders scenario, proving that enhancement of the Josephson interlayer coupling can be achieved at the expense of the stripe order phase. In this framework, as already discussed above, the absence of any light-induced response in the stripe phase of the 1/8-doped sample can be attributed to the fact that here the CO order parameter and correlation length are stronger and superconductivity is heavily quenched, resulting in a much lower photo-susceptibility of this material.

6

Summary and outlook

In this thesis two different mechanisms for controlling the c-axis Josephson coupling in layered high-T_C superconductors with light fields have been demonstrated and discussed. A brief summary of the results achieved is stated below.

6.1. Coherent control of Josephson physics with Terahertz pulses

- **Soliton excitation**

This work presents a theoretical and experimental study of the Josephson physics initiated by an intense terahertz pulse in a layered superconductor. The main observation is that direct excitation of the plasma resonance with narrowband (~ 25 picoseconds long) terahertz pulses results in the creation of a transparency window in the optical properties. This phenomenon is due to the generation of a slowly propagating mode, confirmed to be a Josephson plasma soliton by the simulations. In order to further

validate the soliton formation, additional experiments combining imaging techniques and free electron laser radiation could be performed.

Vortex excitations are key to a number of fundamental properties of superconductors and have been statically studied with various techniques such as magnetization [97], calorimetry [98], optical spectroscopy [99], [100] and neutron scattering [101]. However, the current study focuses on the out-of-equilibrium dynamic response, which hitherto has largely remained out of reach. The phenomenon observed is also reminiscent to the electromagnetic induced transparency (EIT). This ultrafast optical method of creating flux-carrying phase kinks might be optimized for information transport and storage in fields such as quantum computing [102], [103].

- **Amplification of plasma waves**

This work exploits the nonlinearity of interlayer Josephson tunneling in cuprate superconductors, and demonstrates the possibility to parametrically amplify a terahertz plasma wave. In this case, for strong single-cycle terahertz pulses in resonance with the JPR frequency, a modulation of the optical response around the JPR is observed as a function of pump-probe delay. This translates into a strong reshaping of the optical properties, with the loss function oscillating between positive and negative values, corresponding to damping and amplification of the plasma oscillations. All the theoretical predictions were confirmed by experiment.

These parametric phenomena could, for example, be used to achieve squeezed light at terahertz frequencies [104]. Further, as the Josephson coupling is sensitive to phase fluctuations, new experiments may become possible in which the fluctuations of the superconducting order parameter phase are controlled in the time domain, possibly stabilizing the superconducting state [105], [106].

6.2. Enhancing the interlayer Josephson tunneling through suppression of competing stripe order

This study demonstrates the enhancement of the Josephson interlayer coupling when the competing stripe (charge- and spin-) order is suppressed in the high T_C cuprate $La_{2-x}Ba_xCuO_4$. This is achieved by using high photon energy pulses in the NIR

and MIR range, and is identified in the transient optical response at THz frequencies by a considerable light-induced blue shift of the plasma resonance (below T_C). Furthermore, a similar transient response is found in the non-superconductive state above T_C, indicative of light induced coherent c-axis transport throughout the stripe phase.

Systematic soft x-ray scattering measurements could corroborate the suppression of the CO and of the LTT distortion. The results further support the competing nature between the stripe order and the superconducting phase.

Although the superconducting state was identified in the optical response such as reflectivity, conductivity and loss function, it would be far more compelling to confirm the superconducting nature through the measurement of the Meissner response. Such measurements in a transient state are inherently challenging, however attempts could be undertaken to increase the lifetime of the transient superconducting state. The experiments presented in this work offer the advantage of using 800 nm excitation (as opposed to mid infrared pulses), easing the experimental demands and facilitating the study of the transient state as a function of external parameters, such as magnetic field. One approach to achieve this might also involve the utilization of longer duration light fields to stimulate the transient state.

Appendix A

Experimental methods

In the following I will present in some detail the pump-probe setups employed in this work. A pump-probe measurement is a technique for studying ultrafast phenomena in solids, where an optical *pump pulse* is used to excite the investigated sample, and a subsequent pulse (the *probe*) is used for probing the sample after an adjustable time delay.

In particular, for THz time-resolved spectroscopy, the pump pulse (which could have NIR, MIR or THz wavelength) beam which initiates a change in the far-infrared properties of the sample, on a sub-picosecond time scale, that is further probed by a subsequent THz beam. By varying the time delay, t, between the pump and the probe pulses, the full dynamics of the transient state upon excitation can be recovered. One can define t = 0 in multiple fashions, but here it will be defined as the moment when the pump pulse arrives at the sample surface.

A.1. Near-IR and MIR pump – terahertz probe setup

The time-domain THz spectroscopy measurements presented in this thesis were performed in a reflection geometry. For the table top setup employed for all experiments presented in Chapter 5, the laser source is a Ti:sapphire laser with an output beam of ~100 fs and 800 nm central frequency (Figure A.1). The repetition rate is 1 kHz, while the output power is ~ 3.5 W. The beam is split in two by a first beam-splitter, with

most of the beam used for the **pump pulse**. Due to the tunable wavelength of the pump pulses, different methods were employed for different wavelengths:

- 800 nm light was shined directly onto the sample;
- the 800 nm pulse was shined onto a 1 mm thick β-barium borate (BBO) crystal to obtain the 400 nm pump pulses via second harmonic generation;
- the 800 nm was used as an input for the TOPAS. => 2 µm light
- the 800 nm was used as an input for the TOPAS. Difference frequency generation between the signal and idler pulses (*i.e.* by using a DFG setup) resulted in pulses with $\omega_{pump} = 5$ µm central wavelength. For more detail on the OPA and DFG processes see section A.3.

After generation, the pump pulse hits the sample at normal incidence.

The residual 800 nm beam that is not employed for the pump pulses is further divided in two, with the main part used for generating THz light (the **probe pulse**) and the rest for the EOS detection setup. In order to obtain single-cycle THz pulses, the NIR beam illuminates a large-area photoconductive GaAs-based antenna, which basically consists of a semiconductor device patterned with electrodes that apply a bias across a small (submillimeter scale) strip of semiconductor. The 800 nm light excites carriers from the valence band into the conductance band of the semiconductor. Thus, the applied bias accelerates the charges across the electrode, releasing dipole radiation in the THz regime, as the timescale of this process is in the picoseconds range for GaAs-based antennae. The THz probe pulses generated through the antenna cover a frequency range between 150 GHz and 3 THz, with a controllable polarization via antenna alignment. Note that the time resolution of the experiment is limited instead by the spectral content of the THz.
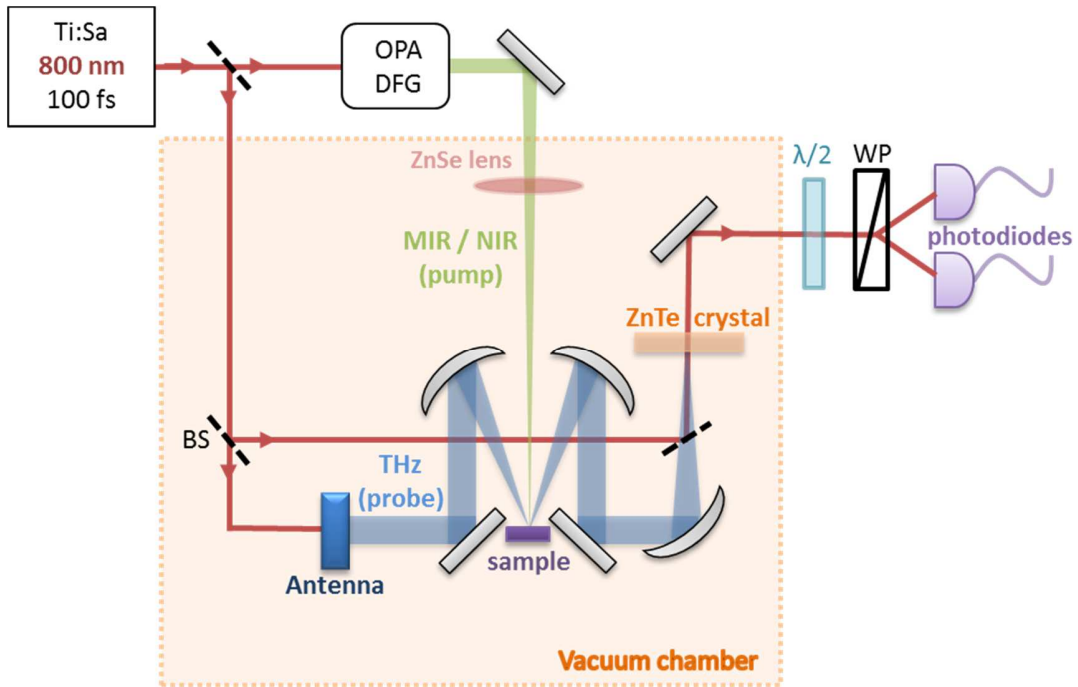
Figure A.1 Scheme of the THz time domain spectroscopy setup used for the measurements, most of which is encapsulated in a vacuum chamber. The MIR (or NIR) pump pulse is focused onto the sample at normal incidence. The THz probe pulse is generated in a photoconductive antenna and impinges on the sample at 30° incidence. The reflected beam is focused onto a ZnTe crystal. A residual 800 nm beam (EOS beam) is focused onto the same position on the crystal, for detection via electro-optic sampling, which makes use of a half wave plate, a Wollaston prism (WP), and two balanced photodiodes.

After generation, the pulses were focused on a ~ 1 mm spot diameter onto the sample surface, at a 30° angle incidence. The reflected electric field was measured by electro-optic sampling in a 1 mm thick ZnTe, procedure that is briefly described below. The THz was generated and detected within a vacuum chamber, which eliminates ringing of the pulses in the time domain due to water absorption.

A.2. Electro-optic sampling (EOS)

Electro-optic sampling is an optoelectronic detection technique used for directly measuring the electric field profile of a THz pulse. A depiction of the electro-optic sampling scheme is shown in Figure A.2. In this procedure, the THz light pulse and a short gating beam are spatially and temporally overlapped, in order to interact in a

nonlinear detection crystal via the Pockels effect. The THz field induces a transient birefringence in the nonlinear detection crystal, which is proportional to the electric field of the pulse. This varying birefringence can be measured by observing the change in polarization state of the gating pulse, at the arrival time of the gating pulse. By shifting the delay between the THz and the sampling pulse, the full spectrum of the THz pulse can be retrieved.

Further, the gating light is decomposed in two orthogonal polarization components by the use of a half waveplate and a Wollaston prism. The resulting beams are measured with a balanced detection including two photodetectors and a lock-in. The instantaneous THz field is proportional with the subtracted signals. In the absence of the THz beam, the sampling beam is initially polarized such that the Wollaston prism splits is into two pulses of equal intensity but opposing polarization. This procedure is very sensitive, allowing detection of THz pulses with less than a nJ energy.
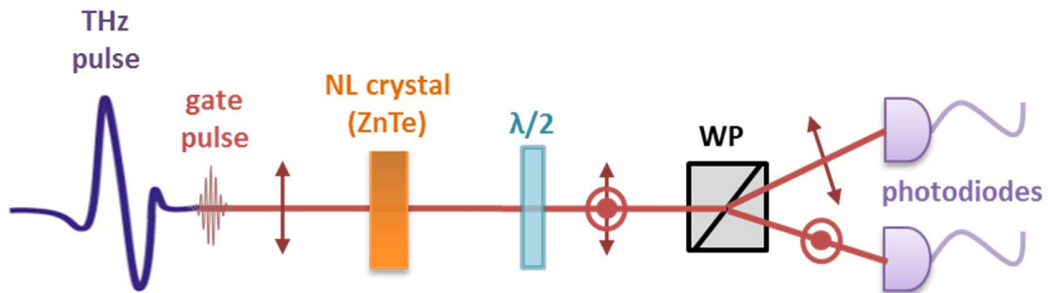
Figure A.2 Electro-optic sampling. The THz pulse (blue) and the gating beam (red) are focused on a nonlinear (NL) crystal. The polarization of the gating beam is rotated in proportion with the applied THz field. The rotation of the polarization is then measured by splitting the polarization components with a half waveplate ($\lambda/2$) and a Wollaston prism (WP) and using a balanced detection scheme. Red arrows indicate the polarization of the sampling beam after various optical elements.

The nonlinear crystals, which stay at the core of the electro-optic technique, that are most frequently used are: ZnTe, GaP, GaSe, inorganic semiconductors (e.g. GaAs, InP, InSb), organic compounds (e.g. DAST, SDTMS) [107], [108]. For our experiment the detection crystal is 110 cut ZnTe with a thickness of 500μm.

A.3. Optical Parametric Amplification (OPA) and Difference Frequency Generation (DFG)

The wavelength range of the pump light used for the experiment shown in Chapter 5 scales from 400 nm to 5000 nm, values which cannot be reached by the fundamental line of the commercial Ti:sapphire lasers. In order to achieve the desired value, we make use of different techniques, such as optical parametric amplification (OPA) for the generation of short near-infrared (NIR) pulses and difference frequency generation (DFG) to achieve mid-infrared (MIR) pulses.

Both OPA and DFG rely on second order optical processes like difference frequency mixing, which will briefly be discussed below. An applied external electric field E will induce a polarization within a medium, which can be expressed as follows:

$$P = \chi^{(1)}E + \chi^{(2)}E^2 + \chi^{(3)}E^3 + \cdots + \chi^{(n)}E^n,$$

where $\chi^{(n)}$ denotes the n-th order susceptibility. The nonlinear order susceptibility terms of the series, $\chi^{(n>1)}$, are much smaller than the linear response $\chi^{(1)}$, and become relevant only when strong enough external fields are applied.

For an incident field of the form

$$E(t) = E_1 e^{-i\omega_1 t} + E_2 e^{-i\omega_2 t} + c.c.,$$

the second order polarization will contain several contributions at frequencies $\omega = 0$ (optical rectification), $2\omega_1$ and $2\omega_2$ (second harmonic generation), $\omega_1 + \omega_2$ (sum frequency generation), $\omega_1 - \omega_2$ (difference frequency generation, described by a term of the type: $P = \chi^{(2)}E_1 E_2^*$).

Optical parametric amplification uses the difference mixing of a high intensity *pump beam* of frequency ω_p and a second so-called *signal beam* at ω_s in order to amplify the later one. In the process of energy transfer from the pump beam to the signal beam, a third *idler beam* is also generated, at frequency $\omega_i = \omega_p - \omega_s$. If k_p, k_s, k_i are the wavevectors of pump, signal and idler beam respectively, conservation of momentum requires that: $\vec{k_p} = \vec{k_s} + \vec{k_i}$. This condition is called phase-matching and it is rather

difficult to achieve in practice, given that $k = n(\omega)\omega/c$, with the refractive index being frequency dependent.
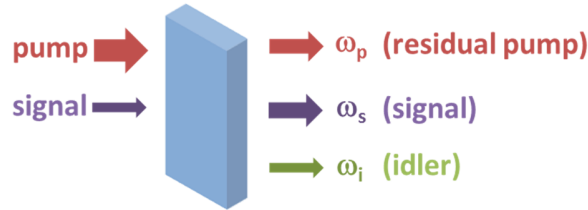
Figure A.3 Sketch of difference frequency mixing

Difference frequency generation also uses the $\chi^{(2)}$ process described above to generate the difference frequency between the signal and idler beams produced by optical parametric amplification. By this, the spectral range of the OPA is extended to mid-infrared (MIR). The main distinction between OPA and DFG consists in the intensity ratio between the pump and the signal beam. In a typical OPA, the pump is usually several orders of magnitude stronger than the initial signal beam (*i.e.* the process is in the undepleted pump regime). In the MIR generation the two beams have nearly the same intensity.

As already mentioned, for the experiments in Chapter 5 a commercial Ti:sapphire laser source was used, which emits pulses centered at 800 nm wavelength. Optical parametric amplification was used to convert the 800 nm pulses to NIR light, and then combined with DFG to tune the wavelength of the final output pulses from 5 µm up to 17 µm.

The optical parametric amplifier (OPA) was a commercial **TOPAS** from Coherent, which is schematically depicted in Figure A.4. This is a two-stage OPA which uses 800 nm light to generate a near-infrared (NIR) signal beam in the first stage, which is then amplified in the second stage.

The initial 800 nm beam is split in two, with most of the light used for the second-stage amplification process. The fraction of the beam sent to the first stage is further split in two, with part of the beam used to generate 'white light' (after going through a sapphire crystal) which will provide the tunable seed beam for the parametric amplification. The white light is mixed with the rest of the first stage 800 nm beam in a nonlinear crystal: the 800 nm pulse should arrive at the same time with the chosen color

of the white light spectrum. Phase matching for optical parametric amplification can be achieved in a birefringent crystal (in this case, β-barium borate (BBO), due to its e□cient phase matching in the NIR).
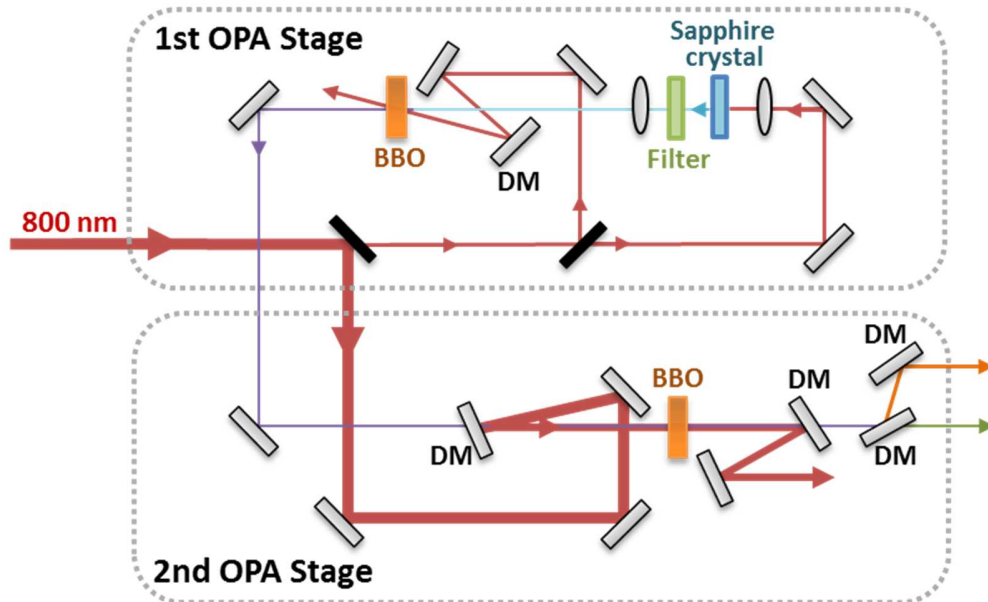
Figure A.4 Schematic diagram of a two stage optical parameter amplifier. Red lines represent the pump light at 800 nm, the blue line – white light, purple light – output NIR beams (orange – idler, green - signal). BBO - β-barium borate, DM – dichroic mirror.

The signal beam is sent on to the second stage, where it is mixed again in a second BBO crystal with the higher power 800 nm beam. In the second stage the relative propagation of the signal and the pump beams are collinear, to maximize the amplification efficiency. In the end, the pump beam will be separated from the NIR beams using a dichroic mirror. One could also use dichroic mirrors to separate the signal and idler beams (not the case here). If the beams are cross-polarized, a waveplate can also be used to select a single beam.

In order to extend the spectral range of the OPA into the MIR, the co-propagating signal and idler beams are guided into a commercial Coherent **NDFG** system. This is built in a non-collinear geometry, so the MIR light is spatially separated from the residual signal and idler beams as they propagate. The resulting MIR pulse spectra are measured by using a Michelson interferometer and a MCT detector. As mentioned above, the TOPAS

OPA used in the experiments described in this thesis, combined with the NDFG system, gives output pulses up to 17 µm in wavelength.

A.4. Tilted pulse front technique for intense THz pulses generation

The generation of high intensity broad-band THz radiation can be achieved through optical rectification of femtosecond near-infrared laser radiation in nonlinear crystals. In particular, the tilted pulse front technique in materials with high nonlinear susceptibility, such as lithium niobate (LiNbO$_3$), allows for the generation of microjoule pulse energies and electric fields reaching megavolts per centimeter.

In this insulator the gap is much larger than the NIR photon energy, thus preventing two-photon absorption and allowing for higher excitation powers [109]. Efficient optical rectification requires that the group velocity of the near-infrared beam, v_{NIR}, matches the phase velocity of the generated terahertz pulse, v_{THz}. Unfortunately, in LiNbO$_3$ the near-infrared group velocity is about twice as large as the terahertz phase velocity [110]. This issue can be overcome by tilting the intensity front of the near-infrared radiation by an angle γ, such that the modified phase matching condition becomes:

$$v_{NIR} cos\gamma = v_{THz}.$$

In the case of LiNbO$_3$ the optimum tilt angle inside the crystal is γ = 63°. This is achieved by diffracting the 800 nm light off a grating [106].
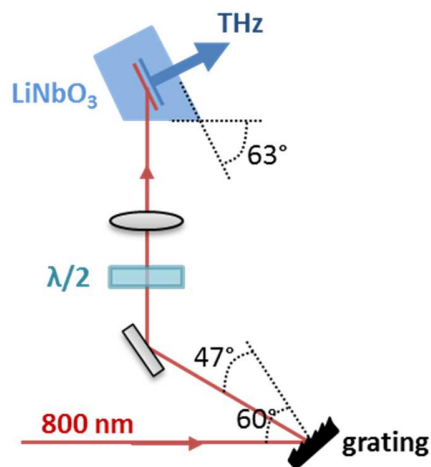
Figure A.5 Tilted pulse front technique for THz generation in LiNbO3 crystals

Figure A.5 depicts a simplified sketch of the experimental implementation of the tilted pulse front setup. The 800 nm light impinges on a blazed grating; the beam is polarized parallel to the plane of incidence. After diffraction off the grating, a λ/2-wave plate rotates the polarization of the light by 90°, to be parallel to the optical axis of the LiNbO$_3$ crystal. Next, the beam is collimated by passing through a lens and then shined onto the nonlinear crystal.

Appendix B

Matlab code for numerically solving the sine-Gordon equation

```matlab
clear all;

% material parameters
%------------------------------------------------------------------------
    epsilon_inf = 27;    % high frequency permittivity
    omega_J = 0.5*2*pi; % Josephson Plasma resonance (in THz)
    lambda_J = 20;       % Josephson penetration depth (in micrometers)
%------------------------------------------------------------------------

% pump field parameters:
%------------------------------------------------------------------------
    E0 = 8.0;                % Intensity: E0=1.0 <=> E0=30kV/cm
    omega_field =1;          % frequency: multiple of omega_J
    T = 2*pi / omega_field;
    delta_pulse = 0.5*T;              % width of the pulse
    center_pulse = 3*delta_pulse;     % center of the pulse
%------------------------------------------------------------------------

% probe field parameters:
%------------------------------------------------------------------------
    E0_probe = 0.001;    % Intensity
    omega_probe = 1.0;   % frequency: multiple of omega_J
    delta_probe = 1*T;
%------------------------------------------------------------------------

% other input parameters:
%------------------------------------------------------------------------
    delay_probe = 0.2*T;    % pump-probe delay
    n_sampling = 50;        % number of sampling points per cycle
    dt = T/n_sampling;      % time resolution

t_i = 0;
t_f = floor((1*center_pulse + 150*T)/dt)*dt;
z_max = t_f/dt+1;           % number of steps in time
t = t_i:dt:t_f;             % time variable used for numerical calculation
```

```matlab
t_real = t./omega_J;      % time variable used for plotting (in ps)

K = 0.2;    % K=dt/dx is a numerical parameter
            % K<1 to guarantee convergence

deltax = dt/K;
nr_i = ceil(z_max*K);  % number of steps in x
                       % for nr_i<z_max*K, reflection at the backend
                       % of the sample may occur
m = nr_i+1;
x_i = 0.0;
x_f = nr_i*deltax;
x = x_i: deltax: x_f;  % space variable used for numerical calculation
x_real = x*lambda_J;   % space variable for plotting (in micrometers)

phi = pi/2;            % phase difference between pump and probe pulses
n_phi = size(phi,2);

df = 1/(t_f-t_i);
f_i = 0;
f_f = df*(z_max-1);
f = f_i:df:f_f;
omega = f*2*pi;
domega = df*2*pi;

ind_j = round(1/domega);
ind_delta = ceil(2*pi/delta_pulse/domega/100);
ind_omega_i = max(ind_j-30*ind_delta);
ind_omega_f = min(ind_j+30*ind_delta);
n_omega = ind_omega_f - ind_omega_i +1 ;
n_delays = size(delay_probe,2);
Loss_matrix = zeros (n_delays, n_omega);
%-------------------------------------------------------------------

n_iter=1;
for n_iter = 1:n_phi

center_probe = center_pulse + delay_probe;

Eprobe_r_sum = zeros(size(t));
Eprobe_r_sum_static = zeros(size(t));

E_pump = zeros(1, z_max);
E_probe = zeros(1, z_max);

Eprobe_r_plus = zeros(1, z_max);
omega_J_inhom = 1.0*ones(size(x));
            % inhomogeneities are accounted by a space dependent JPR
            % omega_J_inhom = 1.0 <=> no inhomogeneity


% defining pump and probe pulses:
%-------------------------------------------------------------------
```

```matlab
    E_probe = E0_probe*sin(omega_probe*t)
                 .*(exp(-(t-center_probe).^2/delta_probe^2));
    E_pump = E0*sin(omega_field*t+phi(n_iter))
                 .*(exp(-(t-center_pulse).^2/delta_pulse^2));
    E = E_pump + E_probe;
%------------------------------------------------------------------

    tau = 10;
    y_B = zeros(m, length(t));

% pump-probe procedure (used in the current code):
     % calculate the space and time dependent phase difference
     % after the pump pulse; then probing the resulting state
% an alternate procedure (not shown here)
     % calculate the phase given by the pump,
     % then the phase given by the pump and probe;
     % take the difference
%------------------------------------------------------------------
    t_probe = 100;
    [Epump_r, phase_J_B] = Loop_sine_Gordon(E_pump, epsilon_inf, K,
nr_i, x, t, deltax, dt, omega_J, lambda_J, tau, y_B', omega_J_inhom,
omega_field, t_probe);

    tau = 40;
    [Eprobe_r_static, phase_J] = Loop_sine_Gordon(E_probe, epsilon_inf,
K, nr_i, x, t, deltax, dt, omega_J, lambda_J, tau, y_B', omega_J_inhom,
omega_field, t_probe);
    [Eprobe_r_breather, phase_J] = Loop_sine_Gordon(E_probe,
epsilon_inf, K, nr_i, x, t, deltax, dt, omega_J, lambda_J, tau,
phase_J_B', omega_J_inhom, omega_field, t_probe);

    Eprobe_r_sum = Eprobe_r_sum + Eprobe_r_breather;
    Eprobe_r_sum_static = Eprobe_r_sum_static + Eprobe_r_static;
%------------------------------------------------------------------

% calculating optical properties
%------------------------------------------------------------------
    E_f = conj(fft(E_probe));
    E_r_f = conj(fft(Eprobe_r_breather));
    reflectivity = E_r_f./E_f;
    I = find(abs(reflectivity(1:round(z_max/2)))<=10);
    Loss = imag(-((reflectivity+1)./(reflectivity-1)).^2);
    Loss_matrix (n_iter, :) = Loss(ind_omega_i: ind_omega_f);

    E_r_f_bre = conj(fft(Eprobe_r_breather));
    E_r_f_sta = conj(fft(Eprobe_r_static));
    reflectivity_bre = E_r_f_bre./E_f;
    reflectivity_sta = E_r_f_sta./E_f;
    Loss_bre = imag(-((reflectivity_bre+1)./(reflectivity_bre-1)).^2);
    Loss_sta = imag(-((reflectivity_sta+1)./(reflectivity_sta-1)).^2);
%------------------------------------------------------------------
```

```matlab
end

% example of plotting various optical properties
          % reflectivity and Loss function):
%----------------------------------------------------------------------
figure;
plot(omega(ind_omega_i:ind_omega_f),
                abs(reflectivity_sta(ind_omega_i:ind_omega_f)));
hold on;
plot(omega(ind_omega_i:ind_omega_f),
                abs(reflectivity_bre(ind_omega_i:ind_omega_f)), 'r');
xlabel('Frequency (w/w_J_P_R)'); ylabel('Reflectivity');

figure;
plot(omega(ind_omega_i:ind_omega_f),
                Loss_sta(ind_omega_i:ind_omega_f));
hold on;
plot(omega(ind_omega_i:ind_omega_f),
                Loss_bre(ind_omega_i:ind_omega_f), 'r');
xlabel('Frequency (w/w_J_P_R)'); ylabel('Loss Function');
%----------------------------------------------------------------------
%----------------------------------------------------------------------


function [Ereflect, phase_J] = Loop_sine_Gordon(E, epsilon_inf, K,
nr_i, x, t, deltax, dt, omega_J, lambda_J, tau, y_B, omega_J_inhom,
omega_field, t_probe)
% output parameters:
     % the reflected field
     % the phase as a function of time and space

m = nr_i +1;
x_i = min(x);
x_f = max(x);

y = zeros(1,m);          % variable phase at current time, t
y_minus = zeros(1,m);    % variable phase at previous moment in time, t-1
y_plus = zeros(1,m);     % variable phase at a latter moment in time, t+1
g = zeros(1,m);          % dy/dt at t=0

r = 1/tau;               % damping factor

B_xt = zeros(round(m/10),length(t));
                    % saves the phase as a function of time and space

for index = 1: length(t)
    y_B_vec = [y_B(index, :), zeros(1, m-round(m/10))];

    % implementing boundary conditions:
    if index == 1
```

```matlab
        y_plus(1) = (1-r*dt/2
            -K/sqrt(epsilon_inf)*(omega_J_inhom(1))^2)*dt*g(1)
            +(1-K^2)*y(1)+K^2*y(2)
            -dt^2/2*(omega_J_inhom(1))^2*sin(y(1)).*cos(y_B_vec(1))
            +K/sqrt(epsilon_inf)*dt*E(index);
        y_plus(m) = (1-r*dt/2
            -K/sqrt(epsilon_inf)*(omega_J_inhom(m))^2)*dt*g(m)
            +(1-K^2)*y(m)+K^2*y(m-1)
            -dt^2/2*(omega_J_inhom(m))^2*sin(y(m)).*cos(y_B_vec(m));
        y_plus(2:m-1) = (1-r*dt/2)*dt*g(2:m-1)
            +(1-K^2)*y(2:m-1)+K^2/2*(y(3:m)+y(1:m-2))
            -dt^2/2*(omega_J_inhom(2:m-1)).^2.*sin(y(2:m-1))
            .*cos(y_B_vec(2:m-1));
        Er(index) = 2*(omega_J_inhom(1))^2*g(1)-E(index);

        y_minus = y;
        y = y_plus;
    else
        y_plus(1) = ((r*dt/2+K/sqrt(epsilon_inf)*(omega_J_inhom(1))^2
            -1)*y_minus(1)+2*(1-K^2)*y(1)+2*K^2*y(2)
            +2*dt*K/sqrt(epsilon_inf)*E(index)
            -cos(y_B_vec(1)).*dt^2*(omega_J_inhom(1))^2*sin(y(1)))
            /(1+r*dt/2+K/sqrt(epsilon_inf)*(omega_J_inhom(1))^2);
        y_plus(m) = ((r*dt/2+K/sqrt(epsilon_inf)*(omega_J_inhom(m))^2
            -1)*y_minus(m)+2*(1-K^2)*y(m)+2*K^2*y(m-1)
            -cos(y_B_vec(m)).*dt^2*(omega_J_inhom(m))*sin(y(m)))
            /(1+r*dt/2+K/sqrt(epsilon_inf));
        y_plus(2:m-1) = ((r*dt/2-1)*y_minus(2:m-1)+2*(1-K^2)
            *y(2:m-1)+K^2*(y(3:m)+y(1:m-2))-dt^2
            *cos(y_B_vec(2:m-1)).*(omega_J_inhom(2:m-1))
            .^2.*sin(y(2:m-1)))/(1+r*dt/2);
        Er(index) = (omega_J_inhom(1))^2*(y_plus(1)
            -y_minus(1))/dt-E(index);

        y_minus = y;
        y = y_plus;
    end

    B_xt(:, index) = y_plus(1:round(m/10));

end
x_real = x.*lambda_J;
t_real = t./omega_J;

% output parameters of the Loop_sine_Gordon function:
      % the reflected field
      % the phase as a function of time and space
%-----------------------------------------------------------------
Ereflect = Er;
```

```matlab
phase_J = B_xt;
%----------------------------------------------------------------------

% example of 2D plot of the phase as a function of time and space
%----------------------------------------------------------------------
figure;
image(t_real, x_real(1:round(m/10)), B_xt(1:round(m/10),:), ...
            'CDataMapping', 'scaled');
xlabel('time (ps)'); ylabel('x (um)');
colorbar;
axis xy;
%----------------------------------------------------------------------
```

Role of the Author

This thesis is the result of multiple collaborations. In the following, I will present in more detail my contribution to this work.

The projects at the core of this thesis were conceived by A. Cavalleri.

Nonlinear physics of the Josephson plasma resonance projects:

The $La_{1.84}Sr_{0.16}CuO_4$ samples were grown by S. Pyon, T. Takayama and H. Takagi. The experimental data were measured and analyzed by A. Dienst and D. Fausti at the free electron laser in Dresden. The model used for numerically solving the sine-Gordon equation which was utilized to describe this experiment was implemented in a MATLAB code developed by the author with guidance from prof. M. Eckstein and L. Zang. The author performed the simulations.

All samples from the LBCO cuprate family were grown and characterized by G. D. Gu and J. P. Hill. The experimental set-up used for parametrically amplifying the JPW in $L_{1.905}B_{0.095}CuO_4$ was built by S. Rajasekaran, who also collected the data. The data was simulated by S. Rajasekaran and the author, using a modified version of the MATLAB code developed by the author for solving the sine-Gordon equation.

Competing charge and superconducting orders in LBCO project:

The low frequency THz optics set-up which was used for the measurements shown in Chapter 5 was developed by D. Nicoletti and S. Kaiser. Measurements with 800nm pump pulses were taken by D. Nicoletti and the author. The set-up was modified by the author for the pump wavelength dependence measurements. The wavelength dependence data was acquired by the author with the guidance of D. Nicoletti. Calculation of the full transient optical response was performed by the author, using a MATLAB code developed by C. Hunt. The analysis and interpretation on the wavelength dependent data were performed by the author, under the supervision of D. Nicoletti and A. Cavalleri. The soft x-ray data were measured at the DIAMOND light source, by the author, V. Kahnna, S. Rajasekaran, D. Nicoletti and M. Petrich.

List of Publications

The results presented are based on the following articles:

Parametric amplification of a superconducting plasma wave
S. Rajasekaran, **E. Casandruc**, Y. Laplace, D. Nicoletti, G. D. Gu, S. R. Clark, D. Jaksch & A. Cavalleri, *Nature Physics (2016)*

Wavelength-dependent optical enhancement of superconducting interlayer coupling in La$_{1.885}$Ba$_{0.115}$CuO$_4$
E. Casandruc, D. Nicoletti, S. Rajasekaran, Y. Laplace, V. Khanna, G. D. Gu, J. P. Hill, and A. Cavalleri, *Physical Review B*, 91, 17 (2015)

Optically-induced superconductivity in striped La$_{2-x}$Ba$_x$CuO$_4$ by polarization-selective excitation in the near infrared
D. Nicoletti, **E. Casandruc**, Y. Laplace, V. Khanna, C. R. Hunt, S. Kaiser, S. S. Dhesi, G. D. Gu, J. P. Hill, A. Cavalleri, *Physical Review B*, 90, 100503(R) (2014)

Optical excitation of Josephson plasma solitons in a cuprate superconductor
A. Dienst, **E. Casandruc**, D. Fausti, L. Zhang, M. Eckstein, M. Hoffmann, V. Khanna, N. Dean, M. Gensch, S. Winnerl, W. Seidel, S. Pyon, T. Takayama, H. Takagi & A. Cavalleri, *Nature Materials*, 12, 535-541 (2013)

Acknowledgement

I would like to express my gratitude to my supervisor, Andrea Cavalleri, for providing me scientific guidance and the opportunity to work on this project. Thank you for your patient and helpful support.

I have been fortunate to also have Martin Eckstein as a supervisor. I am very grateful for the constant support you gave me in the first two years of my doctoral studies, in my effort of simulating the sine-Gordon equation.

Special thanks go towards Srivats for being so smart, always ready to listen to my questions, and - most importantly - always ready to help. It was a pleasure to talk to you, both on a professional and personal level. I would like to thank Daniele, for making my first experience with an optics lab enjoyable, and for all the guidance throughout the LBCO project. Lijian, thank you for all your help, for the passion you were putting in everything you did, including deriving equations. I have benefited greatly from your experience.

With great emphasis, I would like to thank my parents and my sister for their constant support that pushed me forward. Special thanks to my daughter and personal German teacher, Sabina. You are both the source and the 'black hole' of my energy, in the best possible way, and words are not enough to tell you how lucky I am to have you in my life. Albert, thank you for ten full and inspiring years; we have done a great job together. Florin – special thanks for your permanent willingness to help.

Sven, Mariana, Alice – thank you for making our office such a friendly and enjoyable working environment; Sven, I will especially miss our Monday morning talks; Mariana, I am still trying to master the art of calm from you. Tobia, heart-felt thanks for your advices, constant support, and most importantly for all the sushi outings. Andrea, Ivanka, Matthias, Thomas, Yannis, Razvan, Michelle – thank you for improving my everyday experience in Hamburg. I will sorely miss you all.

My acknowledgement list would not be complete without the colleagues from the IMPRS doctoral school, among which many are now my friends. I am so grateful to have had you when I started my Hamburg adventure, for everything is easier with friends around.

Bibliography

[1] M. Dressel and G. Grüner, *Electrodynamics of Solids: Optical Properties of Electrons in Matter*. Cambridge Univ. Press, 2002.

[2] C. Kittel, *Introduction to Solid State Physics*. New York: Wiley, 2005.

[3] A. V. Ustinov, H. Kohlstedt, M. Cirillo, N. F. Pedersen, G. Hallmanns, and C. Heiden, "Coupled fluxon modes in stacked $Nb/AlO_x/Nb$ long Josephson junctions," *Phys. Rev. B*, vol. 48, no. 14, pp. 10614–10617, Oct. 1993.

[4] K. Tamasaku, Y. Nakamura, and S. Uchida, "Charge dynamics across the CuO_2 planes in $La_{2-x}Sr_xCuO_4$," *Phys. Rev. Lett.*, vol. 69, no. 9, pp. 1455–1458, Aug. 1992.

[5] J. G. Bednorz and K. A. Müller, "Possible highTC superconductivity in the Ba−La−Cu−O system," Z. Physik B - Condensed Matter, vol. 64, no. 2, pp. 189–193.

[6] R. J. Cava, R. B. van Dover, B. Batlogg, and E. A. Rietman, "Bulk superconductivity at 36 K in $La_{1.8}Sr_{0.2}CuO_4$," *Phys. Rev. Lett.*, vol. 58, no. 4, pp. 408–410, Jan. 1987.

[7] A. V. Narlikar, *Superconductors*. Oxford University Press, 2014.

[8] M. K. Wu *et al.*, "Superconductivity at 93 K in a new mixed-phase Y-Ba-Cu-O compound system at ambient pressure," *Phys. Rev. Lett.*, vol. 58, no. 9, pp. 908–910, Mar. 1987.

[9] H. Maeda, Y. Tanaka, M. Fukutomi, and T. Asano, "A new high-Tc oxide superconductor without a rare earth element," *Jpn J Appl. Phys. 27 L209*, 1988.

[10] S. N. Putilin, E. V. Antipov, O. Chmaissem, and M. Marezio, "Superconductivity at 94 K in $HgBa_2CuO_{4+\delta}$," *Nature*, vol. 362, no. 6417, pp. 226–228, Mar. 1993.

[11] A. Schilling, M. Cantoni, J. D. Guo, and H. R. Ott, "Superconductivity above 130 K in the Hg–Ba–Ca–Cu–O system," *Nature*, vol. 363, no. 6424, pp. 56–58, May 1993.

[12]   P. A. Lee, N. Nagaosa, and X.-G. Wen, "Doping a Mott insulator: Physics of high-temperature superconductivity," *Rev. Mod. Phys.*, vol. 78, no. 1, pp. 17–85, Jan. 2006.

[13]   P. A. Lee, "From high temperature superconductivity to quantum spin liquid: progress in strong correlation physics," *Rep. Prog. Phys.*, vol. 71, no. 1, p. 12501, 2008.

[14]   *Principles of Terahertz Science and Technology*. Boston, MA: Springer US, 2009.

[15]   R. Kleiner, F. Steinmeyer, G. Kunkel, and P. Müller, "Intrinsic Josephson effects in $Bi_2Sr_2CaCu_2O_8$ single crystals," *Phys. Rev. Lett.*, vol. 68, no. 15, pp. 2394–2397, Apr. 1992.

[16]   R. Kleiner and P. Müller, "Intrinsic Josephson effects in high-T_C superconductors," Phys. Rev. B, vol. 49, no. 2, pp. 1327–1341, Jan. 1994.

[17]   R. Kleiner, P. Müller, H. Kohlstedt, N. F. Pedersen, and S. Sakai, "Dynamic behavior of Josephson-coupled layered structures," *Phys. Rev. B*, vol. 50, no. 6, pp. 3942–3952, Aug. 1994.

[18]   B. D. Josephson, "Possible new effects in superconductive tunnelling," *Physics Letters*, vol. 1, no. 7, pp. 251–253, Jul. 1962.

[19]   O. M. Braun and Y. S. Kivshar, *The Frenkel-Kontorova model*. New York: Springer, 2004.

[20]   Y. S. Kivshar and B. A. Malomed, "Dynamics of solitons in nearly integrable systems," *Rev. Mod. Phys.*, vol. 61, no. 4, pp. 763–915, Oct. 1989.

[21]   V. Zharnitsky, I. Mitkov, and M. Levi, "Parametrically forced sine-Gordon equation and domain wall dynamics in ferromagnets," *Phys. Rev. B*, vol. 57, no. 9, pp. 5033–5035, Mar. 1998.

[22]   V. Zharnitsky, I. Mitkov, and N. Grønbech-Jensen, "π kinks in strongly ac driven sine-Gordon systems," *Phys. Rev. E*, vol. 58, no. 1, pp. R52–R55, Jul. 1998.

[23]   V. G. Ivancevic and T. T. Ivancevic, "Sine-Gordon Solitons, Kinks and Breathers as Physical Models of Nonlinear Excitations in Living Cellular Structures," *ResearchGate*, vol. 31, May 2013.

[24]   J. Orenstein and A. J. Millis, "Advances in the Physics of High-Temperature Superconductivity," *Science*, vol. 288, no. 5465, pp. 468–474, Apr. 2000.

[25]   V. K. Thorsmølle, R. D. Averitt, M. P. Maley, L. N. Bulaevskii, C. Helm, and A. J. Taylor, "C-axis Josephson plasma resonance observed in $Tl_2Ba_2CaCu_2O_8$ superconducting thin films by use of terahertz time-domain spectroscopy," Optics Letters, vol. 26, no. 16, p. 1292, Aug. 2001.

[26]   A. M. Gerrits, A. Wittlin, V. H. M. Duijn, A. A. Menovsky, J. J. M. Franse, and P. J. M. van Bentum, "Josephson plasma oscillations in $La_{1.85}Sr_{0.15}CuO_4$," *Physica C: Superconductivity*, vol. 235, pp. 1117–1118, Dec. 1994.

[27]   S. V. Dordevic, S. Komiya, Y. Ando, and D. N. Basov, "Josephson Plasmon and Inhomogeneous Superconducting State in $La_{2-x}Sr_xCuO_4$," Phys. Rev. Lett., vol. 91, no. 16, p. 167401, Oct. 2003.

[28]   J. M. Rowell, "Magnetic Field Dependence of the Josephson Tunnel Current," *Phys. Rev. Lett.*, vol. 11, no. 5, pp. 200–202, Sep. 1963.

[29]   F. Geniet and J. Leon, "Energy Transmission in the Forbidden Band Gap of a Nonlinear Chain," *Phys. Rev. Lett.*, vol. 89, no. 13, p. 134102, Sep. 2002.

[30]   U. Welp, K. Kadowaki, and R. Kleiner, "Superconducting emitters of THz radiation," *Nat Photon*, vol. 7, no. 9, pp. 702–710, Sep. 2013.

[31]   N. Martinov and N. Vitanov, "On some solutions of the two-dimensional sine-Gordon equation," *J. Phys. A: Math. Gen.*, vol. 25, no. 8, p. L419, 1992.

[32]   D. E. McCumber, "Effect of ac Impedance on dc Voltage☐Current Characteristics of Superconductor Weak☐Link Junctions," *Journal of Applied Physics*, vol. 39, no. 7, pp. 3113–3118, Jun. 1968.

[33]   K. Inomata et al., "Macroscopic Quantum Tunneling in a d-Wave High-TC $Bi_2Sr_2CaCu_2O_{8+\delta}$ Superconductor," Phys. Rev. Lett., vol. 95, no. 10, p. 107005, Sep. 2005.

[34]   X. Y. Jin, J. Lisenfeld, Y. Koval, A. Lukashenko, A. V. Ustinov, and P. Müller, "Enhanced Macroscopic Quantum Tunneling in $Bi_2Sr_2CaCu_2O_{8+\delta}$ Intrinsic Josephson-Junction Stacks," Phys. Rev. Lett., vol. 96, no. 17, p. 177003, May 2006.

[35]   R. D. Averitt, G. Rodriguez, A. I. Lobad, J. L. W. Siders, S. A. Trugman, and A. J. Taylor, "Nonequilibrium superconductivity and quasiparticle dynamics in $YBa_2Cu_3O_{7-\delta}$," Phys. Rev. B, vol. 63, no. 14, p. 140502, Mar. 2001.

[36]   M. Hashimoto, I. M. Vishik, R.-H. He, T. P. Devereaux, and Z.-X. Shen, "Energy gaps in high-transition-temperature cuprate superconductors," *Nat Phys*, vol. 10, no. 7, pp. 483–495, Jul. 2014.

[37]   A. Dienst *et al.*, "Bi-directional ultrafast electric-field gating of interlayer charge transport in a cuprate superconductor," *Nat Photon*, vol. 5, no. 8, pp. 485–488, Aug. 2011.

[38]   B. Mansart *et al.*, "Coupling of a high-energy excitation to superconducting quasiparticles in a cuprate from coherent charge fluctuation spectroscopy," *PNAS*, vol. 110, no. 12, pp. 4539–4544, Mar. 2013.

[39]   F. Geniet and J. Leon, "Nonlinear supratransmission," *J. Phys.: Condens. Matter*, vol. 15, no. 17, p. 2933, 2003.

[40]   S. Savel'ev, A. L. Rakhmanov, V. A. Yampol'skii, and F. Nori, "Analogues of nonlinear optics using terahertz Josephson plasma waves in layered superconductors," *Nat Phys*, vol. 2, no. 8, pp. 521–525, Aug. 2006.

[41]   U. Fano, "Effects of Configuration Interaction on Intensities and Phase Shifts," *Phys. Rev.*, vol. 124, no. 6, pp. 1866–1878, Dec. 1961.

[42]   K.-J. Boller, A. Imamoğlu, and S. E. Harris, "Observation of electromagnetically induced transparency," *Phys. Rev. Lett.*, vol. 66, no. 20, pp. 2593–2596, May 1991.

[43]   A. A. Abdumalikov, O. Astafiev, A. M. Zagoskin, Y. A. Pashkin, Y. Nakamura, and J. S. Tsai, "Electromagnetically Induced Transparency on a Single Artificial Atom," *Phys. Rev. Lett.*, vol. 104, no. 19, p. 193601, May 2010.

[44]   A. Dienst *et al.*, "Optical excitation of Josephson plasma solitons in a cuprate superconductor," *Nat Mater*, vol. 12, no. 6, pp. 535–541, Jun. 2013.

[45]   W. Hu *et al.*, "Optically enhanced coherent transport in YBa2Cu3O6.5 by ultrafast redistribution of interlayer coupling," *Nat Mater*, vol. 13, no. 7, pp. 705–711, Jul. 2014.

[46]   S. S. Apostolov, Z. A. Maizelis, M. A. Sorokina, V. A. Yampol'skii, and F. Nori, "Self-induced tunable transparency in layered superconductors," *Phys. Rev. B*, vol. 82, no. 14, p. 144521, Oct. 2010.

[47]   H. Frohlich, "On the Theory of Superconductivity: The One-Dimensional Case," *Proceedings of the Royal Society of London A: Mathematical, Physical and Engineering Sciences*, vol. 223, no. 1154, pp. 296–305, May 1954.

[48]   J. H. D. Boer and E. J. W. Verwey, "Semi-conductors with partially and with completely filled 3d-lattice bands. Proceedings of the Physical Society 49, 59 ." 1937.

[49]   N. F. Mott and R. Peierls, "Discussion of the paper by de Boer and Verwey.," *Proceedings of the Physical Society*, no. 49, p. 72, 1937.

[50]   J. Hubbard, "The magnetism of iron," *Physical Review B*, vol. 19, p. 2626, 1979.

[51]   J. Zaanen, G. A. Sawatzky, and J. W. Allen, "Band gaps and electronic structure of transition-metal compounds," *Phys. Rev. Lett.*, vol. 55, no. 4, pp. 418–421, Jul. 1985.

[52]   C. Giannetti, "New perspectives in the ultrafast spectroscopy of many-body excitations in correlated materials," *Il Nuovo Cimento C*, vol. 39, p. 279, 2016.

[53]   M. R. Presland, J. L. Tallon, R. G. Buckley, R. S. Liu, and N. E. Flower, "General trends in oxygen stoichiometry effects on Tc in Bi and Tl superconductors," *Physica C: Superconductivity*, vol. 176, no. 1, pp. 95–105, May 1991.

[54]   B. Bucher, P. Steiner, J. Karpinski, E. Kaldis, and P. Wachter, "Influence of the spin gap on the normal state transport in YBa2Cu4O8," *Phys. Rev. Lett.*, vol. 70, no. 13, pp. 2012–2015, Mar. 1993.

[55]   C. C. Homes, T. Timusk, R. Liang, D. A. Bonn, and W. N. Hardy, "Optical conductivity of c-axis oriented $YBa_2Cu_3O_{6.70}$: Evidence for a pseudogap," *Phys. Rev. Lett.*, vol. 71, no. 10, pp. 1645–1648, Sep. 1993.

[56]   D. N. Basov, T. Timusk, B. Dabrowski, and J. D. Jorgensen, "c-axis response of $YBa_2Cu_4O_8$: A pseudogap and possibility of Josephson coupling of CuO_2 planes," *Phys. Rev. B*, vol. 50, no. 5, pp. 3511–3514, Aug. 1994.

[57]   H. Ding *et al.*, "Spectroscopic evidence for a pseudogap in the normal state of underdoped high-Tc superconductors," *Nature*, vol. 382, no. 6586, pp. 51–54, Jul. 1996.

[58]   A. G. Loeser *et al.*, "Excitation Gap in the Normal State of Underdoped $Bi_2Sr_2CaCu_2O_{8+\delta}$," *Science*, vol. 273, no. 5273, pp. 325–329, Jul. 1996.

[59]   J. Wen *et al.*, "Magnetic field induced enhancement of spin-order peak intensity in $La_{1.875}Ba_{0.125}CuO_4$," *Phys. Rev. B*, vol. 78, no. 21, p. 212506, Dec. 2008.

[60] P. Dai, H. A. Mook, R. D. Hunt, and F. Doğan, "Evolution of the resonance and incommensurate spin fluctuations in superconducting $YBa_2Cu_3O_{6+x}$," *Phys. Rev. B*, vol. 63, no. 5, p. 54525, Jan. 2001.

[61] T. Suzuki and T. Fujita, "Structural phase transition in $(La_{1-x}Ba_x)_2CuO_{4-\delta}$," *Physica C: Superconductivity*, vol. 159, no. 1, pp. 111–116, Jun. 1989.

[62] M. K. Crawford *et al.*, "Lattice instabilities and the effect of copper-oxygen-sheet distortions on superconductivity in doped La_2CuO_4," *Phys. Rev. B*, vol. 44, no. 14, pp. 7749–7752, Oct. 1991.

[63] E. Fradkin and S. A. Kivelson, "High-temperature superconductivity: Ineluctable complexity," *Nat Phys*, vol. 8, no. 12, pp. 864–866, Dec. 2012.

[64] "Cooper, S. L., K. E. Gray, and D. M. Ginsberg. 'Physical Properties of High Temperature Superconductors IV.' World Scientific (1994)."

[65] P. W. Anderson, "Experimental Constraints on the Theory of High-Tc Superconductivity," *Science*, vol. 256, no. 5063, pp. 1526–1531, Jun. 1992.

[66] R. E. Peierls, *Quantum Theory of Solids*. Oxford University Press, 1955.

[67] W. Kohn, "Image of the Fermi Surface in the Vibration Spectrum of a Metal," *Phys. Rev. Lett.*, vol. 2, no. 9, pp. 393–394, May 1959.

[68] M. D. Johannes and I. I. Mazin, "Fermi surface nesting and the origin of charge density waves in metals," *Phys. Rev. B*, vol. 77, no. 16, p. 165135, Apr. 2008.

[69] A. M. Gabovich and A. I. Voitenko, "Superconductors with charge- and spin-density waves: theory and experiment (Review)," *Low Temperature Physics*, vol. 26, no. 5, pp. 305–330, May 2000.

[70] A. M. Gabovich, A. I. Voitenko, J. F. Annett, and M. Ausloos, "Charge- and spin-density-wave superconductors," *Supercond. Sci. Technol.*, vol. 14, no. 4, p. R1, 2001.

[71] A. Himeda, T. Kato, and M. Ogata, "Stripe States with Spatially Oscillating d-Wave Superconductivity in the Two-Dimensional t-t'-J Model," *Phys. Rev. Lett.*, vol. 88, no. 11, p. 117001, Feb. 2002.

[72] D. E. Moncton, J. D. Axe, and F. J. DiSalvo, "Study of Superlattice Formation in $2H-NbSe_2$ and $2H-TaSe_2$ by Neutron Scattering," *Phys. Rev. Lett.*, vol. 34, no. 12, pp. 734–737, Mar. 1975.

[73]   R. v. Coleman, B. Giambattista, P. k. Hansma, A. Johnson, W. w. McNairy, and C. g. Slough, "Scanning tunnelling microscopy of charge-density waves in transition metal chalcogenides," *Advances in Physics*, vol. 37, no. 6, pp. 559–644, Dec. 1988.

[74]   J. E. Hoffman *et al.*, "A Four Unit Cell Periodic Pattern of Quasi-Particle States Surrounding Vortex Cores in $Bi_2Sr_2CaCu_2O_{8+\delta}$," *Science*, vol. 295, no. 5554, pp. 466–469, Jan. 2002.

[75]   W. D. Wise *et al.*, "Charge-density-wave origin of cuprate checkerboard visualized by scanning tunnelling microscopy," *Nat Phys*, vol. 4, no. 9, pp. 696–699, Sep. 2008.

[76]   J. Chang *et al.*, "Direct observation of competition between superconductivity and charge density wave order in $YBa_2Cu_3O_{6.67}$," *Nat Phys*, vol. 8, no. 12, pp. 871–876, Dec. 2012.

[77]   A. Girlando, M. Masino, J. A. Schlueter, N. Drichko, S. Kaiser, and M. Dressel, "Charge-order fluctuations and superconductivity in two-dimensional organic metals," *Phys. Rev. B*, vol. 89, no. 17, p. 174503, May 2014.

[78]   J. M. Tranquada, B. J. Sternlieb, J. D. Axe, Y. Nakamura, and S. Uchida, "Evidence for stripe correlations of spins and holes in copper oxide superconductors," *Nature*, vol. 375, no. 6532, pp. 561–563, Jun. 1995.

[79]   P. Abbamonte, A. Rusydi, S. Smadici, G. D. Gu, G. A. Sawatzky, and D. L. Feng, "Spatially modulated 'Mottness' in $La_{2-x}Ba_xCuO_4$," *Nat Phys*, vol. 1, no. 3, pp. 155–158, Dec. 2005.

[80]   M. Fujita, H. Goka, K. Yamada, J. M. Tranquada, and L. P. Regnault, "Stripe order, depinning, and fluctuations in $La_{1.875}Ba_{0.125}CuO_4$ and $La_{1.875}Ba_{0.075}Sr_{0.050}CuO_4$," *Phys. Rev. B*, vol. 70, no. 10, p. 104517, Sep. 2004.

[81]   M. Fujita, H. Goka, K. Yamada, and M. Matsuda, "Competition between Charge- and Spin-Density-Wave Order and Superconductivity in $La_{1.875}Ba_{0.125-x}Sr_xCuO_4$," *Phys. Rev. Lett.*, vol. 88, no. 16, p. 167008, Apr. 2002.

[82]   D. H. Torchinsky, F. Mahmood, A. T. Bollinger, I. Božović, and N. Gedik, "Fluctuating charge-density waves in a cuprate superconductor," *Nat Mater*, vol. 12, no. 5, pp. 387–391, May 2013.

[83]   J. Demsar, L. Forró, H. Berger, and D. Mihailovic, "Femtosecond snapshots of gap-forming charge-density-wave correlations in quasi-two-dimensional

dichalcogenides 1T-TaS$_2$ and 2H-TaSe$_2$," *Phys. Rev. B*, vol. 66, no. 4, p. 41101, Jun. 2002.

[84]   H. Schäfer, V. V. Kabanov, M. Beyer, K. Biljakovic, and J. Demsar, "Disentanglement of the Electronic and Lattice Parts of the Order Parameter in a 1D Charge Density Wave System Probed by Femtosecond Spectroscopy," *Phys. Rev. Lett.*, vol. 105, no. 6, p. 66402, Aug. 2010.

[85]   D. Fausti *et al.*, "Light-Induced Superconductivity in a Stripe-Ordered Cuprate," *Science*, vol. 331, no. 6014, pp. 189–191, Jan. 2011.

[86]   M. Först *et al.*, "Melting of Charge Stripes in Vibrationally Driven La$_{1.875}$Ba$_{0.125}$CuO$_4$: Assessing the Respective Roles of Electronic and Lattice Order in Frustrated Superconductors," *Phys. Rev. Lett.*, vol. 112, no. 15, p. 157002, Apr. 2014.

[87]   C. R. Hunt, D. Nicoletti, S. Kaiser, T. Takayama, H. Takagi, and A. Cavalleri, "Two distinct kinetic regimes for the relaxation of light-induced superconductivity in La$_{1.675}$Eu$_{0.2}$Sr$_{0.125}$CuO$_4$," *Phys. Rev. B*, vol. 91, no. 2, p. 20505, Jan. 2015.

[88]   J. Demsar, B. Podobnik, V. V. Kabanov, T. Wolf, and D. Mihailovic, "Superconducting Gap Δc, the Pseudogap Δp, and Pair Fluctuations above Tc in Overdoped Y$_{1-x}$Ca$_x$Ba$_2$Cu$_3$O$_7$ from Femtosecond Time-Domain Spectroscopy," *Phys. Rev. Lett.*, vol. 82, no. 24, pp. 4918–4921, Jun. 1999.

[89]   R. A. Kaindl *et al.*, "Ultrafast Mid-Infrared Response of YBa$_2$Cu$_3$O$_{7-\delta}$," *Science*, vol. 287, no. 5452, pp. 470–473, Jan. 2000.

[90]   M. Hücker *et al.*, "Stripe order in superconducting LaBaCuO$_4$," *Phys. Rev. B*, vol. 83, no. 10, p. 104506, Mar. 2011.

[91]   C. C. Homes *et al.*, "Determination of the optical properties of LaBaCuO$_4$ for several dopings, including the anomalous x=1/8 phase," *Phys. Rev. B*, vol. 85, no. 13, p. 134510, Apr. 2012.

[92]   E. Berg et al., "Dynamical Layer Decoupling in a Stripe-Ordered High-Tc Superconductor," Phys. Rev. Lett., vol. 99, no. 12, p. 127003, Sep. 2007.

[93]   D. N. Basov and T. Timusk, "Electrodynamics of high-Tc superconductors," *Rev. Mod. Phys.*, vol. 77, no. 2, pp. 721–779, Aug. 2005.

[94]   L. S. Bilbro, R. V. Aguilar, G. Logvenov, O. Pelleg, I. Boović, and N. P. Armitage, "Temporal correlations of superconductivity above the transition

temperature in La$_{2-x}$Sr$_x$CuO$_4$ probed by terahertz spectroscopy," *Nat Phys*, vol. 7, no. 4, pp. 298–302, Apr. 2011.

[95]   J. Fink *et al.*, "Charge ordering in La$_{1.8-x}$Eu$_{0.2}$Sr$_x$CuO$_4$ studied by resonant soft x-ray diffraction," *Phys. Rev. B*, vol. 79, no. 10, p. 100502, Mar. 2009.

[96]   V. Khanna *et al.*, "Restoring interlayer Josephson coupling in LaBa$_{0.115}$CuO$_4$ by charge transfer melting of stripe order," *Phys. Rev. B*, vol. 93, no. 22, p. 224522, Jun. 2016.

[97]   Z. A. Xu, N. P. Ong, Y. Wang, T. Kakeshita, and S. Uchida, "Vortex-like excitations and the onset of superconducting phase fluctuation in underdoped La2-xSrxCuO4," *Nature*, vol. 406, no. 6795, pp. 486–488, Aug. 2000.

[98]   A. Schilling *et al.*, "Calorimetric measurement of the latent heat of vortex-lattice melting in untwinned YBa$_2$Cu$_3$O$_{7-\delta}$," *Nature*, vol. 382, no. 6594, pp. 791–793, Aug. 1996.

[99]   S. V. Dordevic, S. Komiya, Y. Ando, Y. J. Wang, and D. N. Basov, "Josephson vortex state across the phase diagram of La$_{2-x}$Sr$_x$CuO$_4$: A magneto-optics study," *Phys. Rev. B*, vol. 71, no. 5, p. 54503, Feb. 2005.

[100]   V. K. Thorsmølle, R. D. Averitt, T. Shibauchi, M. F. Hundley, and A. J. Taylor, "Dynamic Coupling-Decoupling Crossover in the Current-Driven Vortex State in Tl$_2$Ba$_2$CaCu$_2$O$_8$ Probed by the Josephson Plasma Resonance," *Phys. Rev. Lett.*, vol. 97, no. 23, p. 237001, Dec. 2006.

[101]   R. Cubitt *et al.*, "Direct observation of magnetic flux lattice melting and decomposition in the high-Tc superconductor Bi$_{2.15}$Sr$_{1.95}$CaCu$_2$O$_{8+x}$," *Nature*, vol. 365, no. 6445, pp. 407–411, Sep. 1993.

[102]   T. A. Fulton, R. C. Dynes, and P. W. Anderson, "The flux shuttle - A Josephson junction shift register employing single flux quanta," *Proceedings of the IEEE*, vol. 61, no. 1, pp. 28–35, Jan. 1973.

[103]   K. Nakajima, Y. Onodera, and Y. Ogawa, "Logic design of Josephson network," *Journal of Applied Physics*, vol. 47, no. 4, pp. 1620–1627, Apr. 1976.

[104]   A. M. Zagoskin, E. Il'ichev, M. W. McCutcheon, J. F. Young, and F. Nori, "Controlled Generation of Squeezed States of Microwave Radiation in a Superconducting Resonant Circuit," *Phys. Rev. Lett.*, vol. 101, no. 25, p. 253602, Dec. 2008.

[105] S. J. Denny, S. R. Clark, Y. Laplace, A. Cavalleri, and D. Jaksch, "Proposed Parametric Cooling of Bilayer Cuprate Superconductors by Terahertz Excitation," *Phys. Rev. Lett.*, vol. 114, no. 13, p. 137001, Mar. 2015.

[106] Y. Laplace, S. Fernandez-Pena, S. Gariglio, J. M. Triscone, and A. Cavalleri, "Proposed cavity Josephson plasmonics with complex-oxide heterostructures," *Phys. Rev. B*, vol. 93, no. 7, p. 75152, Feb. 2016.

[107] Q. Wu and X.-C. Zhang, "7 terahertz broadband GaP electro-optic sensor," *Applied Physics Letters*, vol. 70, no. 14, pp. 1784–1786, Apr. 1997.

[108] S. L. Dexheimer, *THz spectroscopy: principles and applications*. 6000 Broken Sound Parkway NW, FL 33487-2742: CRC Press, 2008.

[109] D. Redfield and W. J. Burke, "Optical absorption edge of LiNbO3," *Journal of Applied Physics*, vol. 45, no. 10, pp. 4566–4571, Oct. 1974.

[110] J. Hebling, G. Almási, I. Z. Kozma, and J. Kuhl, "Velocity matching by pulse front tilting for large-area THz-pulse generation," *Opt. Express, OE*, vol. 10, no. 21, pp. 1161–1166, Oct. 2002.

[111] Z. Bor, B. Racz, G. Szabo, M. Hilbert, and H. A. Hazim, "Femtosecond pulse front tilt caused by angular dispersion," *Opt. Eng*, vol. 32, no. 10, pp. 2501–2504, 1993.